

Evolution of microstructure and deformation mechanisms in a metastable Fe₄₂Mn₂₈Co₁₀Cr₁₅Si₅ high entropy alloy: A combined in-situ synchrotron X-ray diffraction and EBSD analysis

Jiajia Shen ^{a,g,*}, Wei Zhang ^b, J.G. Lopes ^a, Yutao Pei ^b, Zhi Zeng ^c, E. Maawad ^d, N. Schell ^d, Ana C. Baptista ^g, Rajiv S. Mishra ^{e,f}, J.P. Oliveira ^{a,g,*}

^a UNIDEMI, Department of Mechanical and Industrial Engineering, NOVA School of Science and Technology, Universidade NOVA de Lisboa, Caparica 2829-516, Portugal

^b Advanced Production Engineering, Engineering and Technology Institute Groningen, Faculty of Science and Engineering, University of Groningen, Nijenborgh 4, 9747 AG, the Netherlands

^c School of Mechanical and Electrical Engineering, University of Electronic Science and Technology of China, Sichuan 611731, China

^d Institute of Materials Physics, Helmholtz-Zentrum Hereon, Max-Planck-Str. 1, Geesthacht D-21502, Germany

^e Center for Friction Stir Processing, Department of Materials Science and Engineering, University of North Texas, Denton, TX 76207, USA

^f Advanced Materials and Manufacturing Processes Institute, University of North Texas, Denton, TX 76207, USA

^g CENIMAT/I3N, Department of Materials Science, NOVA School of Science and Technology, Universidade NOVA de Lisboa, 2829-516 Caparica, Portugal



ARTICLE INFO

Keywords:

High entropy alloys
Deformation mechanisms
Transformation twinning
Transformation induced plasticity
Synchrotron X-ray diffraction

ABSTRACT

In this work, a combination of in-situ high synchrotron X-ray diffraction and electron backscattered diffraction were used to systematically investigate the activation and evolution of the deformation mechanisms in an as-cast Fe₄₂Mn₂₈Co₁₀Cr₁₅Si₅ metastable high entropy alloy deformed until fracture at room temperature. This work unveils the critical role of the dual-phase γ -f.c.c. / ϵ -h.c.p. microstructure on the deformation response of the alloy. The different deformation modes, i.e., slip, transformation induced plasticity (TRIP) and transformation induced twinning (TWIP), were seen to initiate at different loading stresses and then to overlap. Quantitative microstructural characterization, which included the evolution of the phase fraction, stress partitioning, dislocation density, c/a ratio and lattice strain for different planes, was performed to elucidate the role of each phase on the macroscopic mechanical response of the metastable high entropy alloy. Furthermore, the magnitude of the different strengthening contributions has been quantified for the first time.

1. Introduction

High entropy alloys (HEAs) were first discovered independently by Yeh et al. and Cantor et al. in 2004 [1,2]. At the beginning, focus was devoted to the development of single phase HEAs. However, it is difficult to design single phase HEAs that simultaneously possess a good combination of strength and plasticity [3]. In order to overcome the strength-ductility paradigm, phase transformation induced plasticity (TRIP) [4], twinning induced plasticity (TWIP) [5,6], or the combined activation of TWIP and TRIP [7] have become new concepts in the design of non-equiaxed HEAs in the recent years. Such HEAs containing TRIP and/or TWIP effects are generally referred to as metastable HEAs [8]. In addition, such metastable HEAs often introduce auxiliary

strengthening mechanisms such as precipitation strengthening [9] and solid solution strengthening [10] which further increase the material strength.

The deformation mechanisms of metastable HEAs can be adjusted by the alloy stacking fault energy (SFE) which is composition- and temperature-dependent [11]. When the stacking fault energy is above 45 mJ/m², the dominant deformation mode is dislocation slip. With a decrease in the stacking fault energy, the dislocation slip-dominated deformation mechanism gradually changes to TWIP ($20 \text{ mJ/m}^2 > \text{SFE} > 40 \text{ mJ/m}^2$) or TRIP ($\text{SFE} < 15 \text{ mJ/m}^2$) [12]. The stacking fault energy values for the combined effect of TRIP and TWIP have also been reported to range between 13 mJ/m² and 18 mJ/m² [13]. Moreover, the stacking fault energy is key to changing the stability of the γ -f.c.c. matrix phase

* Corresponding author at: CENIMAT/I3N, Department of Materials Science, NOVA School of Science and Technology, Universidade NOVA de Lisboa, 2829-516 Caparica, Portugal.

E-mail addresses: j.shen@campus.fct.unl.pt (J. Shen), jp.oliveira@fct.unl.pt (J.P. Oliveira).

[14].

Li et al. [6] focusing on the Fe-Mn-Co-Cr system showed that the deformation mechanisms such as dislocation slip, TWIP and TRIP were adjustable by varying the Mn content, and that the strain-induced phase transition from γ -f.c.c. to ϵ -h.c.p. could simultaneously improve the strength and plasticity of the alloy. From their work, resulted a $\text{Fe}_{50}\text{Mn}_{30}\text{Co}_{10}\text{Cr}_{10}$ metastable HEA with a good strength/ductility balance. Earlier work reported that the addition of Si promotes the reduction of the stacking fault energy in this HEA system, which is effective in improving the metastability of the γ -f.c.c. matrix phase [15]. Thus, based on metastable engineering, Nene et al. [14] used thermodynamic simulations to assess the effect of Si addition on the metastability of the matrix γ -f.c.c. phase, showing that the addition of 5 at. % Si leads to a maximum metastability of γ -f.c.c. phase, which corresponded to a final nominal composition of $\text{Fe}_{42}\text{Mn}_{28}\text{Co}_{10}\text{Cr}_{15}\text{Si}_5$.

So far, most studies on the mechanical behavior of metastable HEAs have primarily focused on advanced electron microscopy characterization [16,17], while only a few studies using diffraction-based techniques to trace, in real time, the microstructure evolution and deformation mechanisms activation during deformation [18,19]. Specially for the optimized composition of $\text{Fe}_{42}\text{Mn}_{28}\text{Co}_{10}\text{Cr}_{15}\text{Si}_5$ developed in [14] there is still a gap on the microstructural evolution and assessment of the competing deformation mechanisms experienced by the alloy upon loading. Besides, the stress partitioning behavior, strengthening effects, lattice strain evolution, and the variation of the stacking fault probability with deformation are yet to be quantified.

In this study, the activation and changes in the deformation mechanisms of an as-cast $\text{Fe}_{42}\text{Mn}_{28}\text{Co}_{10}\text{Cr}_{15}\text{Si}_5$ metastable HEA during tensile deformation was evaluated in real time using high energy synchrotron X-ray diffraction. Stemming from the acquired diffraction data, the micromechanical behavior of the two main constituent phases of the alloy was determined. The TRIP and TWIP effects of the current studied material during tensile deformation and the onset for each to occur are revealed and discussed. By quantifying the evolution of dislocation density and stacking faults, the strengthening contributions for the material strength have been elucidated for the first time. A detailed and comprehensive analysis of the diffraction data determined the relationship between the microstructure evolution and the alloy mechanical behavior, providing a deeper understanding of the different deformation mechanisms activated metastable HEAs.

2. Experimental procedure and methods

2.1. Starting material

The material used in this work was an as-cast non-equiautomic metastable $\text{Fe}_{42}\text{Mn}_{28}\text{Co}_{10}\text{Cr}_{15}\text{Si}_5$ (at. %) HEA, obtained by vacuum induced melting under an argon atmosphere [20].

A Leica DMI 5000 M inverted optical microscope was used to detail the microstructure evolution before and after tensile deformation. Standard metallography was used to prepare the samples, which were etched with Kalling's-2 reagent (5 g CuCl_2 , 100 ml HCl and 100 ml $\text{C}_2\text{H}_5\text{OH}$) at room temperature for 40 s. Dog-bone shaped specimens for tensile testing with a cross section of $1.5 \times 2 \text{ mm}^2$ and gauge length of 16 mm were used. Tensile testing was performed at room temperature with a $1 \times 10^{-3} \text{ s}^{-1}$ strain rate.

2.2. In-situ synchrotron X-ray diffraction

High energy synchrotron X-ray diffraction was used to investigate the deformation behavior of the metastable $\text{Fe}_{42}\text{Mn}_{28}\text{Co}_{10}\text{Cr}_{15}\text{Si}_5$ HEA during the loading process. Experiments were performed at the P07/High Energy Materials Science beamline of Petra III at the DESY synchrotron, Germany. A monochromatic X-ray beam with a fixed energy of 87 keV was used. A Perkin Elmer 2D detector with a pixel size of $200 \times 200 \mu\text{m}^2$ collected the scattered intensity in the form of Debye-Scherrer

rings at 12 different loading stresses. The beam size was set to $700 \times 700 \mu\text{m}^2$. The sample-to-detector distance was of 1.226 m, which was determined by calibration with LaB_6 powder.

The raw 2D Debye-Scherrer diffraction images can be converted to one dimensional diffraction patterns by full or partial integration using open-source software Fit2D [21]. Here, full integration along the azimuthal angle was performed to get an overall understanding of the microstructural changes induced in the material upon tensile loading. To evaluate the orientation-dependent microstructural evolution of certain lattice planes of both phases, partial integration along the loading direction, LD, and transverse direction, TD, was performed. The integration ranges were set from 85 to 95° for LD and from -5 to 5° for TD.

A single-peak fitting routine was performed on the 1D X-ray diffraction patterns using the structural analysis software GSAS II [22], to determine the diffraction peak positions of different lattice planes, their integrated intensity and full width at half maximum (FWHM). These microstructure features were then used to calculate the dislocation density, dislocation strengthening, stacking fault strengthening, and the evolution of the lattice strain during the tensile process, as it will be described in detail in the next sections. Rietveld refinement using the Materials Analysis Using Diffraction (MAUD) software [23] was used for full spectrum fitting to determine the evolution of lattice parameters, phase volume fraction, and to support the phase identification of the acquired diffraction spectra.

2.2.1. Phase volume fraction

The physics-based diffraction models used in MAUD software enable to successfully capture the effects of variations in crystallographic properties, phase fraction as well as material/phase texture, enabling quantitative analysis of the microstructural evolution of the material upon mechanical loading. For the Rietveld refinement procedure used in this work, a polynomial function of degree four was used to reproduce the pattern background [24], while the Cagliotti PV model was chosen for the instrumental broadening and the Popa model was selected for anisotropic broadening [25,26]. The extended Williams-Imhof-Mathies-Vinel algorithm (E-WIMV) [27] was used as the texture model for considering the texture evolution under tensile loading, as described by Wenk et al. [28]. A triaxial elastic stress model with $\sigma_{11} \neq 0$ and $\sigma_{22} = \sigma_{33} \approx 0$ [29,30] was used and the c_{11} , c_{12} and c_{44} single crystal elastic constants for both γ -f.c.c. phase and ϵ -h.c.p. phase were obtained from [31], while the mechanical parameters based on the Young's modulus, E , [32] and Poisson's ratio, ν , can be derived by the Hill-averaged Voigt and Reuss bounds [33] as described by the following equations,

$$E = \frac{9BG}{3B + G} \quad (1)$$

$$\nu = \frac{3B - 2G}{2(3B + G)} \quad (2)$$

where,

$$G = \frac{\left\{ \frac{5(c_{11}-c_{12})c_{44}}{4c_{44}+3(c_{11}-c_{12})} + \frac{c_{11}-c_{12}+3c_{44}}{5} \right\}}{2} \quad (3)$$

$$B = \frac{c_{11} + 2c_{12}}{3} \quad (4)$$

here E is the Young's modulus, ν is the Poisson's ratio, c_{11} , c_{12} and c_{44} are the single crystal elastic constants.

2.2.2. Phase stress partitioning calculation

An in-depth understanding of the deformation behavior of the constituent phases in the metastable $\text{Fe}_{42}\text{Mn}_{28}\text{Co}_{10}\text{Cr}_{15}\text{Si}_5$ HEA during macroscopic tensile deformation and a quantitative analysis of the stress/strain relationship between the soft γ -f.c.c. phase and the hard

ϵ -h.c.p. phase is essential for gaining an insight into the deformation mechanisms of the material and for the design of new materials. Therefore, in order to investigate the micromechanical behavior of the currently studied alloy, the von Mises criterion was introduced to evaluate the stress distribution in both γ -f.c.c. and ϵ -h.c.p. phases.

The phase stress partitioning was calculated considering the (311) lattice plane of the γ -f.c.c. phase [34,35] and of the (10 $\bar{1}$ 2) lattice plane of the ϵ -h.c.p. phase [36], since these planes have a relatively low intergranular strain sensitivity. Thus, with these two specific lattice planes, it is possible to obtain a representative stress/strain behavior of the individual phases that compose the metastable HEA used in this work.

The von Mises stress, σ_{vm} , used to calculate the phase stresses is detailed as follows,

$$\sigma_{vm} = \frac{1}{\sqrt{2}} [(\sigma_{11} - \sigma_{22})^2 + (\sigma_{22} - \sigma_{33})^2 + (\sigma_{33} - \sigma_{11})^2]^{\frac{1}{2}} \quad (5)$$

Here, σ_{11} refers to the principal stress parallel to the direction of loading (LD) and σ_{22} and σ_{33} correspond to the principal stresses perpendicular to the direction of loading (TD). $\sigma_{22} = \sigma_{33} \approx 0$ is assumed here for the flat-plate specimen in this study [37]. The value of σ_{11} can be obtained from lattice strain calculations [38] by the following equations,

$$\sigma_{11} = \frac{E}{1+v} \epsilon_{11} + \frac{vE}{(1+v)(1-2v)} (\epsilon_{11} + \epsilon_{22} + \epsilon_{33}) \quad (6)$$

$$v = -\frac{\epsilon_{transverse}}{\epsilon_{longitudinal}} \quad (7)$$

Here, ϵ_{11} is the lattice strain along the LD, ϵ_{22} and ϵ_{33} are the lattice strains perpendicular to the LD (assuming $\epsilon_{22} = \epsilon_{33}$ [36]). The azimuthal integration ranges corresponding to the LD and TD were from 85 to 95° and from -5 to 5°, respectively, as previously described. The specific calculation procedure for determination of the lattice strain has been described in subsection 2.2.6. E denotes the Young's modulus of the selected lattice planes, i.e., (311) for γ -f.c.c. and (10 $\bar{1}$ 2) for ϵ -h.c.p. calculated along LD, which can be determined by linearly fitting the evolution of the lattice strain in the elastic range. The ratio of the transverse lattice strain, ϵ_{22} , to the longitudinal lattice strain, ϵ_{11} , is the Poisson's ratio, v , as shown in Eq. (7).

Subsequently, the rule-of mixture [39] for the mechanical properties of multiphase materials was used to further investigate the contribution from each constituent phase to the total tensile stress. The fraction-weighted average stress can be calculated by summing up the contribution stresses of both γ -f.c.c. and ϵ -h.c.p. phases [40],

$$\sigma = V_{\gamma\text{-f.c.c.}} \sigma_{\gamma\text{-f.c.c.}} + V_{\epsilon\text{-h.c.p.}} \sigma_{\epsilon\text{-h.c.p.}} \quad (8)$$

where $V_{\gamma\text{-f.c.c.}}$ and $V_{\epsilon\text{-h.c.p.}}$ correspond to the phase volume fraction of the γ -f.c.c. and ϵ -h.c.p. phases (subsection 2.2.1 previously detailed this calculation procedure). $\sigma_{\gamma\text{-f.c.c.}}$ and $\sigma_{\epsilon\text{-h.c.p.}}$ refer to the phase stresses of the γ -f.c.c. and ϵ -h.c.p. phases, which were obtained from the representative lattice planes, i.e., (311) for γ -f.c.c. and (10 $\bar{1}$ 2) for ϵ -h.c.p., respectively.

2.2.3. Dislocation density calculations

Increase in dislocation density is a main source of strengthening in most engineering alloys [41], and its quantitative measurement is essential for understanding its contribution to overall strengthening and even for making qualitative judgements on the main deformation mechanisms of a material. Conventional transmission electron microscopy (TEM) [42] and X-ray diffraction line profile analysis [43] are indirect methods for measuring the dislocation density. However, when the dislocation density is high enough ($>10^{14} \text{ m}^{-2}$), its determination by TEM is hard [44]. This difficulty can be overcome by using X-rays [43]. In addition, the Williamson-Hall model has been shown as a possible

method to correlate the broadening of different diffraction peaks with dislocation density, and thus derive the dislocation density [45].

Here, the dislocation density evolution of the metastable Fe₄₂Mn₂₈-Co₁₀Cr₁₅Si₅ HEA during tensile deformation was calculated by combining the analysis of the FWHM obtained by X-ray line profile analysis with the Williamson-Hall model. The diffraction peaks were obtained by integrating along the full azimuthal angle, as well as along LD and TD. A pseudo-Voigt function was used for the single-peak fitting, and the obtained full width at half maximum is named FWHM_{measured}, and it consists of three main contributions. One is the instrumental-induced peak broadening [46] (specified as FWHM_{instrumental}) and its value can be obtained from the LaB₆ standard powder. The other two components include the peak broadening due to the average microstrain, ϵ_0 , caused by dislocations, and grain size-induced peak broadening. The peak broadening arising by these two contributions is termed FWHM_{microstrain + grain size}. Thus, the broadening of a diffraction peak caused by dislocations and grain size can be obtained from the following equations [47],

$$\text{FWHM}_{\text{microstrain+grainsize}} = [(FWHM_{\text{measured}})^2 - (FWHM_{\text{instrumental}})^2]^{\frac{1}{2}} \quad (9)$$

$$\text{FWHM}_{\text{microstrain+grainsize}} = \text{FWHM}_{\text{microstrain}} + \text{FWHM}_{\text{grainsize}} \quad (10)$$

Here, FWHM_{grainsize} can be estimated from the Scherrer formula [48,49], as shown below,

$$\text{FWHM}_{\text{microstrain}} = 4\epsilon_0 \frac{\sin\theta}{\cos\theta} \quad (11)$$

and

$$\text{FWHM}_{\text{grainsize}} = \frac{k\lambda}{D \cos\theta} \quad (12)$$

Here, ϵ_0 is the average microstrain [50], θ is the half of the Bragg angle of a selected diffraction peak [51], D is the average grain size [45], k is a constant, assumed as 0.9 here [51,52], λ is the wavelength of the X-ray beam (0.14235 Å) [53]. Taking Eq. (11) and Eq. (12) into Eq. (10), Eq. (10) will be simplified as follows,

$$\text{FWHM}_{\text{microstrain+grainsize}} \times \cos\theta = 4\sin\theta \epsilon_0 + \frac{k\lambda}{D} \quad (13)$$

To derive the average microstrain, ϵ_0 , as well as the grain size, D, Eq. (13) can be considered as a linear equation of one variable as below,

$$y = kx + b \quad (14)$$

where y can be treated as FWHM_{microstrain + grain size} $\times \cos(\theta)$, while x corresponds to $4 \times \sin(\theta)$, K is the average microstrain ϵ_0 and b is $(k \times \lambda) / D$. In this approach, the values of the FWHM_{microstrain + grain size} $\times \cos(\theta)$ and $4 \times \sin(\theta)$ were obtained from different diffraction peaks [47]. It is worth noting the definition of the parameter ϵ_0 . Although it is usually referred to as "strain" or "lattice strain" in the literature [45], it does not simply mean the average strain scale (e.g., strain measured by an extensometer upon loading). Venkateswarlu et al. called it an inhomogeneous strain [50], but its definition remains vague, and some researchers avoid the definition of this parameter [47,54]. Here, we define it as the average microstrain experienced by each phase during macroscopic loading.

Based on the above calculated microstrain, ϵ_0 , and grain size, D, the dislocation density, ρ , can be estimated by the Williamson-Hall method [55]. The specific equation is as follows,

$$\rho = \frac{2\sqrt{3}\epsilon_0}{Db} \quad (15)$$

where b refers to the Burgers vector, and its magnitude depends on the dislocation slip system [56]. For the γ -f.c.c. phase structure, the

magnitude of Burger's vector changes from $\frac{\sqrt{2}}{2}a_{f.c.c.}$ into $\frac{1}{\sqrt{6}}a_{f.c.c.}$ [57–59], due to the evolution of the {111} perfect dislocation slip system into a [11 2]{111} Schockley partial dislocation slip system [60]. $a_{f.c.c.}$ is the lattice parameter of the ϵ -f.c.c. phase. Similarly, for the ϵ -h.c.p. phase structure, the slip system transforms from a basal slip to a pyramidal slip as plastic deformation progresses [20]. Correspondingly, the magnitude of the Burgers vector for ϵ -h.c.p. changes from $\frac{\sqrt{6}}{3}$ to $\frac{\sqrt{16}}{3}$, depending on the slip system, with the former corresponding to the basal $< a >$ slip plane, and the latter to the prismatic $< c >$ and pyramidal $< c + a >$ slip planes [61,62].

2.2.4. Strengthening contributions calculations

To investigate the strengthening contributions arising from the different deformation mechanisms experienced by the Fe₄₂Mn₂₈Co₁₀Cr₁₅Si₅ alloy during tensile deformation, the Bailey-Hirsch model [63] was applied to describe the dislocation strengthening effect, $\Delta\sigma_D$, in the material,

$$\Delta\sigma_D = MaGb\rho^{\frac{1}{2}} \quad (16)$$

where M is the *Taylor factor*, α is a proportionality factor [61], G is the shear modulus, b is the burgers vector, and ρ is the *dislocation density* [64].

In this work, the following parameters were used: i) for the ϵ -h.c.p. phase, M is 3.06 [65], the value of α is 1.16 [66] in the $< c + a >$ slip system, which is larger than that in the basal-basal interaction [61] while in the $< a >$ slip system is assumed as 0.2 [61] and G is 78 GPa [67]; ii) for the γ -f.c.c. phase, M is 3.06 [51], α is 0.36 [34] and G is 76 GPa [68]. The selection of the Burgers vectors, b, for the different deformation stages of both γ -f.c.c. and ϵ -h.c.p. phases, as well as the dislocation densities obtained, have been described in previously in section 2.2.3.

In addition to the dislocation density strengthening mechanism, the strain induced transformation from γ -f.c.c. to ϵ -h.c.p. is another primary deformation mechanism [69]. However, the transition from γ -f.c.c. to ϵ -h.c.p. requires the presence of large number of stacking faults in the γ -f.c.c. phase [6]. Thus, stacking faults are the core of the ϵ -h.c.p. phase formation. The quantitative study of stacking fault strengthening, σ_{sf} , can be achieved by tracking the changes in the stacking faults interspacing, L_{sf} , which impedes dislocation movement during deformation, and the probability of stacking faults formation, P_{sf} .

Holden et al. [70] using neutron diffraction experiments, reported that the difference in the diffraction peaks in the (111) and (222) γ -f.c.c. lattice planes may not be caused by elastic strain but by structural factors in the stacking faults among the γ -f.c.c. phase. Jeong et al. [71] achieved a similar conclusion using synchrotron radiation. Since the (111) and (222) γ -f.c.c. lattice planes have equivalent crystallographic orientations, the occurrence of stacking faults can lead to differences in lattice strain in these reflections [72]. Thus, the shifts of the diffraction peaks of the γ -f.c.c. (111) and (222) lattice planes obtained by full azimuthal integration were chosen to evaluate the evolution of the stacking faults interspacing, L_{sf} , *stacking fault probability*, P_{sf} , and hence the *stacking fault strengthening*, σ_{sf} , contribution of the Fe₄₂Mn₂₈Co₁₀Cr₁₅Si₅ HEA.

The lattice strain, ε_{hkl} of the γ -f.c.c. (111) and (222) planes, obtained using the previously described peak fitting routine, consists of the elastic lattice strain, $\varepsilon_{(hkl)}^e$, and the lattice strain induced by stacking faults, $\varepsilon_{(hkl)}^{sf}$ [73,74]. Since the (111) and (222) γ -f.c.c. planes are equivalent in terms crystallographic orientation, the elastic lattice strains of γ -f.c.c. (111) and (222) planes are equal ($\varepsilon_{222}^e = \varepsilon_{111}^e$). The detailed derivation is detailed as follows,

$$\varepsilon_{(hkl)} = \varepsilon_{(hkl)}^e + \varepsilon_{(hkl)}^{sf} = \frac{d_{hkl} - d_{hkl}^0}{d_{hkl}^0} \quad (17)$$

$$\varepsilon_{222}^e = \varepsilon_{111}^e \text{ and} \quad (18)$$

$$\begin{aligned} \varepsilon_{222} - \varepsilon_{111} &= (\varepsilon_{222}^e + \varepsilon_{222}^{sf}) - (\varepsilon_{111}^e + \varepsilon_{111}^{sf}) = \varepsilon_{222}^{sf} - \varepsilon_{111}^{sf} \\ &= \frac{d_{222} - d_{222}^0}{d_{222}^0} - \frac{d_{111} - d_{111}^0}{d_{111}^0} \end{aligned} \quad (19)$$

where d_{hkl} is the hkl-specific lattice spacing obtained at different loading steps, and d_{hkl}^0 is the corresponding stress-free lattice spacing. The stacking faults and hkl-dependent lattice strain ε_{hkl} can be correlated with the experimentally measured lattice strain via the following equation [96],

$$\varepsilon_{hkl} = -\frac{\sqrt{3}}{4\pi} \frac{\sum_b (\pm L_0)}{h_0^2(u+b)} P_{sf} \quad (20)$$

In Eq. (20), u, b, h and L_0 in $\frac{\sum_b (\pm L_0)}{h_0^2(u+b)}$ are crystal structure-related parameters [75], with values of +1/4 and -1/8 being reported [19,73] for the (111) and (222) γ -f.c.c. orientations, respectively; u and b correspond to the non-broadened and broadened components due to the stacking faults, respectively [74,76]. This leads to the following simplified equations for the lattice strain ε_{111} , ε_{222} and stacking faults probability, P_{sf} [19,77],

$$\varepsilon_{222} = -\frac{\sqrt{3}}{4\pi} \left(-\frac{1}{8} \right) P_{sf} = 0.0173P_{sf} \quad (21)$$

$$\varepsilon_{111} = -\frac{\sqrt{3}}{4\pi} \left(\frac{1}{4} \right) P_{sf} = -0.0344P_{sf} \quad (22)$$

$$\varepsilon_{222} - \varepsilon_{111} = 0.0173P_{sf} - (-0.0344P_{sf}) = 0.0517P_{sf} \quad (23)$$

$$P_{sf} = \frac{\varepsilon_{222} - \varepsilon_{111}}{0.0517} = \frac{\frac{d_{222} - d_{222}^0}{d_{222}^0} - \frac{d_{111} - d_{111}^0}{d_{111}^0}}{0.0517} \quad (24)$$

Then, the interspacing between stacking faults, L_{sf} , can be obtained from d_{111} and P_{sf} [63,77], and is given by the following relation [77],

$$L_{sf} = \frac{d_{111}}{P_{sf}} \quad (25)$$

where d_{111} and P_{sf} refer to the (111) d-spacing (obtained from full azimuthal integration) and stacking faults probability, respectively.

Based on the results obtained from the above calculations, the stacking faults strengthening, σ_{sf} , can be obtained by the following equation [63,77],

$$\sigma_{sf} = \frac{K_{sf}}{L_{sf}} \quad (26)$$

where L_{sf} is the interspacing between stacking faults, which can be obtained from Eq. (25), K_{sf} is the strengthening coefficient, and the following formula can be used to calculate this parameter,

$$\sigma_{yield} = \sigma_a + K_{sf} \frac{1}{L_{sf}} \quad (27)$$

K_{sf} is the slope of the linear fit between $1/L_{sf}$ (corresponding to the x-axis) and the yield strength, σ_{yield} , (corresponding to the y-axis) [63], which can be interpreted as the extra energy consumed by dislocations to cut through stacking faults when dislocations are impinged at them. Additional details for determining K_{sf} exist in [63]. σ_a is the total strength contributed by various strengthening mechanisms other than stacking faults [78]. The K_{sf} value calculated in this paper is 2610 MPa.nm indicating that the stacking faults act as a strong barrier against dislocation slip.

2.2.5. c/a ratio calculations

The c/a ratio is a key structural parameter of the h.c.p. phase that can

be directly related to the lattice spacing [62], and is also closely related to the structural plane features that control the activation of the structural slip systems in this phase [79]. The ideal value of the c/a ratio is 1.633, although this value can be adjustable in magnitude [79]. The c/a ratio depends on the alloy composition and the addition of ϵ -h.c.p. phase stabilizers (such as Co, Mn, Si) can increase the c/a ratio, while γ -f.c.c. phase stabilizers (Cu, Al) can decrease it. Thermomechanical processing and deformation is another way of changing the c/a ratio due to the dependence of the lattice parameters on the microstructure and stress state. Small changes in the c/a ratio allows to infer that different slip systems can be activated and thus affect the ductility of the ϵ -h.c.p. phase [19].

The Rietveld refinement methodology previous described was used to determine the c/a ratio change during tensile loading. The formula used to calculate the c/a ratio is as follows,

$$\frac{c}{a_{ratio}} = \frac{c_{\epsilon-h.c.p. \text{ phase}}}{a_{\epsilon-h.c.p. \text{ phase}}} \quad (28)$$

where $c_{\epsilon-h.c.p. \text{ phase}}$ and $a_{\epsilon-h.c.p. \text{ phase}}$ refer to the lattice constants of the ϵ -h.c.p. phase.

2.2.6. Lattice strain calculation

The response of different lattice planes to the applied load during deformation of a material is important for understanding the alloy micromechanical behavior. In this study, the lattice strain evolution of the γ -f.c.c. and ϵ -h.c.p. phases in the Fe₄₂Mn₂₈Co₁₀Cr₁₅Si₅ HEA was calculated along the LD and TD. The (111), (200) and (311) lattice planes in the γ -f.c.c. phase, and the (10 $\bar{1}$ 0), (10 $\bar{1}$ 1), (10 $\bar{1}$ 2) and (10 $\bar{1}$ 3) planes of the ϵ -h.c.p. phase were chosen and single peak fitted. The lattice strain, ε_{hkl} , for a selected (hkl) plane was calculated as,

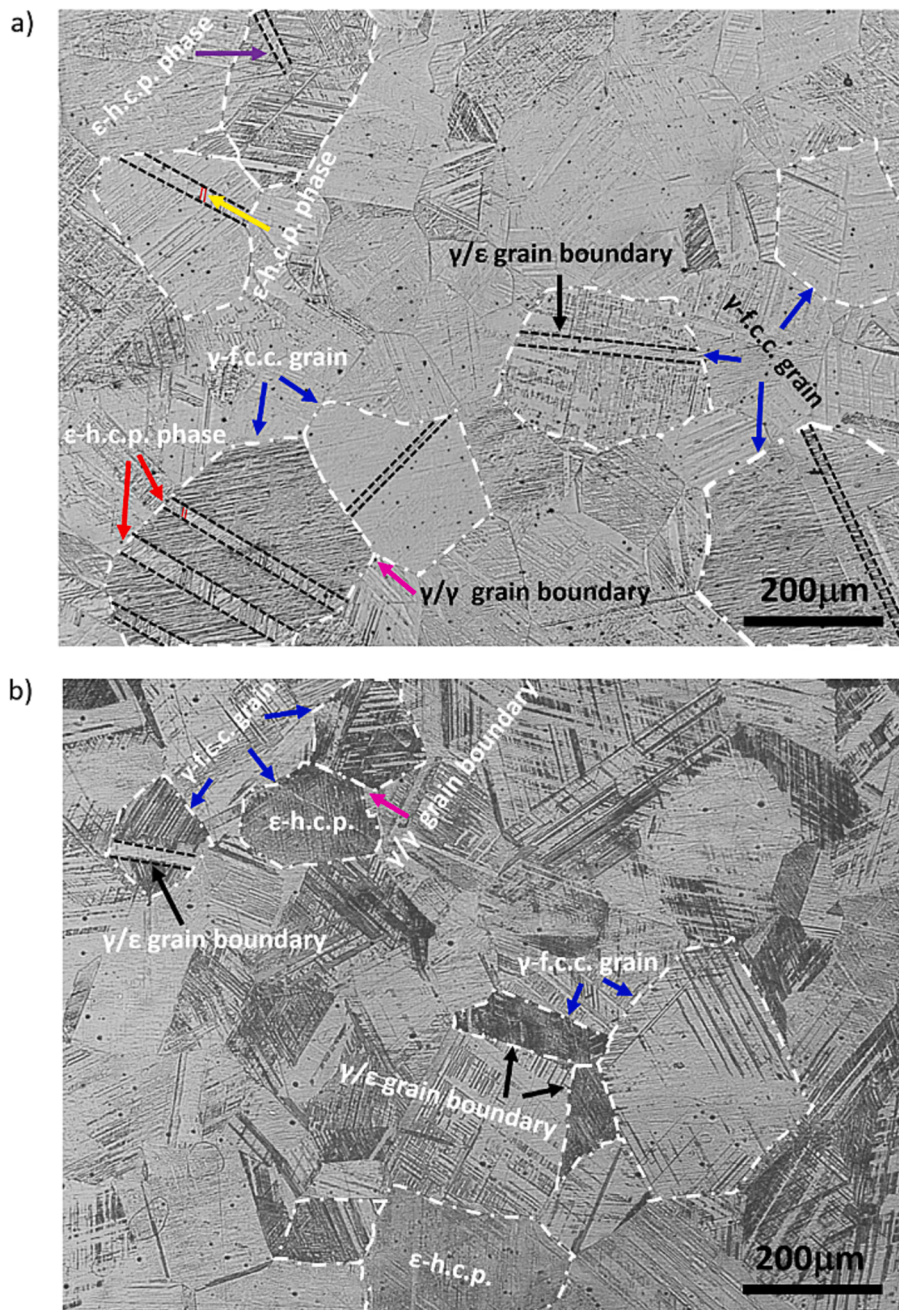


Fig. 1. Optical microscopy of the metastable Fe₄₂Mn₂₈Co₁₀Cr₁₅Si₅ HEA: a) before deformation and b) after fracture.

$$\varepsilon_{hkl} = \frac{d_{hkl} - d_{hkl}^0}{d_{hkl}^0} \times 10^{-6} \quad (29)$$

where d_{hkl} and d_{hkl}^0 represent the interplanar spacings for a certain (hkl) plane under loading and in the stress-free condition, respectively.

2.3. In-situ EBSD tensile tests

To complement and gain a deeper insight into the evolution of microstructural changes induced during tensile testing to failure of the present metastable HEA, an in-situ Electron Backscatter Diffraction (EBSD) analysis was also performed. The in-situ tensile testing was performed using a Kammerath & Weiss tensile module at room temperature with a strain rate of 3×10^{-4} s. The EBSD analysis was carried out in real-time during the deformation process in the standard gauge plane.

It should be mentioned that in-situ synchrotron X-ray analysis and EBSD will provide different, yet complementary microstructural information. For the former, bulk information is obtained since the high energy used allows to work in transmission mode, while for the latter surface information is obtained. This also enables to assess potential changes in the phase transformation evolution which can occur when comparing bulk vs surface conditions.

3. Results

Because of the complexity of deformation mechanisms exhibited by the metastable Fe₄₂Mn₂₈Co₁₀Cr₁₅Si₅ HEA, the results are first shown separately. The discussion section will leverage on these results to clearly detail the micromechanical behavior of the studied alloy.

3.1. Microstructure

Fig. 1 a) and b) depict the microstructure of the metastable Fe₄₂Mn₂₈Co₁₀Cr₁₅Si₅ HEA before and after tensile deformation, respectively. After etching, a dual γ -f.c.c. / ϵ -h.c.p. microstructure is evidenced in both conditions. The bright and dark contrasting colors are related to the microstructural features of both phases.

The γ -f.c.c. grain size decreases with increasing strain, from ≈ 184 to ≈ 150 μm ($\approx 18\%$ reduction), indicating that imposed strain rate does not significantly refine the grain in the Fe₄₂Mn₂₈Co₁₀Cr₁₅Si₅ HEA. This behavior is unlike that observed for a Fe₅₀Mn₃₀Co₁₀Cr₁₀ HEA [14], suggesting the improved grain stability during mechanical behavior upon the addition of Si. Qualitative, it is also observed that the fraction of ϵ -h.c.p. phase in the fractured sample increased. Here, the differentiation of the ϵ -h.c.p. phase from the microstructure is elucidated based

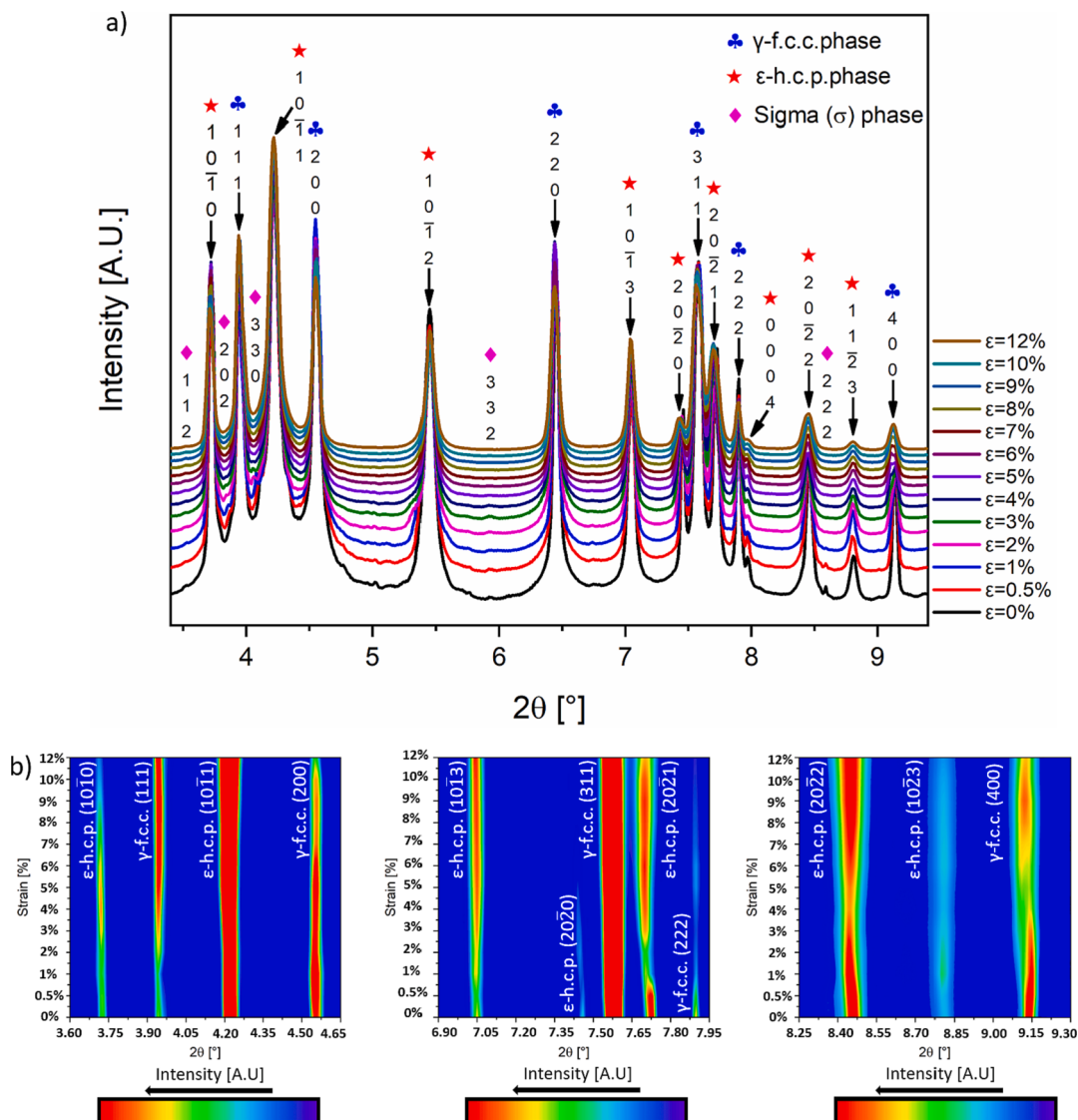


Fig. 2. a) superimposition of the 1D diffraction patterns, b) contour plots of specific diffraction ranges.

on information presented in the authors' previous works [80], along with findings reported by other researchers [20]. The original as-cast $\text{Fe}_{42}\text{Mn}_{28}\text{Co}_{10}\text{Cr}_{15}\text{Si}_5$ metastable High Entropy Alloy (HEA) comprises two distinct phases: a γ -f.c.c. structure and an ϵ -h.c.p. phase. The parent γ -f.c.c. phases appear to be delineated by laths of the ϵ -h.c.p. phase, which traverse individual grains and are densely filled with compact laths. The microstructural and morphological characteristics of the two phases are examined to distinguish the ϵ -h.c.p. and γ -f.c.c. phases, as illustrated in Fig. 1.

Fig. 2 a) and b) depict the superimposition of the X-ray diffraction patterns of the metastable $\text{Fe}_{42}\text{Mn}_{28}\text{Co}_{10}\text{Cr}_{15}\text{Si}_5$ HEA during tensile deformation and the corresponding contour plots, respectively. γ -f.c.c., ϵ -h.c.p. as well as a tetragonal structure known as σ phase are identified. This phase identification is in good agreement with existing literature [81]. Observation of the diffraction spectra in Fig. 2 a), details that no new phases are formed upon loading.

Fig. 2 b) reveals the intensity evolution of different lattice planes of the γ -f.c.c. and ϵ -h.c.p. phases during tensile loading. Although no new phases were detected in the metastable $\text{Fe}_{42}\text{Mn}_{28}\text{Co}_{10}\text{Cr}_{15}\text{Si}_5$ HEA during deformation (refer to Fig. 2 a), there are obvious changes in the diffracted intensity, indicating that transformation from γ -f.c.c. to ϵ -h.c.p. is occurring due to the TRIP effect [14]. Further observation of the evolution of the diffracted intensity of the γ -f.c.c. (400) and (222) peaks show a decrease in their intensity with increasing strain, while the intensity of the ϵ -h.c.p. (10 $\bar{1}$ 0) and (20 $\bar{2}$ 2) diffraction peaks increase significantly. This qualitative observation further suggests the increase in the volume fraction of the ϵ -h.c.p. phase during deformation at the expense of the γ -f.c.c. phase. However, it is worth mention here that the intensity of diffraction peaks is influenced not only by the volume fraction of a phase but also by factors such as crystallite size, texture, and the specific orientation of crystallites with respect to the incident X-ray beam. For example, the decrease in intensity can be attributed to variations in crystallite size or preferred orientation that temporarily suppress the diffraction peaks despite an overall increase in the ϵ -h.c.p. phase volume fraction. The quantitative analysis of the evolution of the phase fractions of both γ -f.c.c. and ϵ -h.c.p. phases has been presented in the following section.

The lattice parameters of the γ -f.c.c., ϵ -h.c.p. and σ phases before and after deformation, as obtained by Rietveld refinement, are shown in Table 1. The results of the lattice parameters of the γ -f.c.c. and ϵ -h.c.p. phases prior to loading are in good agreement the existing literature [20,81].

The c/a ratio before and after loading was also determined (see to Table 1). Initially, the as-cast $\text{Fe}_{42}\text{Mn}_{28}\text{Co}_{10}\text{Cr}_{15}\text{Si}_5$ HEA has a c/a ratio of approximately ≈ 1.625 , which is significantly lower than the ideal value of ≈ 1.633 [79], but very close to that of the as-cast $\text{Fe}_{40}\text{Mn}_{20}\text{Co}_{20}\text{Cr}_{15}\text{Si}_5$ HEA (≈ 1.625) [79] and as-rolled $\text{Fe}_{42}\text{Mn}_{28}\text{Co}_{10}\text{Cr}_{15}\text{Si}_5$ (≈ 1.622) [20]. As expected, the c/a ratio in the present alloy is slightly higher than that reported by Bu et al. (≈ 1.616) for a duplex $\text{Fe}_{50}\text{Mn}_{30}\text{Co}_{10}\text{Cr}_{10}$ HEA [62]. This is related to the addition of Si, a ϵ -h.c.p. phase stabilizer, which promotes the increase of the c/a ratio, while the concomitant decrease of Mn, a γ -f.c.c. phase stabilizer, can decrease it. However, Si has a stronger effect (roughly 22 times higher) that that

Table 1

Refined lattice parameters of the ϵ -h.c.p., γ -f.c.c. and σ phases in the as-cast metastable $\text{Fe}_{42}\text{Mn}_{28}\text{Co}_{10}\text{Cr}_{15}\text{Si}_5$ HEA as obtained by Rietveld refinement.

| Condition | ϵ -h.c.p. phase (Hexagonal: P63/mmc) | | | γ -f.c.c. phase (FCC: Fm/ 3m) | σ phase (Tetragonal P42/mnm) | |
|-----------|--|-------------------------------------|--------------|---|---|------------------|
| | $a_{\epsilon\text{-h.c.p.}}$ (Å) | $c_{\epsilon\text{-h.c.p.}}$ (Å) | c/a ratio | $a_{\gamma\text{-f.c.c.}}$ (Å) | a_{σ} (Å) | c_{σ} (Å) |
| Initial | 2.525 | 4.102 | 1.625 | 3.578 | 8.831 | 4.800 |
| Fracture | 2.533 | 4.076 | 1.608 | 3.582 | – | – |

of Mn on the c/a ratio [82,83], thus justifying the change in the c/a ratio determined in this work.

Compared to the intrinsic c/a ratio of metals such as Ti or Mg that practically do not change during deformation [63], the c/a ratio of the metastable $\text{Fe}_{42}\text{Mn}_{28}\text{Co}_{10}\text{Cr}_{15}\text{Si}_5$ HEA decreases from ≈ 1.625 in the initial state to ≈ 1.609 upon fracture, indicating that the ϵ -h.c.p. phase expands in the a-axis and compresses in the c-axis, revealing that the $(c+a)$ slip system has a strong strain adaptation capability. The variation of the c/a ratio of the ϵ -h.c.p. phase in TRIP HEAs is essentially a dependence of the lattice parameter on the texture and stress state caused by the variation of its volume. It is a function of the dislocation density and the volume of the ϵ -h.c.p. phase, which in turn indirectly affects the activation of the different slip systems of the ϵ -h.c.p. phase [79]. This mechanistic analysis has been discussed in detail in the Discussion section.

Table 2 details that the phase fractions of both γ -f.c.c., ϵ -h.c.p. and σ phases in the metastable $\text{Fe}_{42}\text{Mn}_{28}\text{Co}_{10}\text{Cr}_{15}\text{Si}_5$ HEA before deformation were $\approx 71\%$, $\approx 28\%$ and $\approx 1\%$, respectively. After tensile fracture of the material, the γ -f.c.c. phase decreases to $\approx 17\%$, the ϵ -h.c.p. phase increases to $\approx 82\%$, while the σ volume fraction remained constant.

Before deformation, the existence of $\approx 28\%$ of ϵ -h.c.p. phase is attributed to the addition of Si, which effectively increases the metastability of the γ -f.c.c. matrix phase, as Si is an ϵ -h.c.p. phase stabilizer [10,15,69]. Moreover, it has been suggested that maximum metastability of the γ -f.c.c. phase is obtained when 5 at. % Si is added [6], as also verified by thermodynamic calculations [14]. Specifically, the higher metastability of the γ -f.c.c. phase, the lower the value of the Gibbs free energy for the γ -f.c.c. to ϵ -h.c.p. transformation ($\Delta G_{\gamma\text{-f.c.c.} \rightarrow \epsilon\text{-h.c.p.}}$) to occur, thus causing a greater driving force for the γ -f.c.c. to ϵ -h.c.p. transition, which ultimately corresponds to a reduction in the γ -f.c.c. phase fraction upon cooling to room temperature after casting.

In the current study the phase fraction volume transition which is defined as $(f_{\gamma\text{-f.c.c.}}^b - f_{\gamma\text{-f.c.c.}}^a)/f_{\gamma\text{-f.c.c.}}^b$, with $f_{\gamma\text{-f.c.c.}}^a$ corresponding to phase volume fraction of γ -f.c.c. phase after (superscript a) tensile deformation and $f_{\gamma\text{-f.c.c.}}^b$ to the volume fraction of γ -f.c.c. phase before (superscript b) deformation, was also calculated. The phase volume fraction transition of the γ -f.c.c. matrix phase before deformation and after fracture is $\approx 75\%$, which is consistent with the findings of a high phase fraction transition for an as-cast $\text{Fe}_{42}\text{Mn}_{28}\text{Co}_{10}\text{Cr}_{15}\text{Si}_5$ HEA reported by Nene et al. using TEM [14]. In addition, it was previously reported that the conversion rate of the γ -f.c.c. phase in TRIP HEAs during tensile deformation is proportional to the work hardening rate [14]. As it will be shown later, the work hardening rate of the material studied in this work is significantly higher than that measured for a $\text{Fe}_{50}\text{Mn}_{30}\text{Co}_{10}\text{Cr}_{10}$ HEA [14], which justifies the existence of a higher phase volume fraction conversion.

3.2. In-situ analysis

The engineering and true stress-strain curves (black and red lines, respectively) as well as the strain-hardening rate curve (blue line) during tensile deformation are given in Fig. 3. Based on the activation of a preferred deformation mode these curves can be divided into four stages, each one marked in Fig. 3 with the letters A, B, C and D. Each region represents a qualitative change in the deformation mechanism based on the measured diffraction data. It should be noted that the TRIP

Table 2

Volume fractions of ϵ -h.c.p. phase, γ -f.c.c. phase and σ phase in the as-cast metastable $\text{Fe}_{42}\text{Mn}_{28}\text{Co}_{10}\text{Cr}_{15}\text{Si}_5$, as obtained by Rietveld refinement.

| Phases | Volume fraction | | |
|----------|--------------------------|------------------------|--------------------------|
| | ϵ -h.c.p. phase | γ -f.c.c. phase | Sigma (σ) phase |
| Initial | $\approx 28\%$ | $\approx 71\%$ | $\approx 1\%$ |
| Fracture | $\approx 82\%$ | $\approx 17\%$ | $\approx 1\%$ |

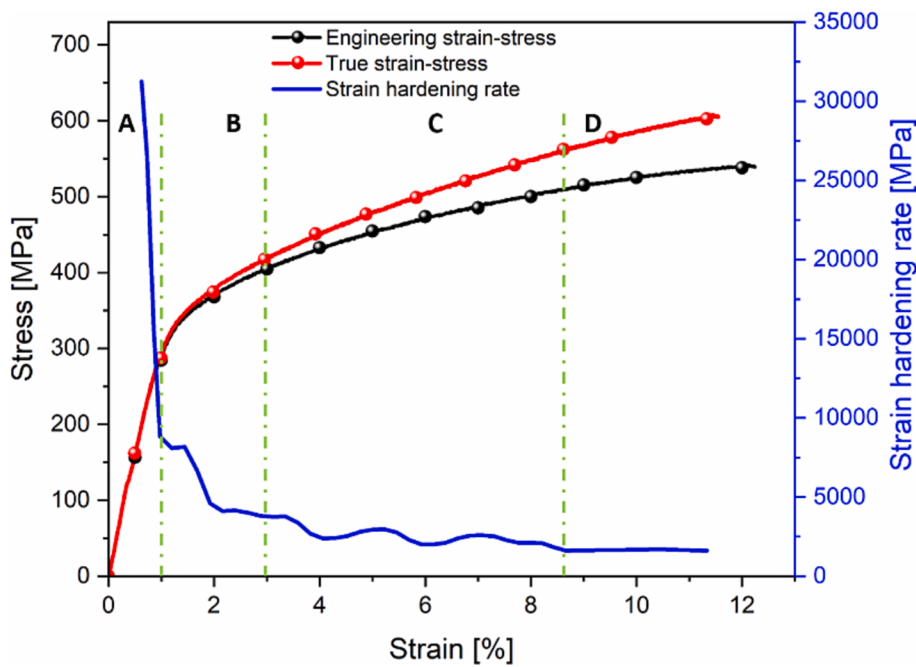


Fig. 3. Engineering and true strain–stress curves and strain hardening rate of the as-cast metastable $\text{Fe}_{42}\text{Mn}_{28}\text{Co}_{10}\text{Cr}_{15}\text{Si}_5$ HEA tested at room temperature at a strain rate of $1 \times 10^{-3} \text{ s}^{-1}$.

and TWIP effects mentioned below are further assessed in the Discussion section.

The uniform strain distribution between the metastable γ -f.c.c. phase and the resultant ϵ -h.c.p. phase in the $\text{Fe}_{42}\text{Mn}_{28}\text{Co}_{10}\text{Cr}_{15}\text{Si}_5$ HEA [14] resulted in a total elongation of $\approx 12\%$ and an yield strength of ≈ 284 MPa. The observed elongation is related to the large number of deformation twins that appear during tensile deformation, as previously shown by TEM [20]. The large number of parallel twins generated during deformation can provide sufficient twinning interfaces in the high strain region (corresponding to stages C and D, as it will be described after), thus increasing the resistance to plastic deformation, and delaying the onset of necking. Similarly, TRIP, as a key deformation mechanism of the γ -f.c.c. phase, is primarily responsible for regulating the mechanical properties of the material through the associated phase transformation. When the γ -f.c.c. to ϵ -h.c.p. phase transformation occurs, there is a corresponding transformation strain which releases the stress concentration on the interface between the two phases, thus delaying the appearance of cracks [84,85]. In addition, the activated pyramidal $<\text{c}+\text{a}>$ and $<\text{a}>$ slip systems [62,86] and the c/a ratio change [19] in the ϵ -h.c.p. phase should also be responsible for the ductile behavior exhibited by the material.

Meanwhile, compared with the $\text{Fe}_{50}\text{Mn}_{30}\text{Co}_{10}\text{Cr}_{10}$ TRIP HEA [87], the yield strength is increased by nearly 100 MPa in the alloy used in this work. However, the elongation is only one third of that of the $\text{Fe}_{50}\text{Mn}_{30}\text{Co}_{10}\text{Cr}_{10}$ counterpart. This is attributed to the fact that the metastability of the matrix γ -f.c.c. phase in the $\text{Fe}_{42}\text{Mn}_{28}\text{Co}_{10}\text{Cr}_{15}\text{Si}_5$ alloy is higher than that of $\text{Fe}_{50}\text{Mn}_{30}\text{Co}_{10}\text{Cr}_{10}$ HEA due to the addition of Si. The stacking fault energy is significantly reduced, which in turn increases the transformation rate from the soft γ -f.c.c. matrix phase to the hard ϵ -h.c.p. phase, thus increasing the yield strength of the material while sacrificing its ductility. With the emergence of the TRIP and TWIP effects, more slip systems and dislocations are activated and the interaction between dislocations provides a greater work-hardening capacity for the macroscopic deformation of the material. In addition, the existence of numerous grains and phase boundaries (as previously shown in Fig. 1) impede and difficult dislocation movement and enhance the strain accommodation capacity, thus justifying the high degree of work hardening in this HEA.

Here, the material exhibits a higher sustained work-hardening behavior related to the higher metastability of the γ -f.c.c. matrix phase on one hand, and to the appearance of deformation twins on the other hand [14,88]. The high metastability can promote the phase transformation of γ -f.c.c. to ϵ -h.c.p., as well as the twinning of the ϵ -h.c.p. phase during deformation, which are called TRIP and TWIP effects, respectively. In addition to the fact that the ϵ -h.c.p. phase is significantly harder than the γ -f.c.c. phase [10,14,69], the formation of plasticity-induced twinning of the ϵ -h.c.p. phase further helps to accommodate more strain, which has a significant effect on the work hardening. In order to investigate the nature of the TRIP effect on the strain-hardening behavior, Nene et al. [4] compared two HEAs with and without Si added ($\text{Fe}_{40}\text{Mn}_{20}\text{Co}_{20}\text{Cr}_{15}\text{Si}_5$ and $\text{Fe}_{45}\text{Mn}_{20}\text{Co}_{20}\text{Cr}_{15}$, respectively). Their results showed that the addition of Si (which increases the instability of the matrix γ -f.c.c. phase) not only increased the yield strength and improved the ductility of the material, but also improved the material work-hardening. At the same time, the TWIP effect produces deformation twins that act as barriers to dislocation movement and, to some extent, provide the material with a continuous work-hardening capacity.

Overall, the strength, ductility and work-hardening behavior exhibited by the metastable $\text{Fe}_{42}\text{Mn}_{28}\text{Co}_{10}\text{Cr}_{15}\text{Si}_5$ HEA studied in this study is mainly attributed to the γ -f.c.c. to ϵ -h.c.p. phase transformation and to deformation twinning initiated in the ϵ -h.c.p. phase due to the large deformation experienced, which is also observed in other HEAs [10,89].

The strain-hardening rate curve (blue line) shows a different slope variation (unevenness) during macroscopic deformation. This slope variation is attributed to the superiority of phase transformation (TRIP) or twinning (TWIP) dominated deformation in the material over conventional dislocation plasticity [6,14,88,91–94]. In the case of materials where the deformation mechanism is by dislocation slip only, the strain hardening rate sharply drops after the onset of plastic deformation and remains almost constant with increasing strain [94], while for TWIP/TRIP dominated deformation there are observable variations in the strain hardening rate after the onset of plastic deformation. In other words, this change in slope during tensile testing is associated with a shift from a dislocation-dominated to a multi-mechanism-dominated deformation condition. Indeed, this multi-stage work-hardening

behavior is common in low stacking fault energy alloys that exhibit secondary deformation mechanisms [4,14]. Based on the evolution of the deformation mechanisms in the material during loading, the strain hardening rate is divided into four stages, labelled with the letters A to D, which are discussed in section 4.2.

3.3. Phase stress partitioning

To further investigate the influence of the constituent phases in the metastable $\text{Fe}_{42}\text{Mn}_{28}\text{Co}_{10}\text{Cr}_{15}\text{Si}_5$ HEA on the continuous work-hardening behavior exhibited by the material, synchrotron X-ray was used to trace in real-time the dynamic stress distribution between the two dominant constituent phases (γ -f.c.c. and ϵ -h.c.p.), and the results are shown in Fig. 4. The stress imparted by the γ -f.c.c. and ϵ -h.c.p. phases varies dynamically at different stages of deformation (as shown by the A to D markings in Fig. 4). The solid blue curve is the true stress-strain curve of the HEA studied in this work; the dashed blue line is the theoretical stress-strain curve of the material, which was calculated using the mixing law for multiphase materials, using the phase volume fractions of the γ -f.c.c. and ϵ -h.c.p. phases obtained at different loading steps. The black and red dashed lines are the representative stresses imparted by γ -f.c.c. and ϵ -h.c.p. phases due to the load partitioning, which was obtained from the (311) and (10 $\bar{1}$ 2) lattice planes of γ -f.c.c. and ϵ -h.c.p. phases. The orange and green overlays refer to the range of stresses partitioned between the γ -f.c.c. and ϵ -h.c.p. phases during loading process. The upper and lower limits for each phase correspond to the stiffest and softest lattice planes, respectively, which were determined based on the elastic modulus of each lattice plane analyzed.

In this paper, for the γ -f.c.c. phase structure, the Young's modulus of the (111), (211) and (311) planes follow the order $E_{111} > E_{311} > E_{211}$ (further information will be detailed in section 4.3 corresponding to the lattice strain evolution). Thus, the upper and lower limits of the green area that make up the γ -f.c.c. phase stress range were calculated using the (111) and (211) γ -f.c.c. planes, respectively. Similarly, for the ϵ -h.c.p. phases structure we have $E_{(1011)} > E_{(1012)} > E_{(1013)}$, which also coincides with observations done in [19]. The upper and lower limits of the

corresponding ϵ -h.c.p. phase stress range (orange region) were then calculated from the (10 $\bar{1}$ 1) and (10 $\bar{1}$ 3) ϵ -h.c.p. planes, respectively.

Two key features are worth mentioning from the results depicted in Fig. 4: i) the ϵ -h.c.p. phase bears significantly more stress than the γ -f.c.c. phase, and ii) macroscopic yielding and phase yielding do not coincide. Macroscopic yielding of the alloy occurs at 287 MPa, whereas the γ -f.c.c. phase yields prematurely at 261 MPa, which contrasts to the 367 MPa for yielding of the ϵ -h.c.p. phase. These aspects will be detailed and clarified in the Discussion section. It should be noted that, unless otherwise stated, all stress values detailed in the text correspond to true stress values.

3.4. fraction evolution

The results depicted in Fig. 4 in combination with the qualitative evolution of the diffraction patterns of Fig. 2a suggest the importance of the phase change in the dynamic stress partitioning process, as determined from the X-ray diffraction experiments. To further explore the phase transformation and its kinetics, evolution of the γ -f.c.c. (black line) and ϵ -h.c.p. (red line) phase fractions were determined (refer to Fig. 5).

Except for stage A, which corresponds to the macroscopic elastic deformation, it can be perceived that transformation of γ -f.c.c. to ϵ -h.c.p. phase is occurring throughout the entire tensile test until failure. However, the conversation rate in each stage changes owing to the different predominant deformation mechanisms. This will be further highlighted and detailed in the Discussion section.

As detailed in the experimental procedure, in-situ EBSD analysis was also performed on the as-cast $\text{Fe}_{42}\text{Mn}_{28}\text{Co}_{10}\text{Cr}_{15}\text{Si}_5$ HEA. The surface microstructural evolution during tensile deformation was analyzed and the deformation-induced γ -f.c.c. to ϵ -h.c.p. phase transformation was studied. A quantitative assessment of the volume fraction evolution of γ -f.c.c. and ϵ -h.c.p. phases during the tensile process was determined. Fig. 6 presents the EBSD image quality maps and phase maps of the material at different tensile strains ($\epsilon = 0, 1, 3, 7, 9$ and 11 %). With the increase of the tensile strain, a noticeable trend emerges: the area

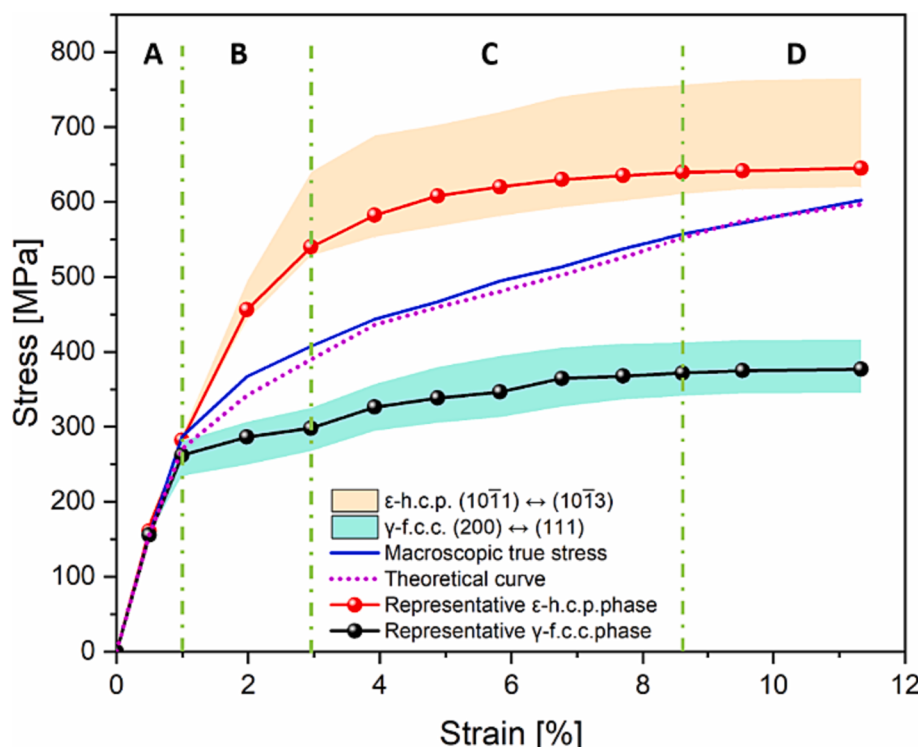


Fig. 4. Stress partitioning between γ -f.c.c. and ϵ -h.c.p. phases as a function of applied strain in the as-cast metastable $\text{Fe}_{42}\text{Mn}_{28}\text{Co}_{10}\text{Cr}_{15}\text{Si}_5$ HEA.

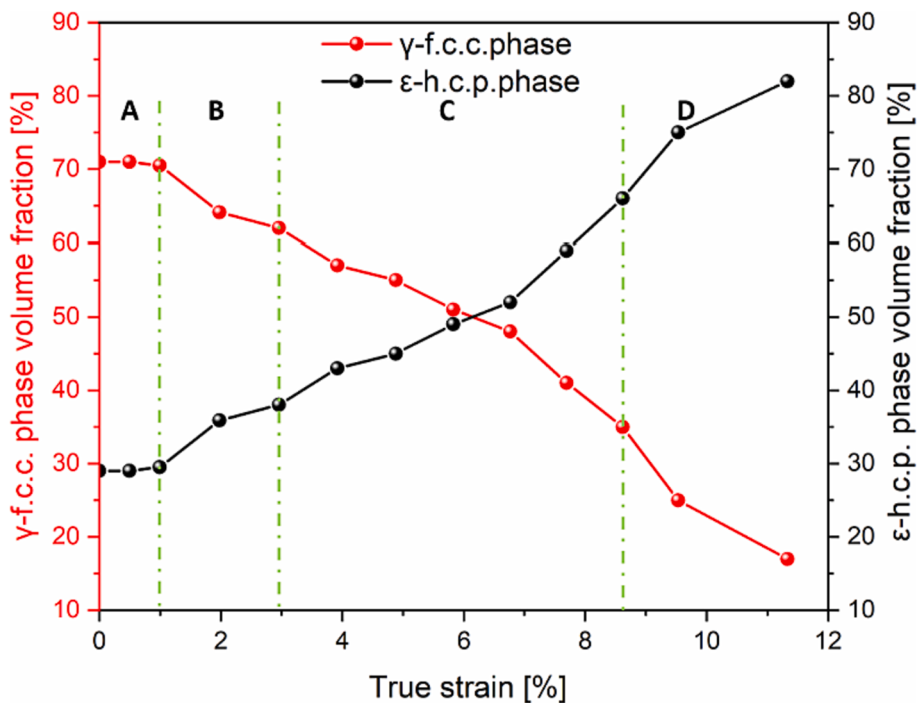


Fig. 5. Evolution of the γ -f.c.c. and ϵ -h.c.p. phase volume fractions in the as-cast metastable $\text{Fe}_{42}\text{Mn}_{28}\text{Co}_{10}\text{Cr}_{15}\text{Si}_5$ HEA obtained from synchrotron X-ray diffraction data.

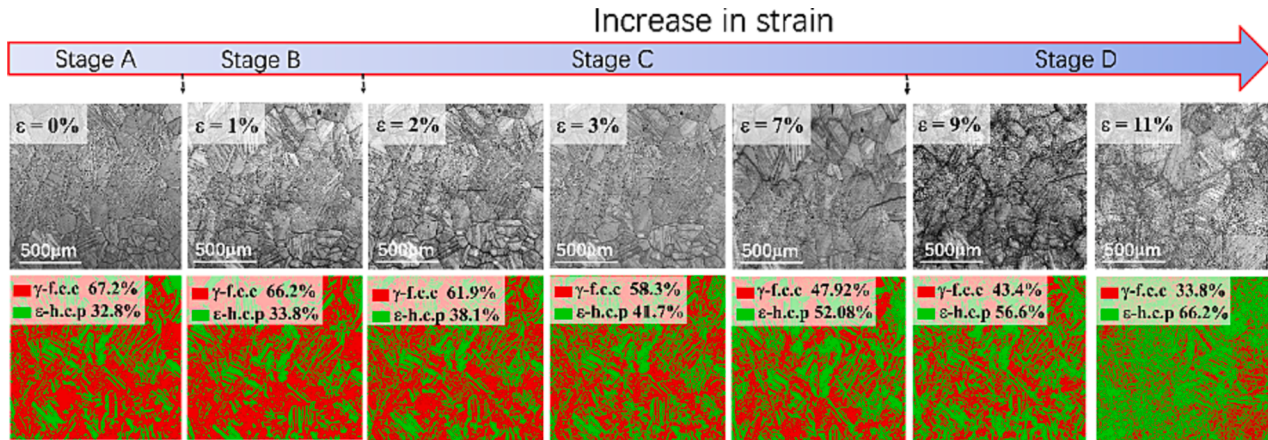


Fig. 6. Evolution of the γ -f.c.c. and ϵ -h.c.p. phase volume fractions in the as-cast metastable $\text{Fe}_{42}\text{Mn}_{28}\text{Co}_{10}\text{Cr}_{15}\text{Si}_5$ HEA obtained from in-situ experiments.

occupied by the γ -f.c.c. phase (in red color) gradually decreases, whereas the region attributed to the ϵ -h.c.p. phase (in green color) increases. This observable phenomenon strongly suggests that as the applied tensile strain varies, the material experiences a notable crystal structure phase transformation from γ -f.c.c. to ϵ -h.c.p.. By comparison, the trends of the phase fractions obtained by EBSD and synchrotron X-ray diffraction are consistent with each other (Fig. 5 and Fig. 6), which will be further discussed in subsection 4.2.5.

3.5. Dislocation density, stacking faults probability and stacking faults interspacing evolution

Fig. 7 reproduces the dynamic evolution of the dislocation density of the $\text{Fe}_{42}\text{Mn}_{28}\text{Co}_{10}\text{Cr}_{15}\text{Si}_5$ metastable HEA along the LD, TD, and as obtained from full azimuthal integration of the synchrotron X-ray diffraction data. As can be seen from Fig. 7, the dislocation density evolution in the γ -f.c.c. and ϵ -h.c.p. phases during tensile loading is also

dependent on the deformation mechanism experienced by the material. The dislocation density shows an increasing trend with increasing tensile loading in both the γ -f.c.c. and ϵ -h.c.p. phases. Moreover, the dislocation density in the γ -f.c.c. phase is always above that in the ϵ -h.c.p. phase regardless of the orientation considered (LD, TD or full azimuthal), as shown in Fig. 7a–c). This is fundamental for the TRIP effect to be activated and proceed during material deformation and will be further detailed in the Discussion section. The dislocation density (refer to Fig. 7 c)) obtained by full azimuthal integration can be treated as an average distribution over the whole material. Thus, focus is given on the dislocation density obtained from full azimuthal integration to investigate its dynamic evolution during the loading process.

The introduction of nanoscale stacking faults provide a barrier to dislocation movement and increase the strength of the material without sacrificing plasticity, thus making stacking faults highly attractive for improving the mechanical properties of the metastable HEA. Therefore, to further investigate the dynamic evolution response of stacking faults

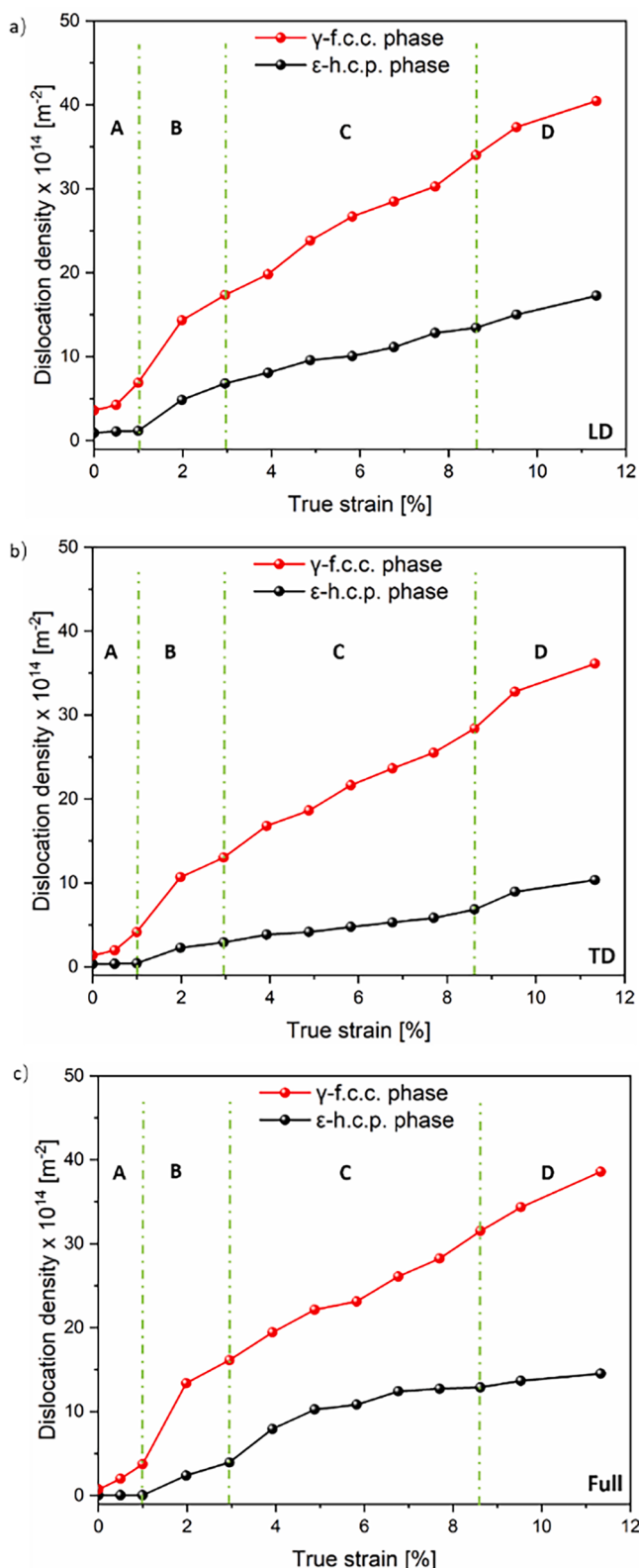


Fig. 7. a), b) and c) dislocation density as a function of True strain along LD, TD, and full azimuthal integration, respectively.

during tensile deformation, the contribution of these microstructural features to the material work-hardening behavior and the origin of macroscopic strength and ductility needs to be properly understood. Fig. 8 reproduces the evolution of the stacking faults interspacing, L_{sf} , and stacking faults probability, P_{sf} , the latter being a measure of

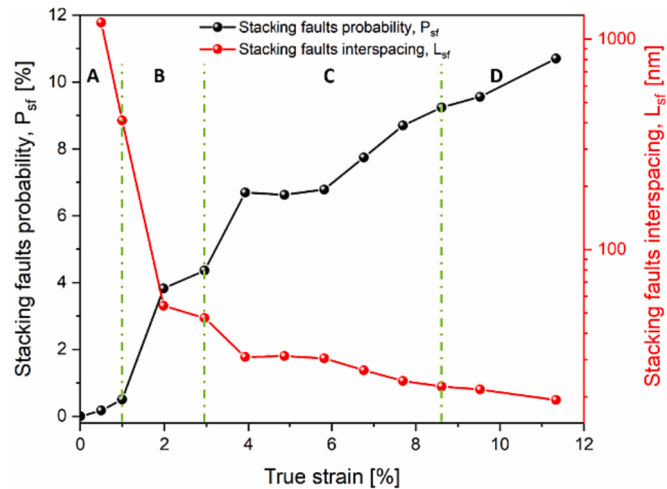


Fig. 8. Evolution of stacking faults probability, P_{sf} , and stacking faults interspacing, L_{sf} obtained from synchrotron X-ray diffraction data.

deformation faulting which is defined as the probability of finding a deformation fault between any two layers in the γ -f.c.c. stacking sequence, with tensile strain.

Fig. 9 illustrates the Kernel Average Misorientation (KAM) maps of the same region during the tensile process, as determined from the in-situ EBSD measurements. KAM maps are employed to assess the evolution of local strain distribution during deformation. Higher KAM values indicate a higher accumulation of dislocations resulting from the imposed plastic deformation.

To gain a deeper understanding of the evolution of dislocation density within the two matrix phases (γ -f.c.c. and ϵ -h.c.p.) during the deformation process, Fig. 9 also presents the Geometrically Necessary Dislocation (GND) maps for these phases at different strain levels (0, 1, 3, 7, 9, and 11 %). Considering the limitations of EBSD measurements, which include a relatively small detection area and its surface-sensitive nature that restricts its capacity to fully, i.e., in bulk, capture comprehensive plastic deformation information across the entire material, this technique can only capture microstructure information near the sample's surface. As a result, the deformation analysis extracted from EBSD data, including KAM maps and the evolution of average GND values for the γ -f.c.c. and ϵ -h.c.p. phases during the deformation process, is employed solely as qualitative references rather than quantitative ones. As expected, the evolving trend of the KAM values across the entire sample (refer to Fig. 9) reveals an increase in the localized dislocation density with the gradual increment in tensile strain. By comparing the average GND values within the γ -f.c.c. and ϵ -h.c.p. phases, it is distinctly evident that the localized dislocation density within the γ -f.c.c. phase consistently surpasses that within the ϵ -h.c.p. phase. The observation can be attributed to the inherent soft and hard characteristics of the γ -f.c.c. and ϵ -h.c.p. phases, as well as their distinct mechanical response behaviors. These aspects will be further expanded in the discussion section.

3.6. Intensity evolution

Ghaghouri et al. [95] reported that in-situ neutron diffraction can be used to study the propagation of deformation twinning, by tracing the characteristic intensity variations of certain (hkl) diffraction reflections corresponding to the "parent grains" (i.e., grains undergoing deformation twinning) and the "twinned" (i.e., twinned parent grains) crystal families. Likewise, synchrotron X-ray diffraction can be used for the same purpose, and this was used to further investigate the deformation mechanisms within the ϵ -h.c.p. phase of the $\text{Fe}_{42}\text{Mn}_{28}\text{Co}_{10}\text{Cr}_{15}\text{Si}_5$ HEA. the variation in the diffracted intensity of certain ϵ -h.c.p. planes along LD and TD during tensile loading was used to demonstrate the onset of

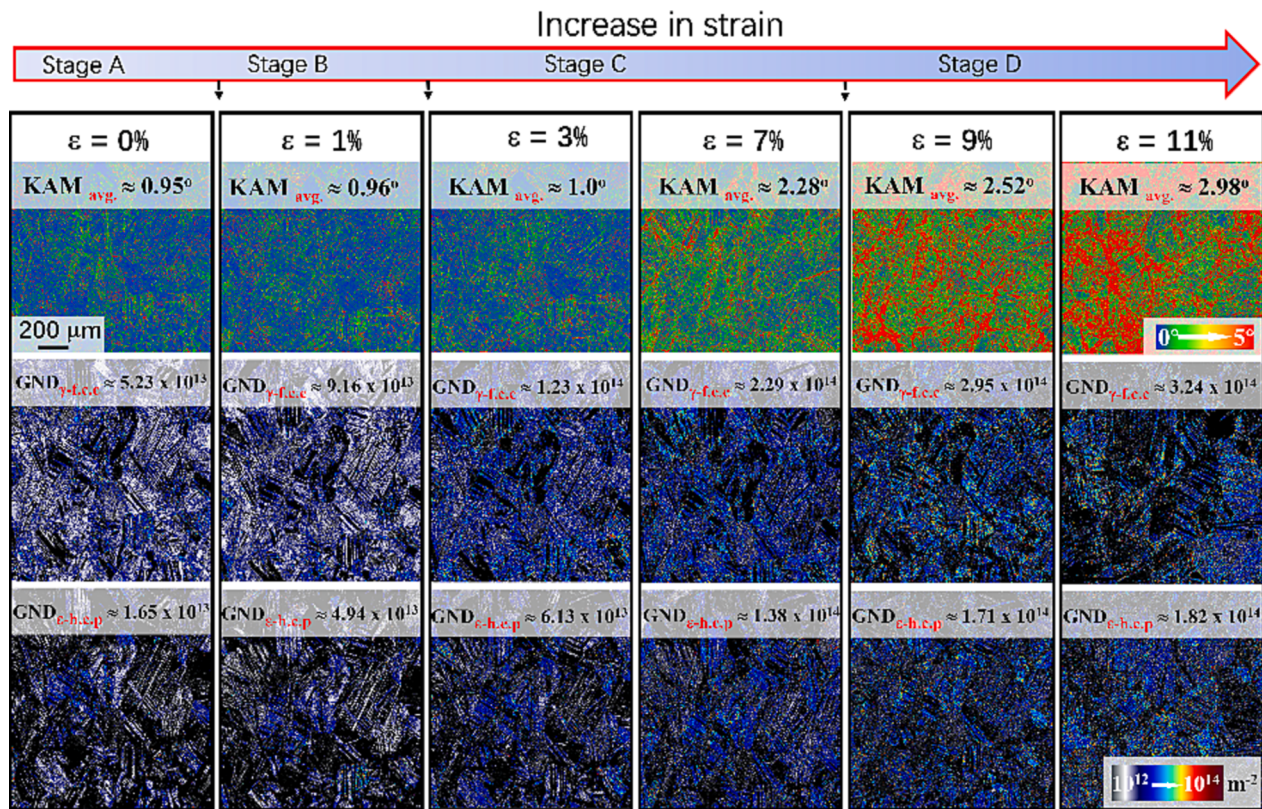


Fig. 9. Evolution of KAM maps, average of GND values for the γ -f.c.c. and ϵ -h.c.p. phase under different loading obtained from in-situ EBSD experiments.

TWIP, as well as the evolution and transition of single-twinning (by tensile twinning) to multi-twinning (with the onset of compression twinning).

In terms of the microscopic mechanisms of twinning, three factors affect the type of twinning in the ϵ -h.c.p. phase, i) c/a ratio, ii) type of loading, and iii) crystal orientation [96]. The c/a ratio must be below the ideal value of 1.633 for twinning to occur. The type of loading is related to the imposition of tensile or compression, or in more complex cases, with multiaxial loadings. Evaluation of different crystal orientations enables to determine if the twinning deformation is tensile or compressive in nature. In fact, the $(10\bar{1}2)$ plane can be used to evaluate the onset of tensile twinning, while $(10\bar{1}3)$ and $(10\bar{1}1)$ planes can be used to record compression twinning. ϵ -h.c.p. grains are difficult to compress along the c-axis, thus the orientation of the c-axis with respect to the loading direction determines the type of twinning, which is activated within a single family of grains, especially the type of twinning modes, i.e., tensile, or compressive, and its range.

We use synchrotron diffraction to reveal the onset and range of TWIP in the $\text{Fe}_{42}\text{Mn}_{28}\text{Co}_{10}\text{Cr}_{15}\text{Si}_5$ HEA by quantitatively analyzing the diffraction intensity evolution of several differently oriented ϵ -h.c.p. grains. Fig. 10 a), c), e) and g) depict the normalized diffracted intensities of the $(10\bar{1}1)$, $(10\bar{1}2)$ and $(10\bar{1}3)$ ϵ -h.c.p. planes along the LD and TD during tensile loading as a function of the true stress. Fig. 10 b), d), f) and h) show the above-mentioned diffraction intensities of the same ϵ -h.c.p. grains as a function of true tensile strain along the LD and TD during tensile deformation. Note that the initial value of the normalized diffracted intensity, I_0 , corresponds to the peak intensity of the analyzed with no load imposed. It is clear that within stages A and B there are no evident changes, in opposition to what occurs in stages C and D. As it will be shown this is related to the activation of tensile and compression twinning.

3.7. Lattice strain evolution

Evaluating the lattice strain evolution along different directions during macroscopic loading can provide insights into the micro-mechanical behavior and load-dependent response of the phases that constitute the metastable $\text{Fe}_{42}\text{Mn}_{28}\text{Co}_{10}\text{Cr}_{15}\text{Si}_5$ HEA. Moreover, the (hkl) -dependent behavior can provide information on the load partitioning between different lattice planes and how this is affected by both TWIP and TRIP effects. Fig. 11 a) and b) depict the evolution of lattice strain as a function of true stress (refer to Fig. 11 a)) and true strain (refer to Fig. 11 b)) for the (111) , (200) and (311) γ -f.c.c. planes along the LD and TD. Similarly, Fig. 11 c) and d) display the mechanical response of the $(10\bar{1}0)$, $(10\bar{1}1)$, $(10\bar{1}2)$ and $(10\bar{1}3)$ ϵ -h.c.p. planes along the LD and TD in relation to the true stress (refer to Fig. 11 c)) and the true strain (refer to Fig. 11 d)). The lattice strain evolution in each plane was divided into the same A, B, C, and D stages which mark different predominant deformation modes experienced by the material, as described in detail in section 4.2.

For both phases a positive lattice strain developed along LD and a negative lattice strain developed along TD, the latter being due to the Poisson effect. It is also observed that the soft planes for the γ -f.c.c. and ϵ -h.c.p. phases are the (200) and $(10\bar{1}0)$, respectively, while the stiffest are the (111) and the $(10\bar{1}3)$. It can be observed that the lattice strain evolution experiences significant changes when transitioning from one stage to another in both phases. This is related to deformation slip, TRIP and/or TWIP being the main deformation mechanisms occurring at a given loading step.

3.8. c/a ratio evolution

To explore the various deformation modes in the ϵ -h.c.p. phase of the currently studied $\text{Fe}_{42}\text{Mn}_{28}\text{Co}_{10}\text{Cr}_{15}\text{Si}_5$ metastable HEA, the changes in the ϵ -h.c.p. phase lattice parameters, $a_{\epsilon\text{-h.c.p.}}$ and $c_{\epsilon\text{-h.c.p.}}$, during the

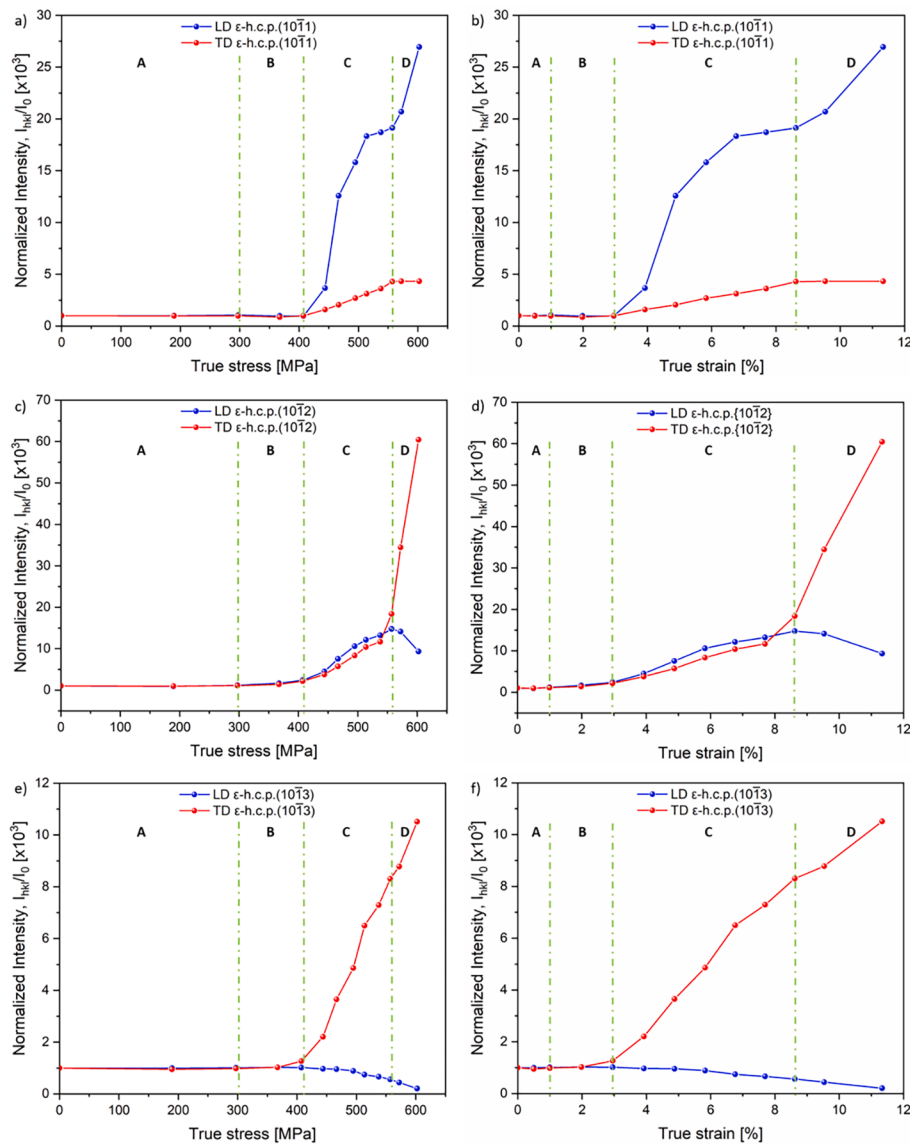


Fig. 10. Normalized diffraction intensity evolution of the different ϵ -h.c.p. planes along LD and TD as a function of, a), c) and e) true stress, and b), d) and f) true strain.

tensile deformation are shown in Fig. 12 a). Fig. 12 b) provides details on the variation of the ϵ -h.c.p. c/a ratio with increasing applied tensile loading.

During tensile deformation at a fixed strain rate, the decrease in the ϵ -h.c.p. c/a ratio with applied tensile loading is attributed to lattice expansion along the a-axis and compression along the c-axis. This is reflected in the lattice constants evolution, where the ϵ -h.c.p. phase lattice parameter a and c tend to increase and decrease, respectively, as shown in Fig. 12 a).

Frank et al. [19] performed in-situ neutron diffraction analysis of a $\text{Fe}_{40}\text{Mn}_{20}\text{Cr}_{15}\text{Co}_{20}\text{Si}_5$ HEA under tensile deformation, and detailed c/a ratio decrease of the ϵ -h.c.p. c/a ratio from 1.619 to 1.588 with increasing strain, which was attributed to the activation of the non-basal pyramidal $\langle c+a \rangle$ slip system and to deformation twinning that can accommodate strain along the c-axis at larger strain levels. The processing and deformation dependence of the ϵ -h.c.p. c/a ratio in TRIP HEAs was also observed in our metastable $\text{Fe}_{42}\text{Mn}_{28}\text{Co}_{10}\text{Cr}_{15}\text{Si}_5$ HEA, where a reduction in the ϵ -h.c.p. c/a ratio from 1.625 to 1.609 was observed (refer to Fig. 12 b). Previous work by Sinha et al. [79] studied the ϵ -h.c.p. c/a ratios of five HEAs, ($\text{Fe}_{44}\text{Mn}_{28}\text{Co}_{10}\text{Cr}_{15}\text{Si}_3$, $\text{Fe}_{42}\text{Mn}_{28}\text{Co}_{10}\text{Cr}_{15}\text{Si}_5$, $\text{Fe}_{40}\text{Mn}_{20}\text{Co}_{20}\text{Cr}_{15}\text{Si}_5$, $\text{Fe}_{39}\text{Mn}_{20}\text{Co}_{20}\text{Cr}_{15}\text{Si}_5\text{Al}_1$ and

$\text{Fe}_{38.5}\text{Mn}_{20}\text{Co}_{20}\text{Cr}_{15}\text{Si}_5\text{Cu}_{1.5}$), showing that the variation of the c/a ratio is attributed to a combination of chemistry, responsive phase evolution, elastoplastic deformation characteristics and transformation volume change. Depending on the c/a ratio, the ϵ -h.c.p. phase can deform not only via basal slip, but also on a number of non-basal slip carriers, which helps to accommodate more strain, and also enable to overcome the strength-ductility paradigm. This is completely different from most conventional ϵ -h.c.p. structural alloys such as Mg, where their c/a ratio remains almost constant during deformation, and thus only pure basal $\langle c+a \rangle$ slip occurs [63,97], being one of the reasons why these alloys possess lower plasticity.

3.9. Strengthening contributions

In Fig. 13, the black, red, and blue dotted lines represent the dislocation strengthening of the ϵ -h.c.p. ($\sigma_{\epsilon-\text{h.c.p. DIS}}$) and γ -f.c.c. ($\sigma_{\gamma-\text{f.c.c. DIS}}$) phases, as well as the stacking faults strengthening of the γ -f.c.c. phase ($\sigma_{\gamma-\text{f.c.c. SF}}$), respectively. The dashed and solid orange lines detail the calculated strengthening contribution (σ_{Calc}) and the macroscopic tensile stress-strain response (σ_{Macro}), respectively. The orange dashed line is the linear summation of all the strengthening contributions.

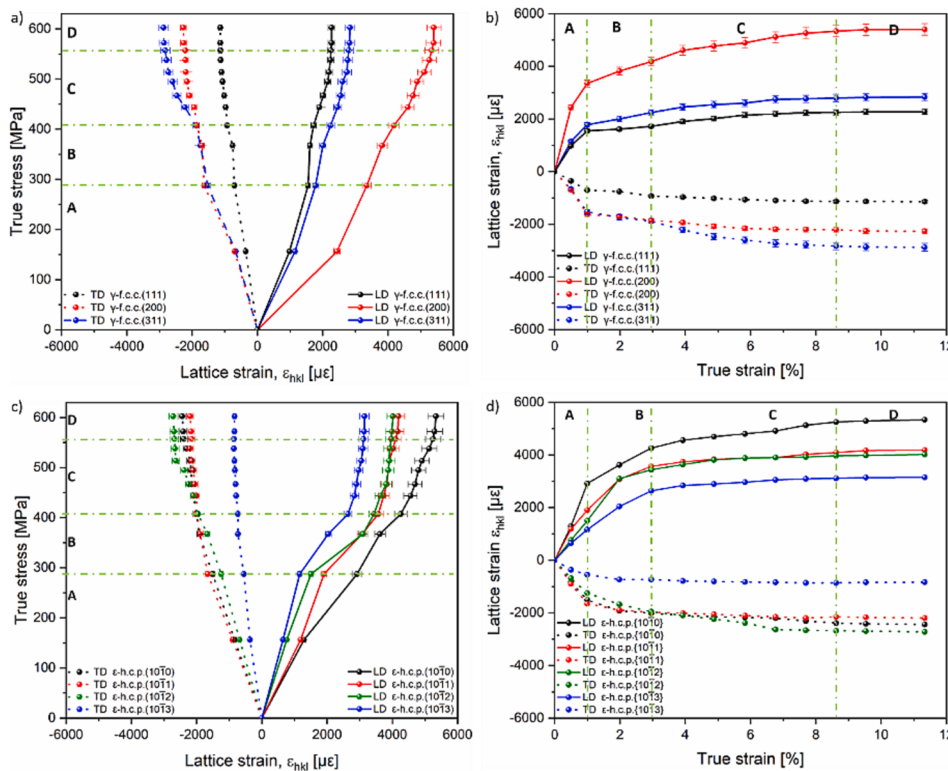


Fig. 11. Lattice strain evolution along the loading direction (LD) and transverse direction (TD) as a function of applied true stress (a, c) and true strain (b, d) for γ -f.c.c. (a, b) and ϵ -h.c.p. phases (c, d).

Moreover, the difference between σ_{Macro} and σ_{Calc} , is defined here as σ_{Extra} which represents the strengthening contributions arising from, i) solid solution strengthening, ii) precipitation strengthening due to the presence of σ phase, and iii) the Hall-Petch strengthening resulting from changes in the interface spacing. These contributions are not quantified as these are expected to remain constant during tensile deformation of the metastable HEA.

Since the dislocation density in both γ -f.c.c. and ϵ -h.c.p. phases, and the amount of stacking faults in the γ -f.c.c. phase vary significantly during deformation (refer to Fig. 7 b) and Fig. 8), it is possible to define the calculated stress, σ_{Calc} , in the currently studied HEA as follows,

$$\sigma_{\text{Calc}} = \sigma_{\gamma-\text{f.c.c. DIS}} + \sigma_{\epsilon-\text{h.c.p. DIS}} + \sigma_{\gamma-\text{f.c.c. SF}}, \quad (30)$$

where $\sigma_{\gamma-\text{f.c.c. DIS}}$ and $\sigma_{\epsilon-\text{h.c.p. DIS}}$ are the strengthening contributions in both the γ -f.c.c. and ϵ -h.c.p. due to dislocations, while $\sigma_{\gamma-\text{f.c.c. SF}}$ is the contribution of the stacking faults generated in the γ -f.c.c. phase. The difference between the macroscopic stress imparted by the alloy, σ_{Macro} , and σ_{Calc} is defined by σ_{Extra} as detailed in Equation (31) and encompasses the strengthening contributions that are kept constant during loading,

$$\sigma_{\text{Extra}} = \sigma_{\text{Macro}} - \sigma_{\text{Calc}} \quad (31)$$

Overall, the evolution of the three major strengthening contributions ($\sigma_{\gamma-\text{f.c.c. DIS}}$, $\sigma_{\epsilon-\text{h.c.p. DIS}}$ and $\sigma_{\gamma-\text{f.c.c. SF}}$) exhibit all a continuous increase with increasing deformation. However, depending on the deformation mechanism that is predominant at a given time (stages A to D) the magnitude of each strengthening contribution is modified. These aspects will be further detailed in section 4.2.

In terms of the magnitude of the strengthening contribution, the dislocation strengthening contribution of the γ -f.c.c. phase is the highest. The strengthening effect induced by dislocations and stacking faults within the ϵ -h.c.p. phase are of similar magnitude with one another.

4. Discussion

Leveraged on the results and descriptions presented in the previous section, we now focus on detailing and discussing the microstructure evolution of the metastable $\text{Fe}_{42}\text{Mn}_{28}\text{Co}_{10}\text{Cr}_{15}\text{Si}_5$ HEA. A full section is devoted to the analysis of the four deformation stages (A to D) to clearly highlight the predominant deformation mechanism during each loading step.

4.1. Microstructure characterization and phase identification

As observed in Fig. 1, the γ -f.c.c. grains are divided by laths of ϵ -h.c.p. in various directions. Further observation of the microstructural features presented in Fig. 1, show that these lath morphologies are limited to a single grain and no cross-over to other grains occurs. This will generate γ -f.c.c./ ϵ -h.c.p. boundaries (shown by black arrows), which combined with the γ -f.c.c./ γ -f.c.c. grain boundaries (shown by pink arrows) and ϵ -h.c.p./ ϵ -h.c.p. boundaries (pointed by yellow arrows) can improve the material work-hardening by piling up of dislocations and stacking faults. The ϵ -h.c.p./ ϵ -h.c.p. boundaries are formed by pairs of ϵ -h.c.p. laths that intersect each other. Moreover, some of the ϵ -h.c.p. laths do not fully cross a γ -f.c.c. single grain where they originate from, as shown by the purple arrow, indicating that incomplete growth of certain laths occurred.

The coexistence of multiple boundaries in the metastable $\text{Fe}_{42}\text{Mn}_{28}\text{Co}_{10}\text{Cr}_{15}\text{Si}_5$ alloy is observed prior and after tensile loading. To the thermally stable ϵ -h.c.p. phase that exists in the material prior to loading (see Fig. 1 a)), it is observed the massive formation of strain-induced ϵ -h.c.p. phase due to TRIP, which generated significantly more interfaces during tensile loading (refer to Fig. 1 b)). Concomitant with the larger amount of ϵ -h.c.p. phase being formed due to TRIP, there is also a dramatic decrease in the lath spacing, which is also aided by TWIP [10, 67, 69, 98, 99].

Observation from the superimposed diffraction data in Fig. 2 a),

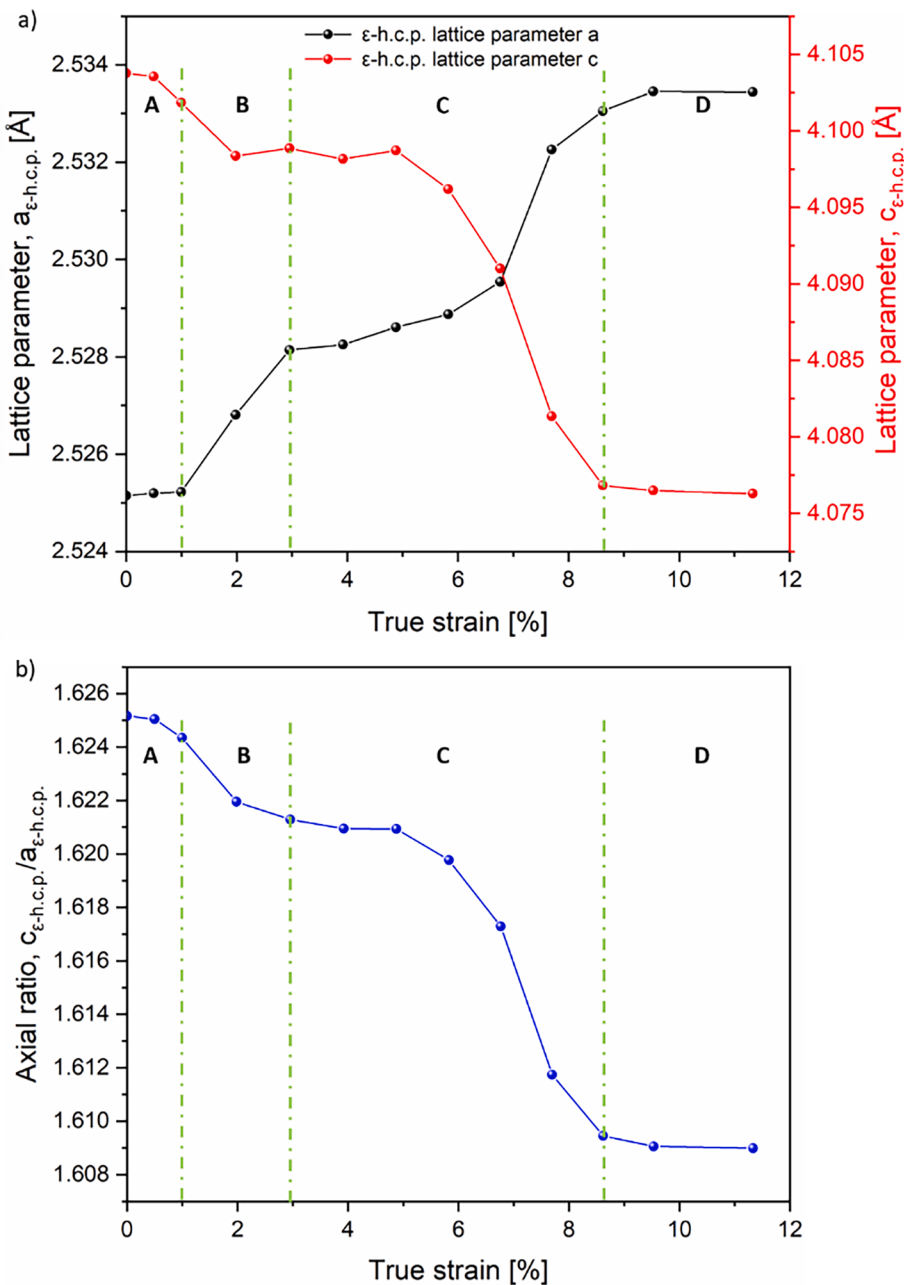


Fig. 12. a) Evolution of a and c lattice parameters in the ϵ -h.c.p. phase as a function of true strain, and b) deformation induced decrease in the c/a ratio of the ϵ -h.c.p. phase in the metastable $\text{Fe}_{42}\text{Mn}_{28}\text{Co}_{10}\text{Cr}_{15}\text{Si}_5$ HEA.

details that no new phases other than the γ -f.c.c., ϵ -h.c.p. and σ phases are formed upon loading. The γ -f.c.c. and ϵ -h.c.p. phases are the dominant structures, with a volume fraction prior to loading of 71 and 28 %, respectively, which is consistent with the phase constitution measured via EBSD by Nene et al. [14]. In HEAs of the Fe-Mn-Co-Cr system, the addition of Si and Cr increases the tendency for σ phase to form [4,66]. Nene et al. detected the presence of Fe- and Cr-rich σ with a tetragonal structure in a $\text{Fe}_{42}\text{Mn}_{28}\text{Co}_{10}\text{Cr}_{15}\text{Si}_5$ HEA [81], which is consistent with our phase identification.

The phase fraction measured at the end of the tensile loading (refer to Table 2) revealed a significant increase of ϵ -h.c.p. (up to 82 %) at the expense of γ -f.c.c. (decreasing to 17 %), which is indicative of the TRIP effect and in good agreement with the qualitative evaluation of the superimposed diffraction data of Fig. 2 a) and optical microscopy analysis of Fig. 1. The dynamic evolution of the phase fraction during

tensile loading will be discussed in section 4.2.

4.2. Deformation mechanisms

Based on the changes of the deformation mechanisms in the as-cast $\text{Fe}_{42}\text{Mn}_{28}\text{Co}_{10}\text{Cr}_{15}\text{Si}_5$ HEA during tensile loading it is possible to identify four distinct deformation regimes. These were marked by the letters A ($\varepsilon < 1.0\%$), B ($1.0\% < \varepsilon < 3.0\%$), C ($3.0\% < \varepsilon < 7.7\%$) and D ($\varepsilon > 7.7\%$), matching to the various trigger stress points for the onset of distinct deformation mechanisms. The trigger stress points for each stage are 0, 287, 407 and 557 MPa, for stages A to D, respectively, and in each the following deformation mechanisms are active, stage A) elastic deformation and dislocation slip in the γ -f.c.c. phase, stage B) dislocation slip + TRIP, stage C) dislocation slip + TRIP + TWIP (single twinning mode), and stage D) dislocation slip + TRIP + TWIP (multiple

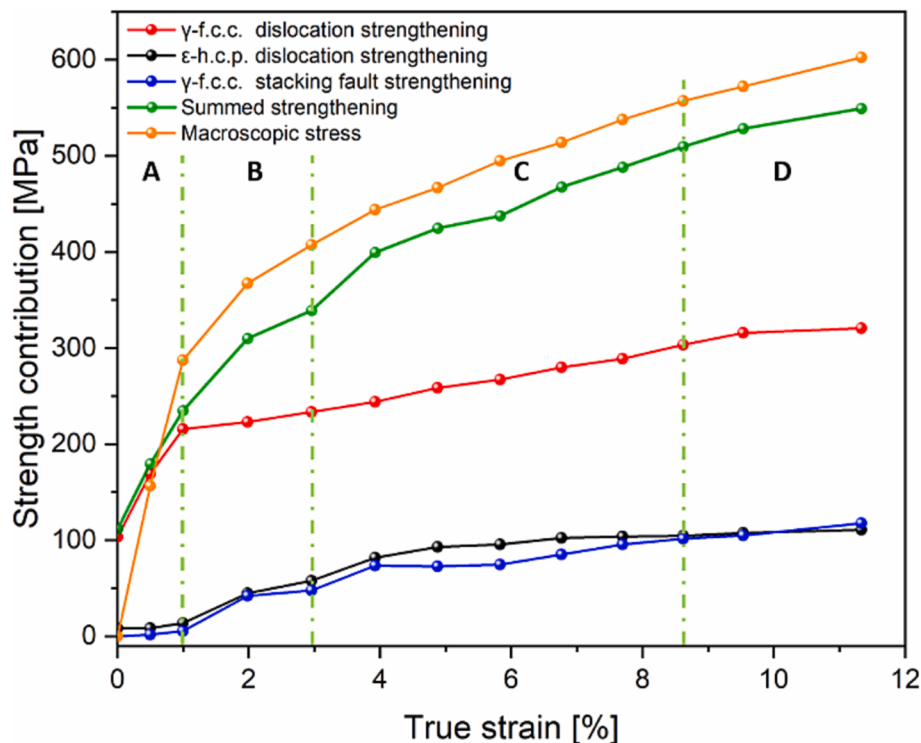


Fig. 13. Evolution of the strengthening contributions of γ -f.c.c. and ϵ -h.c.p. phases as a function of true strain.

twinning modes). A detailed discussion for each stage is presented next.

4.2.1. Stage A – macroscopic elastic deformation

Stage A, corresponding to low strain regime in Fig. 3 ($\epsilon < 1.0\%$), encompasses the macroscopic elastic deformation of the material. During stage A, there is almost no divergence in the load distribution of the main constituent phases of the Fe₄₂Mn₂₈Co₁₀Cr₁₅Si₅ HEA, as shown in Fig. 4. The stress imparted by both γ -f.c.c. and ϵ -h.c.p. phases grow linearly with increasing load. A closer look shows that the γ -f.c.c. phase structure yields first at about 261 MPa (lower than the macroscopic material yield point 284 MPa), while the ϵ -h.c.p. phase showed no signs of yielding at stage A. It is important to note is that the yielding stresses of different lattice planes will necessarily vary, as it will be discussed in detail in section 4.3. Here, we are only analyzing the phase-dependent macroscopic response, as shown by the red and black dotted lines of Fig. 4. Therefore, when there is macroscopic evidence of material yielding, the γ -f.c.c. phase has already yielded, while the ϵ -h.c.p. phase is still in the elastic deformation stage, and part of the load begins to be transferred from the soft γ -f.c.c. phase to the hard ϵ -h.c.p. phase. 284 MPa not only corresponds to the macroscopic yield point of the HEA, but also marks the onset for the γ -f.c.c. \rightarrow ϵ -h.c.p. phase transformation (refer to Fig. 5), which will be analyzed in the next section. This change the stress-strain response of the material, which are consistent with the basic features of the TRIP deformation mechanism [100], promotes significant stress redistribution after yielding. Therefore, besides the soft and hard behaviors of the γ -f.c.c and ϵ -h.c.p. phases, which influence the stress partitioning, the formation of the plastically-induced ϵ -h.c.p. phase from the metastable γ -f.c.c. also requires continuous stress increase to promote plastic deformation and continue the TRIP effect, thus ensuring intergranular and interphase stress coordination in the microstructure [101], which is also the reason why the ϵ -h.c.p. phase can maintain continuous hardening [102].

Stage A is dominated by perfect dislocation slip due to the γ -f.c.c. phase premature yielding. In fact, as it was shown in section 3.5, resulting for the early yielding of the γ -f.c.c. phase in stage A, there is a concomitant increase in the dislocation density (from 7.3×10^{13} to $3.7 \times$

10^{14} m^{-2}). On the other hand, since the ϵ -h.c.p. phase is only elastically deformed (its yielding occurs at 287 MPa), there is no change in the dislocation density of this phase (kept at $3.8 \times 10^{13} \text{ m}^{-2}$). The increase in dislocation density in the γ -f.c.c. phase can help in the nucleation of the ϵ -h.c.p. phase upon the imposition of macroscopic plastic deformation [103]. This stage is also controlled by the evolution of dislocation density without formation of twins. In fact, dislocation entanglement and twinning do not occur, but perfect dislocation slip and overlapping stacking faults often appear [58].

In stage A, the stacking faults probability increases from ≈ 0.17 to $\approx 0.52\%$ during macroscopic elastic deformation and a significant reduction in the stacking faults interspace was determined. As the strain increases, the L_{sf} decreases sharply from ≈ 1199 to ≈ 411 nm, which in combination with the increase in stacking faults probability serves to demonstrate that stacking faults are being formed during macroscopic elastic deformation of the material. More importantly, the presence of stacking faults and the reduction in their interspacing can reduce the free path for dislocation movement. Therefore, the increase of stacking faults probability and decrease of stacking faults interspacing will facilitates the effective accumulation of dislocations in the γ -f.c.c. phase [104] leading to an increase in the dislocation density within the macroscopic elastic regime, which will eventually facilitate the TRIP effect. Thus, it can be stated that stage A is mainly controlled by the perfect dislocation slip of the γ -f.c.c. phase, as well as overlapping of stacking faults without occurrence of twinning [58]. The fact that TRIP does not occurs upon yielding of the macroscopic material is related to the need for the accumulation of stacking faults during stage A, which will act as nuclei for the strain-induced transformation that will take place in stage B.

The onset for macroscopic plastic deformation and entry in stage B is the trigger point for the TRIP effect to occur. Prior to that, the transformation of f.c.c. and ϵ -h.c.p. does not occurs, as also evidenced by the constant volume fraction of both phases in this stage (refer to Fig. 5). The phase transformation kinetics of γ -f.c.c. to ϵ -h.c.p. is mainly determined by the applied stress and by the existence (or not) of plastic deformation. Moreover, it is well known that the nucleation and growth of the ϵ -h.c.p.

phase is accomplished by a large number of stacking faults [105].

The normalized diffraction intensity of the ϵ -h.c.p. phase along both the LD and TD in stage A details no changes for the selected diffraction planes (refer to Fig. 10), which is related to the pure elastic deformation and perfect dislocation slip of this phase in stage A. The non-splitting of diffracted intensity in both the TD and LD reveals that no twinning of the ϵ -h.c.p. grains occurs in the stage A. These findings provide a basis for exploring the slip mechanisms of the ϵ -h.c.p. phase based on the c/a ratio which is discussed next.

The ϵ -h.c.p. c/a ratio is almost practically constant (1.625 vs 1.624) in stage A as seen in Fig. 12 b). It is well known that the c/a ratio is closely related to the slip system [106]. When the c/a ratio is greater than the ideal value of 1.633, mainly basal $< a >$ slip is the dominant in plastic deformation mechanism. In contrast, when the c/a ratio is lower than the ideal value of 1.633, the probability for the non-basal pyramidal $< c + a >$ slip being dominant is higher. Moreover, c/a ratios below the ideal value also aids in the development of twinning as a deformation mechanism. Throughout this stage, although the c/a ratio is lower than ideal value, the basal $< a >$ slip and non-basal pyramidal $< c + a >$ slip have not been activated at this stage. Such is related to the pure elastic deformation experienced by the ϵ -h.c.p. in stage A and explains the constant dislocation density (see Fig. 7).

Based on the above analysis, during the macroscopic elastic loading, the main deformation mechanism is dislocation slip which occurs in the γ -f.c.c. phase that yields prematurely at 261 MPa. The ϵ -h.c.p. phase remains elastically deformed, leading to the differences in the evolution of the dislocation density among both phases.

4.2.2. Stage B – onset of TRIP

When the material enters stage B ($1.0\% < \varepsilon < 3.0\%$) the deformation mechanism is dominated by the TRIP effect, i.e., the phase transition from γ -f.c.c. to the ϵ -h.c.p. takes place, as it can be evidenced by the evolution of the phase volume fraction in Fig. 5). It is well known that TRIP is the main deformation mechanism regulator in the γ -f.c.c. phase, aside from dislocation slip [6,10,14,107]. In this study, the trigger point for the onset of TRIP corresponds to the macroscopic yield strength of 287 MPa. There is a significant decrease in the rate of decline of the strain hardening rate during this stage (refer to Fig. 3). The ups and downs of the strain-hardening curve in stage B can be explained by two concurring effects: the transformation of γ -f.c.c. to ϵ -h.c.p. and the nucleation of twins, which will trigger TWIP in stage C. This nucleation of twins is expected to occur mainly at the plateau regions of stage B [108].

Throughout stage B, the phase stress partitioning evolution in the γ -f.c.c. phase has a small increase in its hardening rate after yielding, as shown in Fig. 4, which is mainly attributed to the phase transformation that introduces new phase boundaries in the γ -f.c.c. matrix, thereby reducing the mean free path for dislocation movement. This results in a sharp increase in dislocation density at this stage as shown in Fig. 7 f), increasing the storage capacity of dislocations and hence the hardening behavior. The ϵ -h.c.p. phase exhibits a more significant work-hardening behavior than the γ -f.c.c., thus having a greater impact on the macroscopic work-hardening behavior exhibited by the studied metastable HEA. As it can be seen, the macroscopic work-hardening behavior exhibited by the material in stage B (blue curve) is mainly attributed to TRIP effect and dislocation slip (refer to Fig. 4).

Upon the onset of TRIP and within stage B, the γ -f.c.c. phase volume fraction decreased from 71 to 62 %, while the ϵ -h.c.p. increased by the corresponding amount. The lower stacking fault energy of the metastable $\text{Fe}_{42}\text{Mn}_{28}\text{Co}_{10}\text{Cr}_{15}\text{Si}_5$ HEA facilitates the occurrence of partial dislocations and phase transformation rather than conventional deformation by dislocation slip [14]. The onset for TRIP occurs slightly after yielding of γ -f.c.c. phase (281 vs 261 MPa, respectively). This suggests that an excess driving force (in the form of plastic deformation) is necessary for the metastability of the γ -f.c.c. to allow the formation of new ϵ -h.c.p. phase. This extra driving force also arises from the stacking

faults that are accumulated still during macroscopic plastic deformation (see Fig. 8).

The stacking faults probability, P_{sf} , shows a sudden increase (from 0.52 to 4.36 %) during stage B. The physical meaning of a stacking fault probability of 4.36 % implies the existence of 43.6 stacking faults among 1000 layers on average in the (111) planes [109]. This abrupt increase in the P_{sf} is related to the transformation from γ -f.c.c. to ϵ -h.c.p. which requires a significant increase in stacking faults, as these act as nucleation sites for the new ϵ -h.c.p. phase to form. The stacking faults that are continuously being generated provide an additional support for the continuous nucleation of ϵ -h.c.p. phase [81,110]. This suggests that the plastic deformation of the as-cast $\text{Fe}_{42}\text{Mn}_{28}\text{Co}_{10}\text{Cr}_{15}\text{Si}_5$ HEA during tensile deformation is mainly regulated by the Shockley partial dislocations, producing large amounts of stacking faults [63]. Compared to NiCoCr [111], FeCoNiCr [112] and $\text{Fe}_{20}\text{Co}_{30}\text{Ni}_{10}\text{Cr}_{20}\text{Mn}_{20}$ alloys [72], the metastable $\text{Fe}_{42}\text{Mn}_{28}\text{Co}_{10}\text{Cr}_{15}\text{Si}_5$ HEA under study has an increased stacking faults probability rate, which is attributed to its lower stacking fault energy [73]. In other words, the smaller the stacking fault energy, the greater the probability for stacking faults to form. Accordingly, the rate of decline of the stacking faults interspacing, L_{sf} , in stage B becomes relatively lower compared to stage A (refer to Fig. 8). Frank et al. [77] pointed out that this reduction in L_{sf} is related to the onset of the phase transition. The continued and significant decrease of L_{sf} in both stages A and B, contrasts with the sudden increase in the dislocation density of the γ -f.c.c. phase indicating that the smaller L_{sf} promotes dislocation accumulation in this phase, which ultimately contributes to an increase in the material strength.

From a crystallographic aspect, the γ -f.c.c. to ϵ -h.c.p. transformation is accomplished by Shockley partial shear $a/6 \langle 112 \rangle$ of every {111} lattice plane in the matrix γ -f.c.c. phase [84,113,114]. In other words, the stacking faults in the γ -f.c.c. phase are formed by the gliding of the Shockley partials of the $1/6 \langle 112 \rangle$ Burgers vector [176,177]. Evidently, the core of ϵ -h.c.p. formation is stacking faults, but this is controlled by the movement of the Shockley partial dislocations [115]. In this work, when the applied stress reaches 287 MPa (macroscopic yield point), the shear stress required for inducing partial dislocation motion is reached, triggering the TRIP. When the applied strain increases from 2.0 to 3.0 %, the phase transformation rate starts to decrease, which is related to the nucleation of tensile twins in the ϵ -h.c.p. grains which will then promote TWIP in stage C.

Although the γ -f.c.c. has already yielded and undergoes phase transformation in stage B, its phase volume fraction is still dominant (as shown in Fig. 5). As for the ϵ -h.c.p. phase, it starts to be plastically deformed in stage B. In fact, yielding of this phase occurs at the same stress level as the material yielding and above the yielding of the γ -f.c.c. phase (287 vs 261 MPa, respectively). Based on the volume fractions of the γ -f.c.c. and ϵ -h.c.p. phases at this stage, it is evident that the γ -f.c.c. phase continues to act as the soft phase regulating the plastic deformation of the material.

During stage B, the dislocation density of both phases is drastically modified. The dislocation density in the γ -f.c.c. phase increases significantly from 3.7×10^{14} to $1.61 \times 10^{15} \text{ m}^{-2}$, which is almost four times higher than the increase in dislocation density in the ϵ -h.c.p. phase from 4.9×10^{13} to $3.94 \times 10^{14} \text{ m}^{-2}$. Moreover, the variation in the dislocation density of the ϵ -h.c.p., which did not occur in stage A, further confirms that plastic deformation of this phase started to occur.

The sustained transformation of γ -f.c.c. to ϵ -h.c.p. requires large amounts of stacking faults, which makes the dislocation activity in the γ -f.c.c. phase to become even more important. As mentioned above, dislocations will encounter stacking faults, which are additional pinning sites to block dislocation motion. Meanwhile, the large number of phase boundaries created by the phase transformation further adds additional barriers to dislocation slip. This also justifies the increased accumulation of dislocations in the γ -f.c.c. phase.

Sinha et al. have proposed that the ϵ -h.c.p. phase dislocation density depends on this volume fraction and c/a ratio [79]. In our work, the

increase in the volume fraction of the ϵ -h.c.p. phase due to the phase transformation was shown in Fig. 5, and can be used to explain the increase in the ϵ -h.c.p. phase dislocation density in stage B. Considering that the pre-existing thermally induced ϵ -h.c.p. phase was not yet plastically deformed until a stress of 287 MPa is reached, the increase in ϵ -h.c.p. phase dislocation arises from both plastic deformation of the thermally induced ϵ -h.c.p. as well as that being formed due to the TRIP effect. In fact, there will be differences in the dislocation densities of the thermally stable and strain-induced ϵ -h.c.p. phase [116]. However, with synchrotron X-ray diffraction, it is only possible to get an overall quantification of the dislocation density in this phase without considering its nature (thermal vs strain-induced).

The predominant deformation mechanisms in stage B can be further elucidated based on the variation of the diffracted intensity of the selected ϵ -h.c.p. planes in both the TD and LD (refer to Fig. 10). Previously, it was shown that the ϵ -h.c.p. phase starts to be plastically deformed during stage B. However, no splitting on the diffracted intensity along LD and TD is expected, and this is shown in Fig. 10. Splitting of the diffracted intensity would mean that twinning was occurring. Thus, the fact that deformation twinning was not yet activated indicates that the ϵ -h.c.p. phase starts to be dominated by the basal $< a >$ slip, instead of the non-basal pyramidal $< c + a >$ slip, although the ϵ -h.c.p. c/a ratio is below the ideal value and shows signs of slow decrease. To be more specific, the material began to yield upon entering in stage B and a slow decrease in the c/a ratio from 1.624 to 1.621 occurs. In this stage, the ϵ -h.c.p. phase begins to deform plastically under a stress of 287 MPa. By default, the ϵ -h.c.p. c/a ratio should continue to follow the same trend of the previous stage, but as the γ -f.c.c. phase yields, the transformation to ϵ -h.c.p. phase is induced while plastic deformation of ϵ -h.c.p. phase also occurs. Therefore, a change in the c/a ratio starts to occur to accommodate the volume change variation resulting from the phase transformation, and lattice distortion induced by plastic deformation of both phases. However, as the phase fraction transformation is only of 9 % (see Fig. 5), there is only a minor decrease in the c/a ratio. Thus, combining the analysis of the intensity evolution in ϵ -h.c.p. phase during the deformation in stage B, it can be concluded that basal $< a >$ is the dominant slip mechanism.

In summary, during stage B two main deformation mechanisms are present: TRIP and dislocation slip. While the γ -f.c.c. phase experiences both dislocation slip and TRIP, the ϵ -h.c.p. phase only experiences basal $< a >$ slip.

4.2.3. Stage C – onset of tensile twinning

In stage B, with the onset of TRIP there was also the nucleation of twins. Stage C ($3.0\% < \epsilon < 7.7\%$) marks the onset of twinning in the ϵ -h.c.p. grains, while the γ -f.c.c. to ϵ -h.c.p. transformation is also occurring. Thus, the main deformation mechanisms at this stage are TRIP and TWIP, in addition to deformation slip, enabling for more plastic deformation of the material. In this region, the strain hardening rate curve exhibits a wave-like shape, which is attributed to the activation of tensile twinning and nucleation of compression twins, with the latter being a preceding step for the activation of a secondary twinning system. The valleys, which appear on the strain hardening rate curve, imply a reduction in the rate of incipient twin formation [58], as well as the nucleation of compression twins which will be described in section 4.2.4.

The stress partitioning evolution in stage C, where both phases have already undergone large plastic deformation, shows more marked differences than in stage B. The phase transformation rate from γ -f.c.c. to ϵ -h.c.p. is further accelerated in this stage (refer to Fig. 5), causing the stacking faults interspacing to further decrease with increasing stress (see Fig. 8). Moreover, the dislocation build-up necessary for the TRIP effect to be manifested also results in a persistent small-amplitude strain hardening in the γ -f.c.c. matrix phase. However, the deformation- and thermally-induced ϵ -h.c.p. phase carry almost 1.5 times more stress than the γ -f.c.c. phase, which is attributed to the load transfer to the harder

ϵ -h.c.p. and to the activation of tensile twinning.

The continued change in the volume fraction transformation from γ -f.c.c. to ϵ -h.c.p. proves that the TRIP deformation mechanism is still progressing. Moreover, the phase transformation rate continues to increase slightly compared to stage B. This is attributed to a combination of multiple deformation mechanisms: tensile twinning triggered in the ϵ -h.c.p. grains, phase transformation and dislocation slip. A stress of 407 MPa marks the trigger point for twinning and enables the TWIP deformation mechanism, as shown in Fig. 10.

Considering Fig. 10, it was observed that the normalized diffraction intensities of the three selected grain families of the ϵ -h.c.p. phase start to change dramatically over TD and LD. The evolution of the normalized diffraction intensity of the ϵ -h.c.p. ($10\bar{1}2$) oriented grains along TD and LD has a similar trend, however, there is a diametrically opposite evolution for the normalized diffraction intensity in both directions among the ($10\bar{1}3$) and ($10\bar{1}1$) orientated grains. Fu et al. [87] used neutron diffraction to evaluate TWIP in a $Fe_{50}Mn_{30}Co_{10}Cr_{10}$ HEA and noted that the splitting behavior of the diffracted intensities along TD and LD is evidence of the presence of deformation twinning, which is associated with significant lattice reorientation. Furthermore, the onset for this splitting marks the stress point at which deformation twinning is activated. Recently, Polatidis et al. [8] combined in-situ synchrotron X-ray diffraction with EBSD to demonstrate once again that the splitting behavior of the normalized diffraction intensity along both TD and LD is indeed caused by the presence of deformed twins in the ϵ -h.c.p. grains. Moreover, distinction between tensile and compression twinning can be evidenced by considering the evolution of the diffracted intensity along LD and TD for the ($10\bar{1}2$), ($10\bar{1}1$) and ($10\bar{1}3$) oriented grains. Considering Fig. 10, it can be observed that the abrupt splitting of the normalized diffraction intensity of the ($10\bar{1}3$) oriented grains over the TD and LD confirm onset of the ($10\bar{1}2$) tensile twinning.

It should be mentioned that, unlike deformation slip, twinning causes an abrupt reorientation of the crystal structure [117–121], and that two factors affect the deformation twinning modes: i) the critical resolved shear stress (CRSS), which refers to the tensile or compression component parallel to the c -axis of the deformed grain; ii) the Schmid factor, which describes the orientation of the grains with respect to the direction of the applied stress) [120]. Usually, tensile twinning in the ($10\bar{1}2$) grains occurs with a rotation of about 86.3° with respect to the “parent grain”, while the compression twinning in the ($10\bar{1}1$) grains has a rotation of around 56.2° [121]. The lower CRSS required for tensile twinning (between 2 and 2.8 MPa) [122], compared to the CRSS required for compression twinning (between 76 and 153 MPa) [123], is the main reason for the preferential and premature activation of ($10\bar{1}2$) tensile twinning. Although the CRSS between ($10\bar{1}1$) tensile twins and ($10\bar{1}2$) compression twins are significantly different, twin crystals with two different deformation modes can also occur in the same grain [124]. Therefore, to further assess the deformation twinning modes that are present in the three selected grain families, the normalized diffraction intensity trends in both TD and LD were used for further comparative analysis.

On closer inspection of the ϵ -h.c.p. ($10\bar{1}3$) oriented grains (refer to Fig. 10 e and f), the normalized diffraction intensity increases sharply along TD and only decreases slightly along LD, while the other oriented grain families do not change significantly in the TD direction. Considering that tensile twins are easily activated during tensile deformation due to the relatively low CRSS, it can be deduced that the increase in the normalized diffraction intensity of ($10\bar{1}3$) oriented grains along TD is caused by the lattice reorientation of the ($10\bar{1}2$) tensile twinning in the ($10\bar{1}3$) oriented “parent grain” reorientated by approximately 86.5° . The ($10\bar{1}2$) tensile twinning after lattice reorientation of 86.3° is now nearly parallel to the TD of the ($10\bar{1}3$) oriented “parent crystal” grains, revealing that the c -axis of the ϵ -h.c.p. ($10\bar{1}3$) oriented “parent crystal” grain is nearly parallel to LD. In other words, the ($10\bar{1}3$) oriented

"parent grain" has a higher Schmidt factor, favoring the activation of tensile twinning [125].

In contrast, the normalized diffracted intensity of the $(10\bar{1}1)$ oriented grains continues to increase along the LD, while in the TD the increase is significantly more reduced, suggesting that the twinned $(10\bar{1}3)$ oriented grains are most likely to become the LD of the $(10\bar{1}1)$ oriented grains. In other words, the ϵ -h.c.p. $(10\bar{1}3)$ oriented grains are in a $\approx 90^\circ$ azimuthal relationship with the ϵ -h.c.p. $(10\bar{1}1)$ oriented grains.

Deformation twinning is now an active deformation mechanism in stage C and occurs first on the ϵ -h.c.p. $(10\bar{1}3)$ oriented grains. This conclusion echoes that the non-basal pyramidal $< c+a >$ slip system is activated aided by the change in the c/a ratio. In addition, twinning formation is strongly influenced by the local stress state or strain distribution, and it can be inferred that the accumulation of a large number of dislocations in the ϵ -h.c.p. phase will act as stress concentrators, being this the main reason for the activation of twinning.

Compared to stage B, the lattice distortion increases in stage C (refer to Fig. 12). The lattice parameters in the ϵ -h.c.p. phase change significantly in this stage, with the lattice constant $a_{\epsilon\text{-h.c.p.}}$ expanding from 2.528 to 2.533 Å and the lattice constant $c_{\epsilon\text{-h.c.p.}}$ shrinking from 4.099 to 4.077 Å, resulting in a sharp decrease in the c/a ratio (from 1.621 to 1.609). At this stage, plastic deformation of the ϵ -h.c.p. phase is more predominant as a way for the material to accommodate more strain. Moreover, pyramidal $< c+a >$ slip gradually replaces the basal $< a >$ slip and starts to dominate the ϵ -h.c.p. phase slip mechanism, since the activity of pyramidal $< c+a >$ slip is strongly dependent on the ϵ -h.c.p. c/a ratio. The lower the ϵ -h.c.p. phase c/a ratio, the less favorable the basal $< a >$ slip is, thus facilitating the activation of the pyramidal $< c+a >$ slip [79]. In other words, at large deformations, the pyramidal $< c+a >$ slip has a higher Schmid factor, and is the deformation mode that can accommodate more strain along the c -axis [79].

The combined effect of pyramidal $< c+a >$ slip and deformation twinning are essential to accommodate the high c -axis strain and the associated work-hardening behavior of the ϵ -h.c.p. phase. Sinha et al. [79] have reported that the c/a ratio in HEAs undergoing phase transformation varies with processing and deformation, which is attributed to the dependence of the ϵ -h.c.p. phase lattice parameters on the microstructure and stress state due to transformation volume changes, which matches with the results derived in the present work. Moreover, from the evolution of the γ -f.c.c. and ϵ -h.c.p. volume fractions, shown in Fig. 5, it is clear that the faster phase transformation rate in stage C allows for the ϵ -h.c.p. phase to become predominant. Thus, it is evident that the change in c/a ratio is also a product by the phase transformation. Furthermore, unlike basal $< a >$ slip, the non-basal pyramidal $< c+a >$ slip system dominated the ϵ -h.c.p. phase slip mechanism which not only helps to achieve kinematically compatible deformation, while is the most efficient way to generate dislocation sources, resulting in major dislocation multiplication [62], which is consistent with the high dislocation density observed in stage C of Fig. 7 c).

The phase stress partitioning of Fig. 4 show that the ϵ -h.c.p. phase now bears more load than the γ -f.c.c. phase, while the higher deformation accommodated (refer to Fig. 7 e) occurs as a result of twinning deformation experienced by the ϵ -h.c.p. phase. It is evident that although the ϵ -h.c.p. phase is a "hard" phase structure, further promotion of strain accommodation can be achieved with the combined assistance of multiple deformation mechanisms such as deformation twinning and $< c+a >$ pyramidal slip as mentioned before. These multiple deformation mechanisms are also responsible for the ductility of the material, proving that the ϵ -h.c.p. phase mentioned above plays a crucial role in regulating of the plastic deformation of the metastable HEA after macroscopic yielding.

The combined existence of TRIP and TWIP in stage C promotes the increase of phase boundaries, providing a high-density source for dislocation accumulation, leading to a rapid increase in the dislocation

density. The dislocation density within the γ -f.c.c. phase evolved from 1.61×10^{15} to $3.15 \times 10^{15} \text{ m}^{-2}$, while for the ϵ -h.c.p. phase it grew from 3.94×10^{14} to $1.29 \times 10^{15} \text{ m}^{-2}$.

Compared to the low dislocation density contained in γ -f.c.c. grains in medium-Mn steels [126], which also experience TWIP, the high dislocation density in the γ -f.c.c. grains found in the metastable Fe₄₂Mn₂₈Co₁₀Cr₁₀Si₅ HEA under study plays a crucial role in enhancing its mechanical stability [41]. Dislocations can act as barriers for the sliding of the ϵ -h.c.p. phase interfaces, thus stabilizing the γ -f.c.c. grains [127]. Also, the larger amount of hard ϵ -h.c.p. induced by TRIP protects the γ -f.c.c. grains from experiencing excessive deformation [128], but still enabling the phase transformation to occur. Meanwhile, the high stress and elastic strain fields caused by the high dislocation density can effectively reduce the ϵ -h.c.p. phase nucleation barriers, and increase the necessary driving force for the phase transformation [103]. In other words, the high dislocation density can increase the transformation rate of γ -f.c.c. to ϵ -h.c.p., which is consistent with the high phase transformation rate of stage C detailed in Fig. 5. The twin boundaries introduced at this stage can also reduce the mean free motion path for dislocations and cause dislocation plugging, thus increasing the dislocation density of the ϵ -h.c.p. phase. This is in good agreement with the moderate increase in the dislocation density observed for the ϵ -h.c.p. phase.

To summarize the following deformation mechanisms are occurring in stage C: dislocation slip and TRIP for the γ -f.c.c. phase; tensile twinning and $< c+a >$ pyramidal slip for the ϵ -h.c.p. phase.

4.2.4. Stage D – onset of compression twinning

Finally, for true strains above 7.7 %, the material enters in stage D where the deformation mechanisms encompass a combination of TRIP, TWIP as well as dislocation slip, which results in an almost constant strain hardening rate. This is attributed to the widespread occurrence of nanoscale twins in the γ -f.c.c. grains and the formation of new boundaries induced by the TRIP and TWIP effects that limit the free travel of dislocations upon macroscopic loading [58].

A closer look at the stress-partition evolution detailed in Fig. 4, reveals that there is a tendency for the saturation of the strain hardening rate for both phases. For the ϵ -h.c.p. phase, the imparted stress is almost approaching that of the macroscopic stress behavior of the material due to the massive transformation of γ -f.c.c. to ϵ -h.c.p. and due to the multiple-twinning effects and dislocation interactions that primarily occur in this phase, indicating that the work hardening of ϵ -h.c.p. phase dominates the deformation behavior of the alloy studied in this work. For the γ -f.c.c. phase, the saturation in the strain hardening is caused by the formation of a large amounts of ϵ -h.c.p. phases through TRIP in the material, which generates new grain boundaries and thus limits the movement of dislocations within and to the γ -f.c.c. phase.

A slightly increase in the phase transformation rate at this stage compared to stage C, demonstrates the continuous occurrence of the TRIP effect, which started from the onset of macroscopic yielding and persists until material failure (refer to Fig. 5). Two reasons may justify the variation of the phase transformation rate at this stage. The first one is related to an activation effect due to the high dislocation density in the γ -f.c.c. phase (refer to Fig. 7 f) under large strains in this stage [115,129]. In stage D, the magnitude of the stacking faults interspacing, L_{sf} , is only 19.31 nm (refer to Fig. 8), with the smaller dislocation slipping path providing evidence for the high dislocation density accumulation. Moreover, the regions in the γ -f.c.c. phase with higher dislocation density (which can act as stress concentrators), when transformed to the ϵ -h.c.p. phase will promote stress relaxation, further activating more slip systems and allowing for more stress and strain to be imparted by the material. The second reason for this is related to the stress redistribution at the grain and phase boundaries. The phase transformation will initiate at the γ -f.c.c. phase grain boundaries, where dislocations tend to primarily pile up increasing the strain energy required for the phase transformation to occur. However, a relaxation effect on these high

stress concentration regions occurs upon TRIP [130]. This will reduce the stresses required for the phase transformation and have a retarding effect on the nucleation of the new ϵ -h.c.p. phase. The interaction between these two factors lead to an incomplete phase transformation prior to failure in the metastable γ -f.c.c. phase, ultimately resulting in 19 % of residual γ -f.c.c. phase.

Overall, the stress partitioning evolution from stage A to D, suggests that the metastable $\text{Fe}_{42}\text{Mn}_{28}\text{Co}_{10}\text{Cr}_{15}\text{Si}_5$ HEA can perform load redistribution during tensile loading through a series of different and competing deformation mechanisms. Moreover, the contributions of each deformation mechanism during macroscopic tensile loading varies and promotes a dynamic stress distribution behavior between both phases in the different deformation stages. Specifically, there is a large difference in the stress partitioning between the γ -f.c.c. and ϵ -h.c.p. phases, with the ϵ -h.c.p. phase bearing 1.2 to 1.5 times more stress than the γ -f.c.c. phase. Again, this value varies with the preferential deformation mechanism at different stages, but TRIP always plays a dominant role in the stress partitioning. Similar behavior to that has been shown in duplex stainless steels [131]. As revealed in [87,100], an essential feature of TRIP is the significant stress redistribution, demonstrating the importance of dynamic load distribution in the bulk hardening behavior [85]. Moreover, it contributes to improving the mechanical properties of the material.

In this stage, the dislocation densities of both γ -f.c.c. and ϵ -h.c.p. phases continues to increase until fracture. In fact, the rate of increase is similar to that of the stage C, which is in good agreement with the similar transformation rate of the γ -f.c.c. to ϵ -h.c.p. phase observed in both stages C and D. The dislocation density of the γ -f.c.c. phase increased from 3.15×10^{15} to $3.85 \times 10^{15} \text{ m}^{-2}$, while for the ϵ -h.c.p. phase it grew from 1.25×10^{15} to $1.49 \times 10^{15} \text{ m}^{-2}$. The increase in dislocation density in the γ -f.c.c. phase probably originates from the release of a large amount of dislocations from the moving ϵ -h.c.p. / γ -f.c.c. heterogeneous interface during the ongoing phase transformation [132]. It should be noted that the volume fraction of the ϵ -h.c.p. phase at this stage is already as high as 81 % (as shown in Fig. 5), and the softer γ -f.c.c. phase is constrained by the surrounding harder ϵ -h.c.p. phase, which can lead to long-range back stress [103,133]. This back stress can prevent/difficult the dislocation source from emitting more dislocations.

The amount of new ϵ -h.c.p. phase formed by phase transformation is to some extent related to stacking faults probability, P_{sf} , and stacking faults interspacing, L_{sf} , since the new ϵ -h.c.p. phase nucleates at sites in γ -f.c.c. phase with a large density of stacking faults. In addition to this, the evolution of the dislocation density in the γ -f.c.c. phase is related to the plastic deformation but also to the formation and accumulation of stacking faults in the γ -f.c.c. phase, as these act as barriers against the movement of the dislocations, resulting in a reduction of the average free path of the dislocation movement and consequently causing the plugging of dislocations.

Regarding the evolution of the stacking faults probability, P_{sf} , and stacking faults interspacing, L_{sf} , in stage D, the P_{sf} is increasing at an approximately constant state with increasing deformation, suggesting that if the material has a sufficiently low stacking faults energy, thus significant accumulation of stacking faults can occur even at room temperature and low strain rates, as in the case of the current work. Upon fracture, the P_{sf} reaches ≈ 10.7 %, which is significantly higher than that measured for a CrMnFeCoNi HEA (≈ 1.5 %) [134], indicating that the lower the stacking faults energy, the higher the corresponding P_{sf} . It is important to mention here that, the the P_{sf} is generally correlated with the amount of ϵ -h.c.p. phase, as this phase is formed by the ordering of dense stacking faults. The increase of the P_{sf} in the γ -f.c.c. phase means that more stacking faults are being formed and accumulated in this phase. These stacking faults act as nucleation sites for the transformation from γ -f.c.c. phase to ϵ -h.c.p. phase. Thus, the evolution of the P_{sf} is directly linked with the phase transformation kinetics upon loading. This is evident when comparing the steady increasing trend of the γ -f.c.c. to ϵ -h.c.p. transformation in both stage C and D (refer to

Fig. 5) and a similar trend in the evolution of the P_{sf} (refer to Fig. 8). From stage C onwards, the reduction in L_{sf} is further slowed until it enters stage D, where the change in L_{sf} is found to reach a saturation plateau, at approximately 19 nm. A similar saturation response is observed in numerous alloys such as hot-rolled Co-Cr-Mo alloy, Mg alloy [63,78] as well as in $\text{Fe}_{40}\text{Mn}_{20}\text{Cr}_{15}\text{Co}_{20}\text{Si}_5$ HEAs [77]. The reduction of the L_{sf} during plastic deformation not only promotes an increase in the dislocation density, but also strengthens the material as evidenced in both a Mg alloys [78] and a $\text{Fe}_{40}\text{Mn}_{20}\text{Cr}_{15}\text{Co}_{20}\text{Si}_5$ HEAs [77].

Alongside with TRIP, multiple twinning modes (tensile and compression twinning modes) are now fully activated. Severe lattice reorientation leads to a dramatic change in the normalized diffracted intensity, as evidenced by the clear splitting behavior diffracted data in Fig. 10 a) and b). The normalized intensity of ϵ -h.c.p. (10 $\bar{1}$ 1) oriented grains decreases along the TD and increases sharply along the LD, while the normalized intensity of ϵ -h.c.p. (10 $\bar{1}$ 2) and (10 $\bar{1}$ 3) oriented grains exhibits an opposite evolution, showing an opposite evolutionary trend along TD and LD. Fu et al. have reported that a similar normalized diffraction intensity splitting behavior was observed in a TRIP $\text{Fe}_{50}\text{Mn}_{30}\text{Co}_{10}\text{Cr}_{10}$ HEA when it was subjected to large tensile plastic deformation, and attributed this to the activation of compression twinning and multiple-twin systems [87]. As can be seen from stage C in Fig. 10 a) and b), the c-axis of ϵ -h.c.p. (10 $\bar{1}$ 1) oriented grains are perpendicular to the loading axis (LD) and therefore the c-axis is compressed, which means that the ϵ -h.c.p. (10 $\bar{1}$ 1) oriented grains are favorable to the formation of compression twins. The source of the CRSS required for compression twinning formation arises the high local stress concentration resulting from the saturation of both the phase transformation (as shown in Fig. 4) as well as the high dislocation density (as shown in Fig. 7 f)). The formation of compression twins in the ϵ -h.c.p. (10 $\bar{1}$ 1) oriented grains allow for an $\approx 56.2^\circ$ lattice reorientation, which is consistent with previous findings [19,87]. Frank et al [19] pointed out that the compression twinning of ϵ -h.c.p. (10 $\bar{1}$ 1) grains can also be predicted by a decrease in the normalized diffraction intensity along TD and an increase along LD. The increase in the diffraction intensity of the ϵ -h.c.p. (10 $\bar{1}$ 2) oriented grains along the LD is the result of dislocation slipping [87]. The rarely reported ϵ -h.c.p. (10 $\bar{1}$ 3), on the other hand, is regarded as evidence of compression twinning action, and the orientation deviations were confirmed by Fu et al. [87] using EBSD.

The lattice parameters of the ϵ -h.c.p. phase, $a_{\epsilon\text{-h.c.p.}}$ and $c_{\epsilon\text{-h.c.p.}}$, reach to practically constant values in stage D (as shown in Fig. 12 a)), which results in a saturation behavior of the c/a ratio. Nonetheless, the main slip mechanism of the ϵ -h.c.p. phase is still dominated by non-basal pyramidal $< c + a >$ slip system, while basal slip is almost suppressed. To accommodate the higher macroscopic tensile strain, both tensile and compression twins are active at this stage (see Fig. 10). The saturation behavior seen in the c/a ratio stems from the high ϵ -h.c.p. phase volume fraction (≈ 81 % in stage D), causing the soft γ -f.c.c. phase to be surrounded by the hard ϵ -h.c.p. phase, which can make the plastic deformation of the γ -f.c.c. phase and the TRIP effect difficult at this stage. In conclusion, when designing structural materials based on ϵ -h.c.p. phase structures, tuning of the c/a ratio should be performed so that the $< c + a >$ slip system is preferentially activated. This can render the development of alloys with excellent strength/ductility balance.

From the comprehensive discussion presented from section 4.2.1 to section 4.2.4, the main deformation mechanisms experienced by the metastable $\text{Fe}_{42}\text{Mn}_{28}\text{Co}_{10}\text{Cr}_{15}\text{Si}_5$ HEA were detailed. These are schematically represented in Fig. 14 and are summarized as follows: stage A experiences dislocation slip in the γ -f.c.c. phase; stage B possesses dislocation slip and TRIP of the γ -f.c.c., while basal $< a >$ slip occurs on the ϵ -h.c.p. phase; stage C is characterized by dislocation slip and TRIP of γ -f.c.c. phase, with the onset of tensile twinning and non-basal pyramidal $< c + a >$ slip in the ϵ -h.c.p. phase; finally in stage D, to same deformation mechanisms observed in stage C there is the addition of compression twinning in the ϵ -h.c.p. phase.

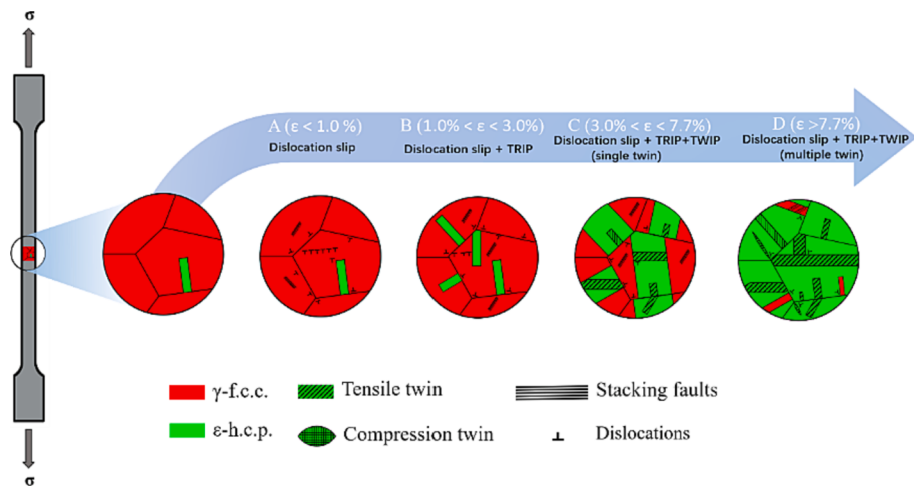


Fig. 14. Schematic diagram of the deformation mechanisms in the as-cast $\text{Fe}_{42}\text{Mn}_{28}\text{Co}_{10}\text{Cr}_{15}\text{Si}_{5}$ metastable HEA during tensile loading.

The schematic of lattice reorientation during tensile and compression twinning is shown in Fig. 15 and can be used to support the previous discussion on the onset of these twinning modes and their identification for the diffracted data of specific ϵ -h.c.p. phase planes. Fig. 15 a) shows a $(10\bar{1}3)$ oriented grain with its c-axis parallel to the LD, which facilitates

the formation of tensile twins by lattice reorientation 86.3° of the “parent grain” $(10\bar{1}3)$. $(10\bar{1}3)$ oriented grains are transformed into $(10\bar{1}1)$ oriented grains after the $(10\bar{1}2)$ tensile twinning occurs. In other words, $(10\bar{1}3)$ oriented grains have high probability to become the

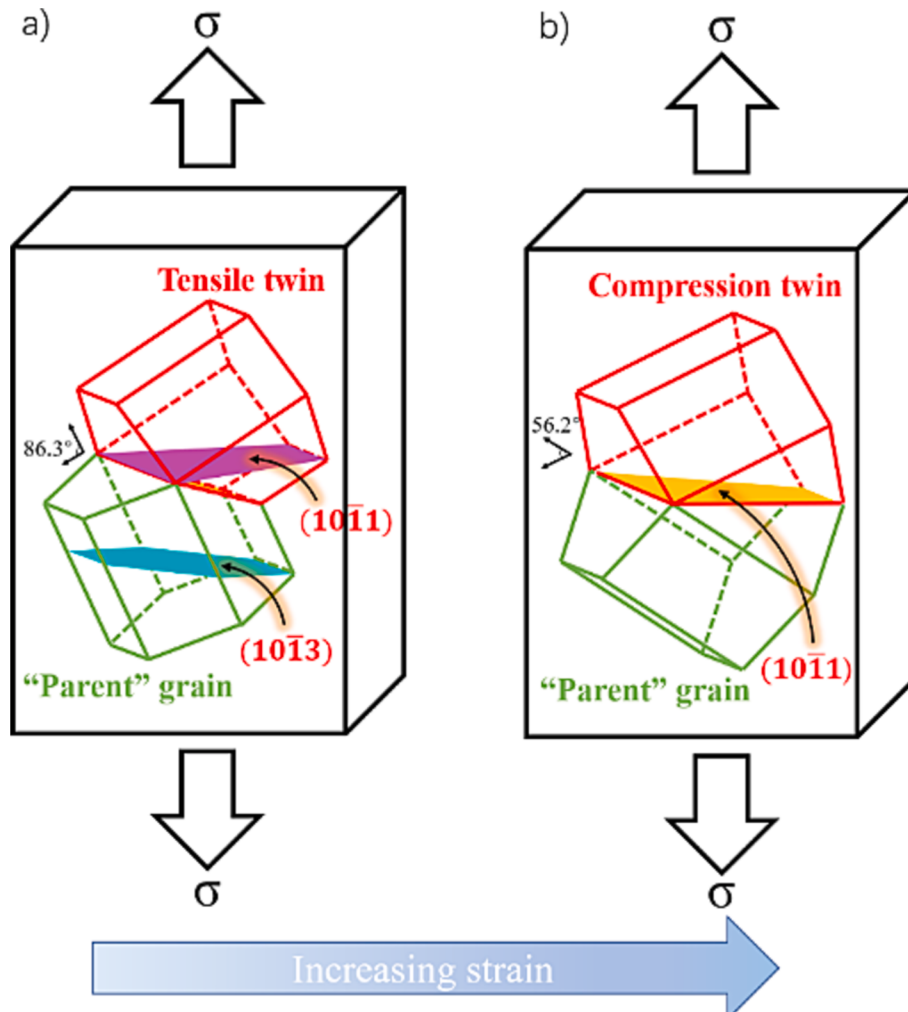


Fig. 15. Schematic representation of the lattice reorientation occurring with increasing strain. a) 86.3° reorientation of the tensile twin relative to the parent $(10\bar{1}3)$ oriented grain; b) 56.2° reorientation of the compression twin relative to the parent $(10\bar{1}1)$ oriented grain.

($10\bar{1}1$) oriented grain after tensile twinning occurs. The ($10\bar{1}1$) oriented grains are prone to compressive twinning because their c-axis is close to TD, and their lattice reorientation schematic is shown in Fig. 15 b), where these compression twins are formed by a 57.2° lattice reorientation of the ($10\bar{1}1$) parent grain.

4.2.5. Comparison between *in-situ* synchrotron X-ray diffraction and EBSD data

The evolution of the phase volume fraction obtained from *in-situ* EBSD experiments (refer to Fig. 6) provides valuable insights into the microstructure changes imposed by the external tensile deformation. Overall, as the strain increases, there is a gradual increase of the lath-like hexagonal close-packed (ϵ -h.c.p.) phase, observed within the metastable face-centered cubic (γ -f.c.c.) matrix, resulting from the TRIP effect. The volume fraction of the γ -f.c.c. phase decreases from $\approx 67.2\%$ (prior to loading) to about $\approx 33.8\%$ (in the fracture region), suggesting that a significant transformation from γ -f.c.c. to ϵ -h.c.p. occurs during the plastic deformation process, which aids the continuous deformation and strengthening of the material.

Considering the evolution of γ -f.c.c. and ϵ -h.c.p. volume fractions during the tensile loading, initially, at $\epsilon = 0\%$ (stage A), these correspond to $\approx 67.2\%$ and $\approx 32.8\%$, respectively. These initial values are in good agreement with the Rietveld refinement calculations obtained from the high energy synchrotron X-ray diffraction data (γ -f.c.c. phase: $\approx 67.2\%$ vs. $\approx 71.1\%$; ϵ -h.c.p. phase: $\approx 32.8\%$ vs. $\approx 28.9\%$). As the strain increases to 1% (stage B), a slight increase in the volume fraction to ϵ -h.c.p. phase, at expense of γ -f.c.c. phase, is observed. This strain determines the onset of the TRIP, as corroborated by the *in-situ* X-ray diffraction data.

As the strain increases further, from $\epsilon = 3$ to 7% (stage C), the volume fraction of the γ -f.c.c. phase declines from $\approx 58.3\%$ to $\approx 48.6\%$. In parallel, synchrotron calculations show a corresponding reduction in the γ -f.c.c. phase volume fraction from $\approx 61.9\%$ to about $\approx 47.9\%$. Upon entering stage D, corresponding to the significant plastic deformation, at $\epsilon = 9\%$, a remarkable consistency is observed in γ -f.c.c. \rightarrow ϵ -h.c.p. phase transformation (γ -f.c.c. phase: $\approx 34.9\%$ vs $\approx 34.4\%$, ϵ -h.c.p. phase: $\approx 65.05\%$ vs $\approx 65.6\%$). However, at the final fracture state ($\epsilon = 11\%$), a slight deviation between *in-situ* EBSD experimental results and synchrotron calculations is noticed for the γ -f.c.c. phase ($\approx 19\%$ vs. $\approx 33.8\%$). This discrepancy primarily stems from the differing operational modes of high-energy synchrotron X-ray diffraction and EBSD. High-energy synchrotron X-rays operates in a transmission mode, enabling the acquisition of bulk-averaged information over the sample thickness for volumetric evaluation. Conversely, EBSD functions in a reflection mode, is influenced by surface effects, and is limited to capturing information from the vicinity of the sample's surface. Therefore, at the fracture surface, there is a difference in the phase volume fraction derived from the two characterization methods.

In conclusion, the evolution of ϵ -h.c.p. and γ -f.c.c. phase fractions obtained through *in-situ* EBSD during tensile testing correlates well with the trends inferred from the synchrotron X-ray diffraction data using Rietveld refinement. The EBSD-derived volume fraction of the ϵ -h.c.p. phase are consistently slightly lower than those obtained from the synchrotron calculations. This discrepancy mainly stems from different factor including: i) different working modes: bulk transformation mode (synchrotron X-ray diffraction) vs surface reflection mode (EBSD); ii) the relatively lower resolution and magnification of the current EBSD scans, coupled with limitations in identifying all the fine ϵ -h.c.p. martensite laths-like construction within the scanned region. Nonetheless, it is shown that both approaches can be confidently used to determine, within a given error margin, the actual phase fractions at any given deformation condition.

The mechanically induced martensitic phase transformation from γ -f.c.c. to ϵ -h.c.p. leads to an increase in dislocation density. This can be inferred from the average Kernel Average Misorientation (KAM) data

where, the average value rises from $\approx 0.95^\circ$ in the as-received condition to $\approx 2.99^\circ$ at the fracture point (refer to Fig. 9).

An important observation is that with the increase in strain, a significant portion of the strain becomes localized at grain boundaries, where the strain amplification is notably higher than within the grain interiors. This behavior is attributed to the fact that the γ -f.c.c. matrix, being the softer phase, experiences a more pronounced plastic deformation. Consequently, this leads to the development of localized strain gradients near the interfaces between the soft γ -f.c.c. matrix and the hard ϵ -h.c.p. phase.

Additionally, as expected, both the γ -f.c.c. and ϵ -h.c.p. phases exhibit an increasing trend in GND values during the tensile process. This trend qualitatively reveals that as deformation progresses, the dislocation density within these two matrix phases also increases. This variation aligns consistently with the results obtained from the dislocation density calculations using synchrotron X-ray diffraction (refer to Fig. 7). Finally, upon comparing the average GND values within the same region of the γ -f.c.c. and ϵ -h.c.p. phases, a consistent observation emerges: across all strain levels, the average GND value in the γ -f.c.c. phase consistently surpasses that in the ϵ -h.c.p. phase. This observation indicates that under identical loading conditions, the softer γ -f.c.c. phase experiences a higher dislocation density compared to the harder ϵ -h.c.p. phase. This distinction arises due to the divergent mechanical responses of the dual-phase γ -f.c.c. and ϵ -h.c.p. structures during the loading process.

4.3. Lattice strain evolution

The lattice strain evolution is not only able to show the amount of deformation imparted by each phase but, more importantly, is able to reflect the load transfer among different grain families. The lattice strain evolution in the $\text{Fe}_{42}\text{Mn}_{28}\text{Co}_{10}\text{Cr}_{15}\text{Si}_5$ metastable HEA which previously shown in Fig. 11 is analyzed next.

During the macroscopic elastic deformation (stage A), the lattice strain of each lattice plane of both γ -f.c.c. and ϵ -h.c.p. phases increases almost linearly with the applied stress. However, the slope of this variation, which is related to the plane stiffness, varies between different crystallographic orientations, revealing anisotropy in the mechanical response. Softer lattice planes will first bear the applied stress until their yielding occurs, upon which load transfer to harder planes takes place. This load transfer and partitioning behaviors ensures the uniform plastic deformation of the material. The Young's modulus of the analyzed γ -f.c.c. and ϵ -h.c.p. phases along the LD were determined by linear fitting in the macroscopic elastic deformation region. For the γ -f.c.c. it follows that $E_{\gamma-\text{f.c.c.}(111)} > E_{\gamma-\text{f.c.c.}(311)} > E_{\gamma-\text{f.c.c.}(200)}$, which reveals that the γ -f.c.c. (111) plane is the hardest, while the (200) plane is the softest. These results are consistent with the soft and hard responses exhibited by the f.c.c. lattice planes observed in some single-phase [134,135] and dual-phase HEAs [19,39,136]. For the ϵ -h.c.p. phase structure, $E_{\epsilon-\text{h.c.p.}(10\bar{1}3)} > E_{\epsilon-\text{h.c.p.}(10\bar{1}2)} > E_{\epsilon-\text{h.c.p.}(10\bar{1}1)}$. For reference, the Young's modulus for the analyzed crystallographic planes obtained along LD are summarized in Table 3. It should be mentioned here that the lattice strains in the γ -f.c.c. and ϵ -h.c.p. lattice planes are both positive in the LD and, conversely, negative in the TD, this behavior being expected due the Poisson's effect.

When entering stage B, where macroscopic plastic deformation of the material starts to occur all analyzed planes exhibit a deviation to the

Table 3

Elastic modulus for different lattice planes of constituent phases in as-cast $\text{Fe}_{42}\text{Mn}_{28}\text{Co}_{10}\text{Cr}_{15}\text{Si}_5$ metastable HEA.

| γ -f.c.c. plane (GPa) | | | ϵ -h.c.p. plane (GPa) | | | |
|------------------------------|---------------|---------------|--------------------------------|--------------------|--------------------|--------------------|
| $E_{(111)}$ | $E_{(200)}$ | $E_{(311)}$ | $E_{(10\bar{1}0)}$ | $E_{(10\bar{1}1)}$ | $E_{(10\bar{1}2)}$ | $E_{(10\bar{1}3)}$ |
| 182 ± 1.9 | 108 ± 1.7 | 158 ± 1.8 | 117 ± 1.1 | 149 ± 1.3 | 191 ± 8.1 | 247 ± 0.4 |

previous linear response suggesting their yielding. However, the associated lattice strain is dependent on the crystal orientation vs loading direction relationship [137]. For example, in stage B the developed lattice strain is higher for the softest plane, and lower for the stiffer one. The same behavior is noticed for the ϵ -h.c.p. phase. The four different lattice planes ($10\bar{1}0$), ($10\bar{1}\bar{1}$), ($10\bar{1}2$) and ($10\bar{1}3$) of ϵ -h.c.p. phase, which are dominated by the basal $<\mathbf{a}>$ slip in stage B, all have a tendency for increasing the imparted lattice strain along LD, but with different magnitudes (1342, 1663, 1933 and 1478 $\mu\epsilon$, respectively). The trend in the evolution of lattice strain also highlights that the ϵ -h.c.p. phase starts to bear more stresses, due to the premature yielding and soft nature of the γ -f.c.c., thus promoting a stress relaxation effect in this phase [87]. However, it should be emphasized that this stress relaxation arises from both the load partitioning to the ϵ -h.c.p. phase but also due to the TRIP effect.

When entering stage C, the lattice strain developed in the ϵ -h.c.p. is significantly reduced in magnitude when compared to stage B. This is related to a saturation of the work-hardening behavior of the different lattice planes resulting from the massive plastic deformation imparted by the material. This effect is further exacerbated in stage D, where the increase in lattice strain as function of stress or strain is almost negligible. The saturation is occurring in both phases and is primarily related to the high dislocation density (refer to Fig. 7 f)).

4.4. Strengthening contributions

Dislocation slip has always been of interest as a common deformation mechanism for γ -f.c.c. and ϵ -h.c.p. phases, while TRIP is another an additional deformation mechanism in the γ -f.c.c. phase. However, studies on the stacking faults strengthening effect in HEAs are scarce. A comprehensive analysis of the different dislocation strengthening contributions of both phases, as well as the stacking faults strengthening contribution in the γ -f.c.c. phase was shown in Fig. 8.

In the macroscopic elastic deformation stage of A ($\epsilon < 1\%$), which is dominated by dislocation slip of the γ -f.c.c., the intrinsic dislocation strengthening contribution from the ϵ -h.c.p. phase due to dislocation is approximately 5 MPa, which contrasts with the 104 MPa (with further increase up to 215 MPa in stage A) of the γ -f.c.c. phase. This significant difference is rooted to the distribution of dislocation density in both phases (see Fig. 7 f)). Throughout stage A, the stacking faults strengthening contribution from the γ -f.c.c. phase increase is only of 5 MPa.

In the plastic deformation stage B ($1\% < \epsilon < 3\%$), where the deformation mechanism is dominated by TRIP and dislocation slip, the dislocation strengthening contributions of the γ -f.c.c. and ϵ -h.c.p. phase increase from 215 to 233 MPa and from 14 MPa to 58 MPa, respectively. Based on the magnitude of the strengthening contribution, the dislocation strengthening contribution in the γ -f.c.c. phase is almost four times larger than that in the ϵ -h.c.p. phase. This is related to the dislocation density contained in both phases ($\rho_{\gamma\text{-f.c.c. phase}} \approx 1.61 \times 10^{15} \text{ m}^{-2}$ and $\rho_{\epsilon\text{-h.c.p. phase}} \approx 3.94 \times 10^{14} \text{ m}^{-2}$, as shown in Fig. 7 f)). Regarding the contribution of the stacking faults in the γ -f.c.c. phase to the material flow stress, it increases from 5 MPa to 48 MPa, which is near a 10-fold increase compared to stage A. In fact, this is directly related to the amount of stacking faults accumulated (refer to Fig. 8). Specifically, it can be seen from Equation (27) that there are two main factors affecting the strengthening due to stacking faults, one being the strengthening factor, K_{sf} , which is a constant, and the other being the stacking faults interspacing L_{sf} , which evolves under tensile deformation as shown in Fig. 8. Therefore, the dynamic evolution of the stacking faults contribution is only dependent on the L_{sf} . Thus, the evolution of the stacking faults strengthening contribution during this stage coincides well with the variation of L_{sf} depicted Fig. 8. In addition to this, Frank et al. [138] have reported that stacking faults strengthening is associated with the γ -f.c.c. to ϵ -h.c.p. phase transformation as well as to the work-hardening behavior, and that an increase in the stacking faults strengthening

contribution corresponds to the onset of the phase transformation, which is again in good agreement with the results of the current study. In this work, the γ -f.c.c. to ϵ -h.c.p. phase transformation is triggered at 284 MPa, which corresponds to the point where there is a sudden increase in the stacking fault probability (refer to Fig. 8).

During stage C ($3 < \epsilon < 7.7\%$) where the deformation mechanism comprised TRIP, TWIP and dislocation slip, the dislocation strengthening contribution from γ -f.c.c. phase grows gradually from 233 to 304 MPa and from 58 to 105 MPa for the ϵ -h.c.p. phase. From Fig. 13, it is observed that the dislocation strengthening contributions in both γ -f.c.c. and ϵ -h.c.p. phase show a continuous increasing trend and the incremental rate is larger than in stages A and B. However, in stage C, the contribution of the dislocation strengthening from the γ -f.c.c. phase is only two times larger than that arising from the ϵ -h.c.p. phase. This was expected, since the transformation from γ -f.c.c. to ϵ -h.c.p. promotes the appearance of ϵ -h.c.p. with higher dislocation density than the thermally-induced one. The large transformation rate (shown in Fig. 5) at this stage also further contributes to the strengthening by stacking faults in the γ -f.c.c. phase from 48 to 102 MPa.

Finally, when entering stage D ($\epsilon > 7.7\%$), it can be found that the evolution of the dislocation strengthening contribution from both γ -f.c.c. and ϵ -h.c.p. phases, as well as the stacking faults strengthening contribution from γ -f.c.c. phase, are approaching a saturated state and remain almost constant. This stems from the saturation of dislocation density and stacking faults interspacing, L_{sf} , as detailed in Fig. 7 c) and Fig. 8. The maximum strengthening contribution arising from dislocations in both the γ -f.c.c. and ϵ -h.c.p. phases reaches 321 and 111 MPa, respectively, while the stacking faults strengthening further contributed to 118 MPa to the material strength. Overall, it is shown that the dislocation strengthening contribution is the main source of the high strength of the present metastable HEA.

In summary, it is shown that there are two major sources of contribution to the flow stress in the as-cast $\text{Fe}_{42}\text{Mn}_{28}\text{Co}_{10}\text{Cr}_{15}\text{Si}_5$ HEA studied in this work. One is dislocation-dislocation interactions, where the dislocation strengthening contribution from the γ -f.c.c. phase is significantly higher than that in the ϵ -h.c.p. phase. The reason for this is the reduction in the average free path for dislocation movement resulting from the large amount of stacking faults and decrease in the stacking faults interspacing in the γ -f.c.c. phase, which greatly contributes to the dislocation hardening effect. The other source is the stacking faults strengthening in the γ -f.c.c. phase, which is necessary for the phase transformation to occur, as stacking faults are the preferential sites for the ϵ -h.c.p. phase nucleation. However, its strengthening effect is significantly lower than that caused by dislocations. It should be mentioned that this is the first time that a quantitative analysis of the evolution of the strengthening contributions of a metastable HEA of the Fe-Mn-Co-Cr system is performed using high energy synchrotron X-ray diffraction. This provides a comprehensive understanding of how the microstructure evolution experienced by the alloy modifies the predominant deformation mechanisms and how these contribute to the strength and ductility of the material, which can be useful to overcome the traditional strength-ductility paradigm with implications for the design of advanced structural alloys.

The strengthening mechanisms experienced by the metastable HEA during tensile loading are schematically shown in Fig. 16, where a) refers to the dislocation strengthening in the γ -f.c.c. phase, $\sigma_{\gamma\text{-f.c.c. DIS}}$; b) details the stacking faults strengthening in the γ -f.c.c. phase, $\sigma_{\gamma\text{-f.c.c. SF}}$; while c) points to dislocation strengthening in the ϵ -h.c.p. phase, $\sigma_{\epsilon\text{-h.c.p. DIS}}$. The core of these strengthening mechanisms is the reduction of the mean free path for dislocations, Λ , causing dislocation pile up.

5. Conclusions

In this paper, the deformation mechanisms and micromechanical behavior of an as-cast $\text{Fe}_{42}\text{Mn}_{28}\text{Co}_{10}\text{Cr}_{15}\text{Si}_5$ metastable HEA was investigated by in-situ synchrotron X-ray diffraction and in-situ EBSD

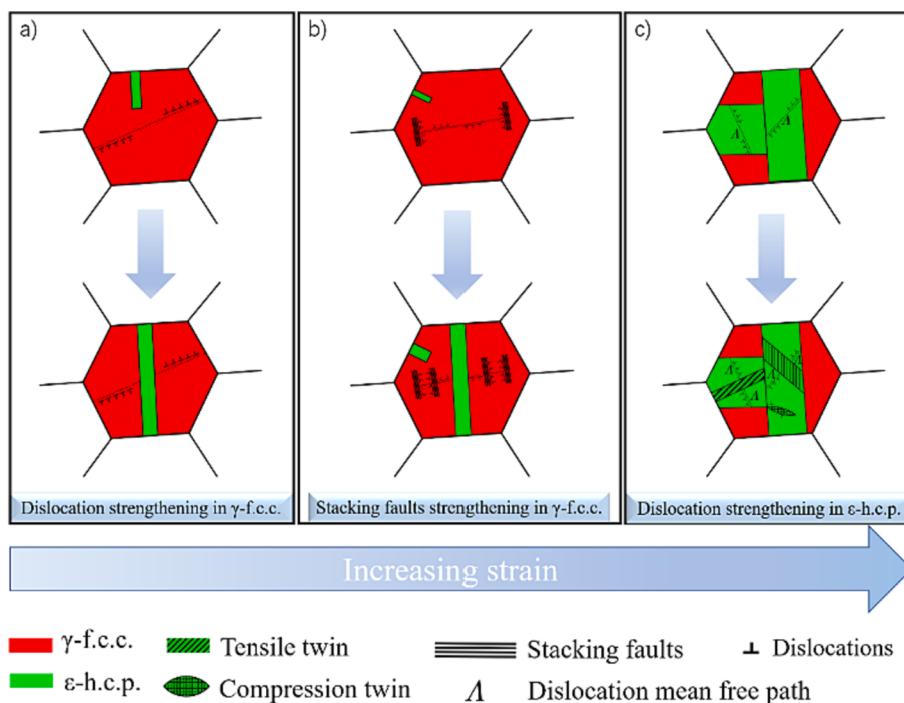


Fig. 16. Schematic representation of the strengthening mechanisms in the as-cast $\text{Fe}_{42}\text{Mn}_{28}\text{Co}_{10}\text{Cr}_{15}\text{Si}_5$ metastable HEA upon tensile loading.

experiments. The microstructure evolution was qualitatively and quantitatively assessed, based on multiple features including phase volume fraction, c/a ratio and lattice strain. Stress partitioning and redistribution between the γ -f.c.c. and ϵ -h.c.p. phases was seen to be linked to the active deformation mechanisms of the alloy at a given loading step.

Yielding of the soft γ -f.c.c. phase was seen to occur prior to yielding of the hard ϵ -h.c.p., with the latter occurring in parallel to macroscopic yielding. Upon entering the plastic deformation region, the hard ϵ -h.c.p. phase bears significantly more stress than the γ -f.c.c. phase. The onset of TRIP occurred slightly after plastic deformation of the γ -f.c.c. phase suggesting the need for an excess driving force for the transformation to occur. This excessive driving force was in the form of stacking faults accumulation. TWIP occurred at larger stresses levels compared to TRIP (407 vs 287 MPa, respectively). Tensile twinning was first activated due to the lower critical resolved shear stress, and prior to material failure compression twinning was evidenced.

The four identified deformation regimes were characterized by different actuating deformation mechanisms: stage A had dislocation slip occurring in the γ -f.c.c. phase; stage B had dislocation slip and TRIP on the γ -f.c.c. and basal $< a >$ dislocation slip on the ϵ -h.c.p.; stage C had the same deformation mechanisms for the γ -f.c.c., but non-basal $< c + a >$ dislocation slip and tensile twinning were activated on the ϵ -h.c.p. phase; finally, in stage D there was the addition of compression twinning to the ϵ -h.c.p. phase, while the other mechanisms were kept active.

The strengthening contributions were also quantified. It was determined that the dislocation strengthening from the γ -f.c.c. phase was larger than that induced by dislocations in the ϵ -h.c.p. phase. Moreover, the magnitude of the strengthening contribution due to stacking faults in the γ -f.c.c. phase was similar to that arising from dislocations in the ϵ -h.c.p. phase. The results presented in this work are of interest for designing dual-phase alloys with good strength/ductility balance.

CRediT authorship contribution statement

Jiajia Shen: Data curation, Formal analysis, Investigation, Methodology, Writing – original draft. **Wei Zhang:** Investigation. **J.G. Lopes:** Investigation. **Yutao Pei:** Investigation. **Zhi Zeng:** Investigation. **E.**

Maawad: Investigation. **N. Schell:** Investigation. **Ana C. Baptista:** Investigation. **Rajiv S. Mishra:** Formal analysis, Investigation, Writing – review & editing. **J.P. Oliveira:** Supervision, Formal analysis, Investigation, Writing – review & editing.

Declaration of competing interest

The authors declare that they have no known competing financial interests or personal relationships that could have appeared to influence the work reported in this paper.

Data availability

Data will be made available on request.

Acknowledgements

JS, JGL and JPO acknowledge Fundação para a Ciência e a Tecnologia (FCT - MCTES) for its financial support via the project UID/00667/2020 (UNIDEMI). JS and JPO acknowledge funding by national funds from FCT - Fundação para a Ciência e a Tecnologia, I.P., in the scope of the projects LA/P/0037/2020, UIDP/50025/2020 and UIDB/50025/2020 of the Associate Laboratory Institute of Nanostructures, Nanomodelling and Nanofabrication – i3N. JS acknowledges the China Scholarship Council for funding the Ph.D. grant (CSC NO. 201808320394). JGL acknowledges Fundação para a Ciência e a Tecnologia (FCT-MCTES) for funding the Ph.D. Grant 2020.07350.BD. ZZ acknowledges Science and Technology Project of Sichuan Province (2020ZDZX0015). The authors acknowledge DESY (Hamburg, Germany), a member of the Helmholtz Association HGF, for the provision of experimental facilities. Beamtime was allocated for proposal I-20210899 EC. The research leading to this result has been supported by the project CALIPSOplus under the Grant Agreement 730872 from the EU Framework Programme for Research and Innovation HORIZON 2020.

References

- [1] J.-W. Yeh, S.-K. Chen, S.-J. Lin, J.-Y. Gan, T.-S. Chin, T.-T. Shun, C.-H. Tsau, S.-Y. Chang, Nanostructured High-Entropy Alloys with Multiple Principal Elements: Novel Alloy Design Concepts and Outcomes, *Adv. Eng. Mater.* 6 (2004) 299–303, <https://doi.org/10.1002/adem.200300567>.
- [2] B. Cantor, I.T.H. Chang, P. Knight, A.J.B. Vincent, Microstructural development in equiaxed multicomponent alloys, *Mater. Sci. Eng. A* 375–377 (2004) 213–218, <https://doi.org/10.1016/j.msea.2003.10.257>.
- [3] O.N. Senkov, G.B. Wilks, J.M. Scott, D.B. Miracle, Mechanical properties of Nb25Mo25Ta25W25 and V20Nb20Mo20Ta20W20 refractory high entropy alloys, *Intermetallics* 19 (2011) 698–706, <https://doi.org/10.1016/j.intermet.2011.01.004>.
- [4] S.S. Nene, M. Frank, P. Agrawal, S. Sinha, K. Liu, S. Shukla, R.S. Mishra, B. A. McWilliams, K.C. Cho, Microstructurally flexible high entropy alloys: Linkages between alloy design and deformation behavior, *Mater. Des.* 194 (2020) 108968, <https://doi.org/10.1016/j.matdes.2020.108968>.
- [5] X. Gao, Y. Lu, J. Liu, J. Wang, T. Wang, Y. Zhao, Extraordinary ductility and strain hardening of Cr26Mn20Fe20Co20Ni14 TWIP high-entropy alloy by cooperative planar slipping and twinning, *Materialia* 8 (2019) 100485, <https://doi.org/10.1016/j.matla.2019.100485>.
- [6] Z. Li, K.G. Pradeep, Y. Deng, D. Raabe, C.C. Tasan, Metastable high-entropy dual-phase alloys overcome the strength–ductility trade-off, *Nature* 534 (2016) 227–230, <https://doi.org/10.1038/nature17981>.
- [7] J. Su, D. Raabe, Z. Li, Hierarchical microstructure design to tune the mechanical behavior of an interstitial TRIP-TWIP high-entropy alloy, *Acta Mater.* 163 (2019) 40–54, <https://doi.org/10.1016/j.actamat.2018.10.017>.
- [8] E. Polatidis, S. Shukla, J. Čapek, S. Van Petegem, N. Casati, R.S.S. Mishra, Unveiling the interplay of deformation mechanisms in a metastable high entropy alloy with tuned composition using synchrotron X-ray diffraction, *Mater. Today Commun.* 30 (2022) 103155, <https://doi.org/10.1016/j.mtcomm.2022.103155>.
- [9] A.V. Ayyagari, B. Gwalani, S. Muskeri, S. Mukherjee, R. Banerjee, Surface degradation mechanism in precipitation-hardened high-entropy alloys, *Npj Mater. Degrad.* 2 (2018) 33, <https://doi.org/10.1038/s41529-018-0054-1>.
- [10] Z. Li, C.C. Tasan, H. Springer, B. Gault, D. Raabe, Interstitial atoms enable joint twinning and transformation induced plasticity in strong and ductile high-entropy alloys, *Sci. Rep.* 7 (2017) 40704, <https://doi.org/10.1038/srep40704>.
- [11] S.M. Vakili, A. Zarei-Hanzaki, A.S. Anoush, H.R. Abedi, M.H. Mohammad-Ebrahimi, M. Jaskari, S.S. Sohn, D. Ponge, L.P. Karjalainen, Reversible dislocation movement, martensitic transformation and nano-twining during elastic cyclic loading of a metastable high entropy alloy, *Acta Mater.* 185 (2020) 474–492, <https://doi.org/10.1016/j.actamat.2019.12.040>.
- [12] P. Agrawal, R.S. Haridas, S. Thapliyal, S. Yadav, R.S. Mishra, B.A. McWilliams, K. C. Cho, Metastable high entropy alloys: An excellent defect tolerant material for additive manufacturing, *Mater. Sci. Eng. A* 826 (2021) 142005, <https://doi.org/10.1016/j.msea.2021.142005>.
- [13] A.A. Saleh, D.W. Brown, E.V. Pereloma, B. Clausen, C.H.J. Davies, C.N. Tomé, A. A. Gazder, An in-situ neutron diffraction study of a multi-phase transformation and twinning-induced plasticity steel during cyclic loading, *Appl. Phys. Lett.* 106 (2015) 171911, <https://doi.org/10.1063/1.4919455>.
- [14] S.S. Nene, M. Frank, K. Liu, R.S. Mishra, B.A. McWilliams, K.C. Cho, Extremely high strength and work hardening ability in a metastable high entropy alloy, *Sci. Rep.* 8 (2018) 9920, <https://doi.org/10.1038/s41598-018-28383-0>.
- [15] R. Xiong, H. Peng, H. Si, W. Zhang, Y. Wen, Thermodynamic calculation of stacking fault energy of the Fe–Mn–Si–C high manganese steels, *Mater. Sci. Eng. A* 598 (2014) 376–386, <https://doi.org/10.1016/j.msea.2014.01.046>.
- [16] K. Liu, S.S. Nene, M. Frank, R.S. Mishra, Effect of Strain Rate on Deformation Response of Metastable High Entropy Alloys Upon Friction Stir Processing, *Metall. Mater. Trans. A* 51 (2020) 5043–5048, <https://doi.org/10.1007/s11661-020-05927-6>.
- [17] J. Ahmed, M. Daly, Yield strength insensitivity in a dual-phase high entropy alloy after prolonged high temperature annealing, *Mater. Sci. Eng. A* 820 (2021) 141586, <https://doi.org/10.1016/j.msea.2021.141586>.
- [18] M. Frank, S.S. Nene, Y. Chen, S. Thapliyal, S. Shukla, K. Liu, S. Sinha, T. Wang, M. J. Frost, K. An, R.S. Mishra, Direct evidence of the stacking fault-mediated strain hardening phenomenon, *Appl. Phys. Lett.* 119 (2021) 081906, <https://doi.org/10.1063/5.0062153>.
- [19] M. Frank, Y. Chen, S.S. Nene, S. Sinha, K. Liu, K. An, R.S. Mishra, Investigating the deformation mechanisms of a highly metastable high entropy alloy using in-situ neutron diffraction, *Mater. Today Commun.* 23 (2020) 100858, <https://doi.org/10.1016/j.mtcomm.2019.100858>.
- [20] A. Sittitho, M. Bhattacharya, J. Graves, S.S. Nene, R.S. Mishra, I. Charit, Friction stir processing of a high entropy alloy Fe42Co10Cr15Mn28Si5 with transformative characteristics: Microstructure and mechanical properties, *Mater. Today Commun.* 28 (2021) 102635, <https://doi.org/10.1016/j.mtcomm.2021.102635>.
- [21] A.P. Hammersley, S.O. Svensson, A. Thompson, Calibration and correction of spatial distortions in 2D detector systems, *Nucl. Instruments Methods Phys. Res. Sect. A Accel. Spectrometers, Detect. Assoc. Equip.* 346 (1994) 312–321, [https://doi.org/10.1016/0168-9002\(94\)90720-X](https://doi.org/10.1016/0168-9002(94)90720-X).
- [22] B.H. Toby, R.B. Von Dreele, GSAS-II : the genesis of a modern open-source all purpose crystallography software package, *J. Appl. Crystallogr.* 46 (2013) 544–549, <https://doi.org/10.1107/S0021889813003531>.
- [23] L. Lutterotti, S. Matthies, H.-R. Wenk, A.S. Schultz, J.W. Richardson, Combined texture and structure analysis of deformed limestone from time-of-flight neutron diffraction spectra, *J. Appl. Phys.* 81 (1997) 594–600, <https://doi.org/10.1063/1.364220>.
- [24] L. Lutterotti, P. Scardi, Simultaneous structure and size-strain refinement by the Rietveld method, *J. Appl. Crystallogr.* 23 (1990) 246–252, <https://doi.org/10.1107/S0021889890002382>.
- [25] A.I. Saville, A. Creuziger, E.B. Mitchell, S.C. Vogel, J.T. Benzing, J. Kleemann-Toole, K.D. Clarke, A.J. Clarke, MAUD Rietveld Refinement Software for Neutron Diffraction Texture Studies of Single- and Dual-Phase Materials, *Integr. Mater. Manuf. Innov.* 10 (2021) 461–487, <https://doi.org/10.1007/s40192-021-00224-5>.
- [26] N.C. Popa, The (hkl) Dependence of Diffraction-Line Broadening Caused by Strain and Size for all Laue Groups in Rietveld Refinement, *J. Appl. Crystallogr.* 31 (1998) 176–180, <https://doi.org/10.1107/S0021889897009795>.
- [27] L. Lutterotti, D. Chateigner, S. Ferrari, J. Ricote, Texture, residual stress and structural analysis of thin films using a combined X-ray analysis, *Thin Solid Films* 450 (2004) 34–41, <https://doi.org/10.1016/j.tsf.2003.10.150>.
- [28] H.-R. Wenk, L. Lutterotti, S. Vogel, Texture analysis with the new HIPPO TOF diffractometer, *Nucl. Instruments Methods Phys. Res. Sect. A Accel. Spectrometers, Detect. Assoc. Equip.* 515 (2003) 575–588, <https://doi.org/10.1016/j.nima.2003.05.001>.
- [29] H.-R. Wenk, L. Lutterotti, P. Kaercher, W. Kanitpanyacharoen, L. Miyagi, R. Vasin, Rietveld texture analysis from synchrotron diffraction images. II. Complex multiphase materials and diamond anvil cell experiments, *Powder Diffr.* 29 (2014) 220–232, <https://doi.org/10.1017/S0885715614000360>.
- [30] C.E. Tommaso, J. Devine, S. Merkel, S. Spezzale, H.-R. Wenk, Texture development and elastic stresses in magnesiowüstite at high pressure, *Phys. Chem. Miner.* 33 (2006) 84–97, <https://doi.org/10.1007/s00269-005-0054-x>.
- [31] X. Li, D.L. Irving, L. Vitos, First-principles investigation of the micromechanical properties of fcc-hcp polymorphic high-entropy alloys, *Sci. Rep.* 8 (2018) 11196, <https://doi.org/10.1038/s41598-018-29588-z>.
- [32] H. Search, C. Journals, A. Contact, M. Iopscience, I.P. Address, The Elastic Behaviour of a Crystalline Aggregate, 349 (1952). <https://doi.org/0370-1298/65/5/307>.
- [33] J.-Q. Zhao, H. Tian, Z. Wang, X.-J. Wang, J.-W. Qiao, FCC-to-HCP Phase Transformation in CoCrNiX Medium-Entropy Alloys, *Acta Metall. Sin. (english Lett.)* 33 (2020) 1151–1158, <https://doi.org/10.1007/s40195-020-01080-6>.
- [34] Y. Shi, S. Li, T.L. Lee, X. Hui, Z. Zhang, R. Li, M. Zhang, S. Kabra, Y.-D. Wang, In situ neutron diffraction study of a new type of stress-induced confined martensitic transformation in Fe22Co20Ni19Cr20Mn12Al7 high-entropy alloy, *Mater. Sci. Eng. A* 771 (2020) 138555, <https://doi.org/10.1016/j.msea.2019.138555>.
- [35] L. Ma, L. Wang, Z. Nie, F. Wang, Y. Xue, J. Zhou, T. Cao, Y. Wang, Y. Ren, Reversible deformation-induced martensitic transformation in Al0.6CoCrFeNi high-entropy alloy investigated by in situ synchrotron-based high-energy X-ray diffraction, *Acta Mater.* 128 (2017) 12–21, <https://doi.org/10.1016/j.jactamat.2017.02.014>.
- [36] S. Agnew, D. Brown, C. Tome, Validating a polycrystal model for the elastoplastic response of magnesium alloy AZ31 using in situ neutron diffraction, *Acta Mater.* 54 (2006) 4841–4852, <https://doi.org/10.1016/j.actamat.2006.06.020>.
- [37] K. Mo, Z. Zhou, Y. Miao, D. Yun, H.-M. Tung, G. Zhang, W. Chen, J. Almer, J. F. Stubbins, Synchrotron study on load partitioning between ferrite/martensite and nanoparticles of a 9Cr ODS steel, *J. Nucl. Mater.* 455 (2014) 376–381, <https://doi.org/10.1016/j.jnucmat.2014.06.060>.
- [38] M.L. Young, J.D. Almer, M.R. Daymond, D.R. Haefner, D.C. Dunand, Load partitioning between ferrite and cementite during elasto-plastic deformation of an ultrahigh-carbon steel, *Acta Mater.* 55 (2007) 1999–2011, <https://doi.org/10.1016/j.actamat.2006.11.004>.
- [39] N.R. Jaladurgam, A. Lozinko, S. Guo, T.L. Lee, M. Hörmqvist Colliander, Temperature dependent load partitioning and slip mode transition in a eutectic AlCoCrFeNi2.1 high entropy alloy, *Materialia*. 17 (2021) 101118, <https://doi.org/10.1016/j.matla.2021.101118>.
- [40] S. Gao, T. Yoshimura, W. Mao, Y. Bai, W. Gong, M. Park, A. Shibata, H. Adachi, M. Sato, N. Tsuji, Tensile Deformation of Ultrafine-Grained Fe-Mn-Al-Ni-C Alloy Studied By In Situ Synchrotron Radiation X-ray Diffraction, *Crystals*. 10 (2020) 1115, <https://doi.org/10.3390/crust10121115>.
- [41] B.B. He, B. Hu, H.W. Yen, G.J. Cheng, Z.K. Wang, H.W. Luo, M.X. Huang, High dislocation density-induced large ductility in deformed and partitioned steels, *Science* (80+) 357 (2017) 1029–1032. <https://doi.org/10.1126/science.aan0177>.
- [42] P. Hirsch, D. Cockayne, J. Spence, M. Whelan, 50 Years of TEM of dislocations: Past, present and future, *Philos. Mag.* 86 (2006) 4519–4528, <https://doi.org/10.1080/14786430600768634>.
- [43] R.A. Renzetti, H.R.Z. Sandim, R.E. Bolmaro, P.A. Suzuki, A. Möslang, X-ray evaluation of dislocation density in ODS-Eurofer steel, *Mater. Sci. Eng. A* 534 (2012) 142–146, <https://doi.org/10.1016/j.msea.2011.11.051>.
- [44] I. Gutierrez-Urrutia, J.A. del Valle, S. Zaeferer, D. Raabe, Study of internal stresses in a TWIP steel analyzing transient and permanent softening during reverse shear tests, *J. Mater. Sci.* 45 (2010) 6604–6610, <https://doi.org/10.1007/s10853-010-4750-7>.
- [45] D. Akama, T. Tsuchiyama, S. Takaki, Change in Dislocation Characteristics with Cold Working in Ultralow-carbon Martensitic Steel, *ISIJ Int.* 56 (2016) 1675–1680, <https://doi.org/10.2355/isijinternational.ISIJINT-2016-140>.
- [46] K.D. Rogers, P. Daniels, An X-ray diffraction study of the effects of heat treatment on bone mineral microstructure, *Biomaterials*. 23 (2002) 2577–2585, [https://doi.org/10.1016/S0142-9612\(01\)00395-7](https://doi.org/10.1016/S0142-9612(01)00395-7).

- [47] A. Khorsand Zak, W.H. Abd, M.E. Majid, R.Y. Abrishami, X-ray analysis of ZnO nanoparticles by Williamson-Hall and size-strain plot methods, *Solid State Sci.* 13 (2011) 251–256, <https://doi.org/10.1016/j.solidstatosciences.2010.11.024>.
- [48] R.D. Deslattes, X-ray fluorescence spectroscopy, *Nucl. Instruments Methods Phys. Res.* 208 (1983) 655–658, [https://doi.org/10.1016/0167-5087\(83\)91200-0](https://doi.org/10.1016/0167-5087(83)91200-0).
- [49] M.R. Panigrahi, S. Panigrahi, Structural analysis of 100% relative intense peak of Ba_{1-x}CaxTiO₃ ceramics by X-ray powder diffraction method, *Phys. B Condens. Matter.* 405 (2010) 1787–1791, <https://doi.org/10.1016/j.physb.2010.01.040>.
- [50] K. Venkateswarlu, A. Chandra Bose, N. Rameshbabu, X-ray peak broadening studies of nanocrystalline hydroxyapatite by Williamson-Hall analysis, *Phys. B Condens. Matter.* 405 (2010) 4256–4261, <https://doi.org/10.1016/j.physb.2010.07.020>.
- [51] H. Cheng, H.Y. Wang, Y.C. Xie, Q.H. Tang, P.Q. Dai, Controllable fabrication of a carbide-containing FeCoCrNiMn high-entropy alloy: microstructure and mechanical properties, *Mater. Sci. Technol. (United Kingdom)* 33 (2017) 2032–2039, <https://doi.org/10.1080/02670836.2017.1342367>.
- [52] Y. Miyajima, S. Okubo, T. Miyazawa, H. Adachi, T. Fujii, In-situ X-ray diffraction during tensile deformation of ultrafine-grained copper using synchrotron radiation, *Philos. Mag. Lett.* 96 (2016) 294–304, <https://doi.org/10.1080/09500839.2016.1218563>.
- [53] M. Wang, M. Knezevic, H. Gao, J. Wang, M. Kang, B. Sun, Phase interface induced stacking faults in Al-7.5Y alloy revealed by in-situ synchrotron X-ray diffraction and ex-situ electron microscopy, *Mater. Charact.* 179 (2021) 111322, <https://doi.org/10.1016/j.matchar.2021.111322>.
- [54] Y.T. Prabhu, K.V. Rao, V.S.S. Kumar, B.S. Kumari, X-Ray Analysis by Williamson-Hall and Size-Strain Plot Methods of ZnO Nanoparticles with Fuel Variation, *World J. Nano Sci. Eng.* 04 (2014) 21–28, <https://doi.org/10.4236/wjNSE.2014.41004>.
- [55] G. Williamson, W. Hall, X-ray line broadening from filed aluminium and wolfram, *Acta Metall.* 1 (1953) 22–31, [https://doi.org/10.1016/0001-6160\(53\)90006-6](https://doi.org/10.1016/0001-6160(53)90006-6).
- [56] J. Wiley, Fundamentals of Materials Science and Engineering An Interactive, Bi-Comp, Inc., and printed and bound by Von Hoffmann Press, n.d.
- [57] R.E. Smallman, A.H.W. Ngan, Introduction to Dislocations, in: *Mod. Phys. Metall.*, Elsevier, 2014: pp. 121–158. <https://doi.org/10.1016/B978-0-08-098204-5.00004-3>.
- [58] B.C. De Cooman, Y. Estrin, S.K. Kim, Twinning-induced plasticity (TWIP) steels, *Acta Mater.* 142 (2018) 283–362, <https://doi.org/10.1016/j.actamat.2017.06.046>.
- [59] R. Xiong, H. Peng, T. Zhang, J.W. Bae, H.S. Kim, Y. Wen, Superior strain-hardening by deformation-induced nano-HCP martensite in Fe–Mn–Si–C high-manganese steel, *Mater. Sci. Eng. A* 824 (2021) 141864, <https://doi.org/10.1016/j.msea.2021.141864>.
- [60] T.S. Byun, On the stress dependence of partial dislocation separation and deformation microstructure in austenitic stainless steels, *Acta Mater.* 51 (2003) 3063–3071, [https://doi.org/10.1016/S1359-6454\(03\)00117-4](https://doi.org/10.1016/S1359-6454(03)00117-4).
- [61] F.F. Lavrentev, Y.A. Pokhil, Relation of dislocation density in different slip systems to work hardening parameters for magnesium crystals, *Mater. Sci. Eng.* 18 (1975) 261–270, [https://doi.org/10.1016/0025-5416\(75\)90179-2](https://doi.org/10.1016/0025-5416(75)90179-2).
- [62] Y. Bu, Z. Li, J. Liu, H. Wang, D. Raabe, W. Yang, Nonbasal Slip Systems Enable a Strong and Ductile Hexagonal-Close-Packed High-Entropy Phase, *Phys. Rev. Lett.* 122 (2019) 075502, <https://doi.org/10.1103/PhysRevLett.122.075502>.
- [63] K. Yamanaka, M. Mori, S. Sato, A. Chiba, Stacking-fault strengthening of biomedical Co–Cr–Mo alloy via multipass thermomechanical processing, *Sci. Rep.* 7 (2017) 10808, <https://doi.org/10.1038/s41598-017-10305-1>.
- [64] J.G. Kim, N.A. Enikeev, J.B. Seol, M.M. Abramova, M.V. Karavaeva, R.Z. Valiev, C.G. Park, H.S. Kim, Superior Strength and Multiple Strengthening Mechanisms in Nanocrystalline TWIP Steel, *Sci. Rep.* 8 (2018) 11200, <https://doi.org/10.1038/s41598-018-29632-y>.
- [65] M. Samiuddin, J. Li, A.D. Chandio, M. Muzamil, S.U. Siddiqui, J. Xiong, Diffusion welding of CoCrNi medium entropy alloy (MEA) and SUS 304 stainless steel at different bonding temperatures, *Weld. World.* 65 (2021) 2193–2206, <https://doi.org/10.1007/s40194-021-01165-5>.
- [66] S.S. Nene, K. Liu, S. Sinha, M. Frank, S. Williams, R.S. Mishra, Superplasticity in fine grained dual phase high entropy alloy, *Materialia.* 9 (2020) 100521, <https://doi.org/10.1016/j.jmsta.2019.100521>.
- [67] S. Sinha, S.S. Nene, M. Frank, K. Liu, R.A. Lebensohn, R.S. Mishra, Deformation mechanisms and ductile fracture characteristics of a friction stir processed transformative high entropy alloy, *Acta Mater.* 184 (2020) 164–178, <https://doi.org/10.1016/j.actamat.2019.11.056>.
- [68] H.Y. Yasuda, K. Shigeno, T. Nagase, Dynamic strain aging of Al 0.3 CoCrFeNi high entropy alloy single crystals, *Scr. Mater.* 108 (2015) 80–83, <https://doi.org/10.1016/j.scriptamat.2015.06.022>.
- [69] Z. Li, C.C. Tasan, K.G. Pradeep, D. Raabe, A TRIP-assisted dual-phase high-entropy alloy: Grain size and phase fraction effects on deformation behavior, *Acta Mater.* 131 (2017) 323–335, <https://doi.org/10.1016/j.actamat.2017.03.069>.
- [70] T. Holden, D.W. Brown, B. Clausen, H. Suzuki, Search for Evidence of Stacking Faults in Austenitic Stainless Steel Alloys by Neutron Diffraction, *Mater. Sci. Forum.* 652 (2010) 129–132, <https://doi.org/10.4028/www.scientific.net/MSF.652.129>.
- [71] J.S. Jeong, W. Woo, K.H. Oh, S.K. Kwon, Y.M. Koo, In situ neutron diffraction study of the microstructure and tensile deformation behavior in Al-added high manganese austenitic steels, *Acta Mater.* 60 (2012) 2290–2299, <https://doi.org/10.1016/j.actamat.2011.12.043>.
- [72] S.F. Liu, Y. Wu, H.T. Wang, W.T. Lin, Y.Y. Shang, J.B. Liu, K. An, X.J. Liu, H. Wang, Z.P. Lu, Transformation-reinforced high-entropy alloys with superior mechanical properties via tailoring stacking fault energy, *J. Alloys Compd.* 792 (2019) 444–455, <https://doi.org/10.1016/j.jallcom.2019.04.035>.
- [73] M. Kang, W. Woo, Y.-K. Lee, B.-S. Seong, Neutron diffraction analysis of stacking fault energy in Fe–18Mn–2Al–0.6C twinning-induced plasticity steels, *Mater. Lett.* 76 (2012) 93–95, <https://doi.org/10.1016/j.matlet.2012.02.075>.
- [74] B. Cai, B. Liu, S. Kabra, Y. Wang, K. Yan, P.D. Lee, Y. Liu, Deformation mechanisms of Mo alloyed FeCoCrNi high entropy alloy: In situ neutron diffraction, *Acta Mater.* 127 (2017) 471–480, <https://doi.org/10.1016/j.actamat.2017.01.034>.
- [75] H.S. Lipson, X-ray diffraction by B. E. Warren, *Acta Crystallogr. Sect. A* 27 (1971) 192, <https://doi.org/10.1107/S0567739471000445>.
- [76] C. Haase, F. Tang, M.B. Wilms, A. Weisheit, B. Hallstedt, C. Varvenne, A. Luque, W.A. Curtin, I. Toda-Caraballos, S. Oliver, L. Zhao, A.J. Gormley, R. Chapman, C. Boyer, Y. Li, K. Yang, S. Liu, B.B. Kappes, B. Amin-ahmadi, O. Benafan, X. Zhang, A.P. Stebner, S. Luo, T. Li, X. Wang, M. Faizan, L. Zhang, F.G. Coury, P. Wilson, K.D. Clarke, M.J. Kaufman, A.J. Clarke, S.Z. Han, E.A. Choi, S.H. Lim, S. Kim, J. Lee, S. Ranganathan, A general formulation for solid solution hardening effect in multicomponent alloys, *Acta Mater.* 167 (2019) 100898, <https://doi.org/10.1016/j.msea.2017.01.099>.
- [77] M. Frank, S.S. Nene, B. Gwalani, E.J. Kautz, A. Devaraj, K. An, R. S. Mishra, Correlating work hardening with co-activation of stacking fault strengthening and transformation in a high entropy alloy using in-situ neutron diffraction, *Sci. Rep.* 10 (2020) 22263, <https://doi.org/10.1038/s41598-020-79492-8>.
- [78] W.W. Jian, G.M. Cheng, W.Z. Xu, H. Yuan, M.H. Tsai, Q.D. Wang, C.C. Koch, Y. T. Zhu, S.N. Mathaudhu, Ultrastrong Mg Alloy via Nano-spaced Stacking Faults, *Mater. Res. Lett.* 1 (2013) 61–66, <https://doi.org/10.1080/21663831.2013.765927>.
- [79] S. Sinha, S.S. Nene, M. Frank, K. Liu, P. Agrawal, R.S. Mishra, On the evolving nature of c/a ratio in a hexagonal close-packed epsilon martensite phase in transformative high entropy alloys, *Sci. Rep.* 9 (2019) 13185, <https://doi.org/10.1038/s41598-019-49904-5>.
- [80] J. Shen, P. Agrawal, T.A. Rodrigues, J.G. Lopes, N. Schell, J. He, Z. Zeng, R. S. Mishra, J.P. Oliveira, Microstructure evolution and mechanical properties in a gas tungsten arc welded Fe42Mn28Co10Cr15Si5 metastable high entropy alloy, *Mater. Sci. Eng. A* 867 (2023) 144722, <https://doi.org/10.1016/j.msea.2023.144722>.
- [81] S. Bhowmik, J. Zhang, S.C. Vogel, S.S. Nene, R.S. Mishra, B.A. McWilliams, M. Knezevic, Effects of plasticity-induced martensitic transformation and grain refinement on the evolution of microstructure and mechanical properties of a metastable high entropy alloy, *J. Alloys Compd.* 891 (2022) 161871, <https://doi.org/10.1016/j.jallcom.2021.161871>.
- [82] T. Gebhardt, D. Music, M. Ekholm, I.A. Abrikosov, L. Vitos, A. Dick, T. Hickel, J. Neugebauer, J.M. Schneider, The influence of additions of Al and Si on the lattice stability of fcc and hcp Fe–Mn random alloys, *J. Phys. Condens. Matter.* 23 (2011) 1–8, <https://doi.org/10.1088/0953-8984/23/24/246003>.
- [83] N. Stanford, D.P. Dunne, Effect of Si on the reversibility of stress-induced martensite in Fe–Mn–Si shape memory alloys, *Acta Mater.* 58 (2010) 6752–6762, <https://doi.org/10.1016/j.actamat.2010.08.041>.
- [84] S. Wei, J. Kim, C.C. Tasan, Boundary micro-cracking in metastable Fe45Mn35Co10Cr10 high-entropy alloys, *Acta Mater.* 168 (2019) 76–86, <https://doi.org/10.1016/j.actamat.2019.01.036>.
- [85] H. Huang, Y. Wu, J. He, H. Wang, X. Liu, K. An, W. Wu, Z. Lu, Phase-Transformation Ductilization of Brittle High-Entropy Alloys via Metastability Engineering, *Adv. Mater.* 29 (2017) 1701678, <https://doi.org/10.1002/adma.201701678>.
- [86] K.Y. Xie, Z. Alam, A. Caffee, K.J. Hemker, Pyramidal I slip in c-axis Compressed Mg Single Crystals, (2015).
- [87] S. Fu, H. Bei, Y. Chen, T.K. Liu, D. Yu, K. An, Deformation mechanisms and work-hardening behavior of transformation-induced plasticity high entropy alloys by in-situ neutron diffraction, *Mater. Res. Lett.* 6 (2018) 620–626, <https://doi.org/10.1080/21663831.2018.1523239>.
- [88] D.T. Pierce, J.A. Jiménez, J. Bentley, D. Raabe, J.E. Wittig, The influence of stacking fault energy on the microstructural and strain-hardening evolution of Fe–Mn–Al–Si steels during tensile deformation, *Acta Mater.* 100 (2015) 178–190, <https://doi.org/10.1016/j.actamat.2015.08.030>.
- [89] Y. Deng, C.C. Tasan, K.G. Pradeep, H. Springer, A. Kostka, D. Raabe, Design of a twinning-induced plasticity high entropy alloy, *Acta Mater.* 94 (2015) 124–133, <https://doi.org/10.1016/j.actamat.2015.04.014>.
- [90] N. Kumar, M. Komarasamy, P. Nelaturu, Z. Tang, P.K. Liaw, R.S. Mishra, Friction Stir Processing of a High Entropy Alloy Al.0.1CoCrFeNi, *JOM.* 67 (2015) 1007–1013, <https://doi.org/10.1007/s11837-015-1385-9>.
- [91] Z. Li, F. Körmann, B. Grabowski, J. Neugebauer, D. Raabe, Ab initio assisted design of quinary dual-phase high-entropy alloys with transformation-induced plasticity, *Acta Mater.* 136 (2017) 262–270, <https://doi.org/10.1016/j.actamat.2017.07.023>.
- [92] M. Calcagnotto, D. Ponge, E. Demir, D. Raabe, Orientation gradients and geometrically necessary dislocations in ultrafine grained dual-phase steels studied by 2D and 3D EBSD, *Mater. Sci. Eng. A* 527 (2010) 2738–2746, <https://doi.org/10.1016/j.msea.2010.01.004>.
- [93] S. Papula, S. Anttila, J. Talonen, T. Sarikka, I. Virkkunen, H. Hänninen, Strain hardening of cold-rolled lean-alloyed metastable ferritic-austenitic stainless steels, *Mater. Sci. Eng. A* 677 (2016) 11–19, <https://doi.org/10.1016/j.msea.2016.09.038>.

- [94] C.L. Yang, Z.J. Zhang, T. Cai, P. Zhang, Z.F. Zhang, Recovery of strain-hardening rate in Ni-Si alloys, *Sci. Rep.* 5 (2015) 15532, <https://doi.org/10.1038/srep15532>.
- [95] M.A. Gharaghouri, G.C. Weatherly, J.D. Embury, The interaction of twins and precipitates in a Mg-7.7 at.% Al alloy, *Philos. Mag. A* 78 (1998) 1137–1149, <https://doi.org/10.1080/01418619808239980>.
- [96] S. Sinha, A. Pukenas, A. Ghosh, A. Singh, W. Skrotzki, N.P. Gurao, Effect of initial orientation on twinning in commercially pure titanium, *Philos. Mag. A* 97 (2017) 775–797, <https://doi.org/10.1080/14786435.2017.1279364>.
- [97] Y.T. Zhu, Deformation Twinning in a Nanocrystalline Hcp Mg Alloy 64 (2011) 213–216, <https://doi.org/10.1016/j.scriptamat.2010.10.024>.
- [98] S.S. Nene, M. Frank, K. Liu, S. Sinha, R.S. Mishra, B.A. McWilliams, K.C. Cho, Corrosion-resistant high entropy alloy with high strength and ductility, *Scr. Mater.* 166 (2019) 168–172, <https://doi.org/10.1016/j.scriptamat.2019.03.028>.
- [99] S.S. Nene, K. Liu, M. Frank, R.S. Mishra, R.E. Brennan, K.C. Cho, Z. Li, D. Raabe, Enhanced strength and ductility in a friction stir processing engineered dual phase high entropy alloy, *Sci. Rep.* 7 (2017) 16167, <https://doi.org/10.1038/s41598-017-16509-9>.
- [100] O. Muránsky, P. Šittner, J. Zrník, E.C. Oliver, In situ neutron diffraction investigation of the collaborative deformation-transformation mechanism in TRIP-assisted steels at room and elevated temperatures, *Acta Mater.* 56 (2008) 3367–3379, <https://doi.org/10.1016/j.actamat.2008.03.026>.
- [101] O. Gra, L. Kru, G. Frommeyer, L.W. Meyer, High Strength Fe ± Mn ± (Al, Si) TRIP / TWIP Steels Development D Properties D Application 16 (2000) 1391–1409.
- [102] K. Yan, K. Liss, I.B. Timokhina, E.V. Pereloma, In situ synchrotron X-ray diffraction studies of the effect of microstructure on tensile behavior and retained austenite stability of thermo-mechanically processed transformation induced plasticity steel, *Mater. Sci. Eng. A* 662 (2016) 185–197, <https://doi.org/10.1016/j.msea.2016.03.048>.
- [103] G. Niu, Q. Tang, H.S. Zurob, H. Wu, L. Xu, N. Gong, Strong and ductile steel via high dislocation density and heterogeneous nano/ultrafine grains, *Mater. Sci. Eng. A* 759 (2019) 1–10, <https://doi.org/10.1016/j.msea.2019.04.112>.
- [104] Y. Han, H. Li, H. Feng, K. Li, Y. Tian, Z. Jiang, Simultaneous enhancement in strength and ductility of Fe50Mn30Co10Cr10 high-entropy alloy via nitrogen alloying, *J. Mater. Sci. Technol.* 65 (2021) 210–215, <https://doi.org/10.1016/j.jmst.2020.04.072>.
- [105] A.V. Drucker, A. Perotti, I. Esquivel, J. Malarria, Design of Devices and Manufacturing of Fe-Mn-Si Shape Memory Alloy Couplings, *Procedia, Mater. Sci.* 8 (2015) 878–885, <https://doi.org/10.1016/j.mspro.2015.04.148>.
- [106] R.S. Mishra, R.S. Haridas, P. Agrawal, High entropy alloys – Tunability of deformation mechanisms through integration of compositional and microstructural domains, *Mater. Sci. Eng. A* 812 (2021) 141085, <https://doi.org/10.1016/j.msea.2021.141085>.
- [107] S.S. Nene, M. Frank, K. Liu, S. Sinha, R.S. Mishra, B. McWilliams, K.C. Cho, Reversed strength-ductility relationship in microstructurally flexible high entropy alloy, *Scr. Mater.* 154 (2018) 163–167, <https://doi.org/10.1016/j.scriptamat.2018.05.043>.
- [108] O. Bouaziz, N. Guerton, Modelling of TWIP effect on work-hardening, *Mater. Sci. Eng. A* 319–321 (2001) 246–249, [https://doi.org/10.1016/S0921-5093\(00\)02019-0](https://doi.org/10.1016/S0921-5093(00)02019-0).
- [109] W. Woo, J.S. Jeong, D.-K. Kim, C.M. Lee, S.-H. Choi, J.-Y. Suh, S.Y. Lee, S. Harjo, T. Kawasaki, Stacking Fault Energy Analyses of Additively Manufactured Stainless Steel 316L and CrCoNi Medium Entropy Alloy Using In Situ Neutron Diffraction, *Sci. Rep.* 10 (2020) 1350, <https://doi.org/10.1038/s41598-020-58273-3>.
- [110] S. Martin, C. Ullrich, D. Rafaja, Deformation of Austenitic CrMnNi TRIP/TWIP Steels: Nature and Role of the ϵ -martensite, *Mater. Today Proc.* 2 (2015) S643–S646, <https://doi.org/10.1016/j.matpr.2015.07.366>.
- [111] Y.Y. Shang, Y. Wu, J.Y. He, X.Y. Zhu, S.F. Liu, H.L. Huang, K. An, Y. Chen, S. H. Jiang, H. Wang, X.J. Liu, Z.P. Lu, Solving the strength-ductility tradeoff in the medium-entropy NiCoCr alloy via interstitial strengthening of carbon, *Intermetallics* 106 (2019) 77–87, <https://doi.org/10.1016/j.intermet.2018.12.009>.
- [112] Y. Wang, B. Liu, K. Yan, M. Wang, S. Kabra, Y.-L. Chiu, D. Dye, P.D. Lee, Y. Liu, B. Cai, Probing deformation mechanisms of a FeCoCrNi high-entropy alloy at 293 and 77 K using in situ neutron diffraction, *Acta Mater.* 154 (2018) 79–89, <https://doi.org/10.1016/j.actamat.2018.05.013>.
- [113] A. Reviews, Quick links to online content, n.d.
- [114] Q. Fang, Y. Chen, J. Li, C. Jiang, B. Liu, Y. Liu, P.K. Liaw, Probing the phase transformation and dislocation evolution in dual-phase high-entropy alloys, *Int. J. Plast.* 114 (2019) 161–173, <https://doi.org/10.1016/j.ijplas.2018.10.014>.
- [115] S. Mahajan, M.L. Green, D. Brasen, A model for the FCC→HCP transformation, its applications, and experimental evidence, *Mater. Trans. A* 8 (1977) 283–293, <https://doi.org/10.1007/BF02661642>.
- [116] S.S. Nene, S. Sinha, M. Frank, K. Liu, R.S. Mishra, B.A. McWilliams, K.C. Cho, Unexpected strength-ductility response in an annealed, metastable, high-entropy alloy, *Appl. Mater. Today.* 13 (2018) 198–206, <https://doi.org/10.1016/j.apmt.2018.09.002>.
- [117] S. Hyuk Park, S. Hong, C.S. Lee, In-plane anisotropic deformation behavior of rolled Mg-3Al-1Zn alloy by initial 10–12 twins, *Mater. Sci. Eng. A* 570 (2013) 149–163, <https://doi.org/10.1016/j.msea.2013.01.071>.
- [118] O. Muránsky, M.R. Barnett, D.G. Carr, S.C. Vogel, E.C. Oliver, Investigation of deformation twinning in a fine-grained and coarse-grained ZM20 Mg alloy: Combined in situ neutron diffraction and acoustic emission, *Acta Mater.* 58 (2010) 1503–1517, <https://doi.org/10.1016/j.actamat.2009.10.057>.
- [119] D. Sarker, D.L. Chen, Texture transformation in an extruded magnesium alloy under pressure, *Mater. Sci. Eng. A* 582 (2013) 63–67, <https://doi.org/10.1016/j.msea.2013.06.048>.
- [120] L. Song, B. Wu, L. Zhang, X. Du, Y. Wang, C. Esling, Twinning characterization of fiber-textured AZ31B magnesium alloy during tensile deformation, *Mater. Sci. Eng. A* 710 (2018) 57–65, <https://doi.org/10.1016/j.msea.2017.10.055>.
- [121] K. Hantsche, J. Bohlen, J. Wendt, K.U. Kainer, S.B. Yi, D. Letzig, Effect of rare earth additions on microstructure and texture development of magnesium alloy sheets, *Scr. Mater.* 63 (2010) 725–730, <https://doi.org/10.1016/j.scriptamat.2009.12.033>.
- [122] B.C. Wonsiewicz, *Plasticity of Magnesium Crystals*, S.B., Massachusetts Institute of Technology, 1966.
- [123] J. Koike, Enhanced deformation mechanisms by anisotropic plasticity in polycrystalline Mg alloys at room temperature, *Metall. Mater. Trans. A* 36 (2005) 1689–1696, <https://doi.org/10.1007/s11661-005-0032-4>.
- [124] B.L. Wu, Y.D. Zhang, G. Wan, M. Humbert, F. Wagner, C. Esling, Primary twinning selection with respect to orientation of deformed grains in ultra-rapidly compressed AZ31 alloy, *Mater. Sci. Eng. A* 541 (2012) 120–127, <https://doi.org/10.1016/j.msea.2012.02.012>.
- [125] J.R. Bingert, T.A. Mason, G.C. Kaschner, G.T. Gray, P.J. Maudlin, Deformation twinning in polycrystalline Zr: Insights from electron backscattered diffraction characterization, *Metall. Mater. Trans. A* 33 (2002) 955–963, <https://doi.org/10.1007/s11661-002-0165-7>.
- [126] S. Lee, S.-J. Lee, B.C. De Cooman, Austenite stability of ultrafine-grained transformation-induced plasticity steel with Mn partitioning, *Scr. Mater.* 65 (2011) 225–228, <https://doi.org/10.1016/j.scriptamat.2011.04.010>.
- [127] S. Chatterjee, H.-S. Wang, J.R. Yang, H.K.D.H. Bhadeshia, Mechanical stabilisation of austenite, *Mater. Sci. Technol.* 22 (2006) 641–644, <https://doi.org/10.1179/174328406X86128>.
- [128] P.J. Jacques, F. Delannay, J. Ladrière, On the influence of interactions between phases on the mechanical stability of retained austenite in transformation-induced plasticity multiphase steels, *Metall. Mater. Trans. A* 32 (2001) 2759–2768, <https://doi.org/10.1007/s11661-001-1027-4>.
- [129] Y. Liu, H. Yang, G. Tan, S. Miyazaki, B. Jiang, Y. Liu, Stress-induced FCC \leftrightarrow HCP martensite transformation in CoNi, *J. Alloys Compd.* 368 (2004) 157–163, <https://doi.org/10.1016/j.jallcom.2003.07.015>.
- [130] V.I. Levitas, M. Javanbakht, Thermodynamically consistent phase field approach to dislocation evolution at small and large strains, *J. Mech. Phys. Solids* 82 (2015) 345–366, <https://doi.org/10.1016/j.jmps.2015.05.009>.
- [131] S. Kuang, Y. Kang, H. Yu, R. Liu, Stress-strain partitioning analysis of constituent phases in dual phase steel based on the modified law of mixture, *Int. J. Miner. Metall. Mater.* 16 (2009) 393–398, [https://doi.org/10.1016/S1674-4799\(09\)60070-4](https://doi.org/10.1016/S1674-4799(09)60070-4).
- [132] L. Song, B. Wu, L. Zhang, X. Du, Y. Wang, C. Esling, J. Liu, C. Chen, Q. Feng, X. Fang, H. Wang, F. Liu, J. Lu, D. Raabe, Author's Accepted Manuscript, *Mater. Sci. Eng. A* (2017), <https://doi.org/10.1016/j.msea.2017.06.107>.
- [133] X. Wu, P. Jiang, L. Chen, F. Yuan, Y.T. Zhu, Extraordinary strain hardening by gradient structure, *Proc. Natl. Acad. Sci.* 111 (2014) 7197–7201, <https://doi.org/10.1073/pnas.1324069111>.
- [134] M. Naeem, H. He, F. Zhang, H. Huang, S. Harjo, T. Kawasaki, B. Wang, S. Lan, Z. Wu, F. Wang, Y. Wu, Z. Lu, Z. Zhang, C.T. Liu, X.L. Wang, Cooperative deformation in high-entropy alloys at ultralow temperatures, *Sci. Adv.* 6 (2020), <https://doi.org/10.1126/sciadv.aax4002>.
- [135] W. Woo, E.-W. Huang, J.-W. Yeh, H. Choo, C. Lee, S.-Y. Tu, In-situ neutron diffraction studies on high-temperature deformation behavior in a CoCrFeMnNi high entropy alloy, *Intermetallics* 62 (2015) 1–6, <https://doi.org/10.1016/j.intermet.2015.02.020>.
- [136] H. He, M. Naeem, F. Zhang, Y. Zhao, S. Harjo, T. Kawasaki, B. Wang, X. Wu, S. Lan, Z. Wu, F. Wang, Y. Wu, Z. Lu, Z. Zhang, C.T. Liu, X.-L. Wang, Stacking Fault Driven Phase Transformation in CrCoNi Medium Entropy Alloy, *Nano Lett.* 21 (2021) 1419–1426, <https://doi.org/10.1021/acs.nanolett.0c04244>.
- [137] B. Wang, H. He, M. Naeem, S. Lan, S. Harjo, T. Kawasaki, Y. Nie, H.W. Kui, T. Ungár, D. Ma, A.D. Stoica, Q. Li, Y. Ke, C.T. Liu, X.-L. Wang, Deformation of CoCrFeNi high entropy alloy at large strain, *Scr. Mater.* 155 (2018) 54–57, <https://doi.org/10.1016/j.scriptamat.2018.06.013>.
- [138] M. Frank, S.S. Nene, Y. Chen, B. Gwalani, E.J. Kautz, A. Devaraj, K. An, Correlating Work Hardening with Co - Activation of Stacking Fault Strengthening and Transformation in a High Entropy Alloy Using in - Situ Neutron Diffraction (2020) 1–11, <https://doi.org/10.1038/s41598-020-79492-8>.